ON NORTHERN HEMISPHERE CLIMATE CHANGE AND VARIABILITY DURING THE LAST HALF OF THE 20TH CENTURY

By

Jian Lu

SUBMITTED IN PARTIAL FULFILLMENT OF THE
REQUIREMENTS FOR THE DEGREE OF
DOCTOR OF PHILOSOPHY
AT
DALHOUSIE UNIVERSITY
HALIFAX, NOVA SCOTIA
DECEMBER 9, 2003

Your file Votre référence
ISBN: 0-612-89808-3
Our file Notre référence
ISBN: 0-612-89808-3

DALHOUSIE UNIVERSITY

DEPARTMENT OF OCEANOGRAPHY

The undersigned hereby certify that they have read and recommend to the Faculty of Graduate Studies for acceptance a thesis entitled "On Northern Hemispheric Climate Change and Variability During the Last Half of the 20th Century" by Jian Lu in partial fulfillment of the requirements for the degree of Doctor of Philosophy.

Dated: December 9, 2003

External Examiner: _____

Research Supervisor: _____

Examining Committee: _____

_____

_____

Departmental Representative: _____

DALHOUSIE UNIVERSITY

Date: **December 9, 2003**

Author: **Jian Lu**

Title: **On Northern Hemisphere Climate Change and Variability During the Last Half of the 20th Century**

Department: **Oceanography**

Degree: **Ph.D.** Convocation: **May** Year: **2004**

Contents

List of Tables

List of Figures

Abstract

The Northern Hemisphere climate underwent significant change during the last half of the 20th century. This thesis focuses on the changes over the Euro-North Atlantic sector characterized by an upward trend in the North Atlantic Oscillation(NAO) index and an eastward shift in the spatial pattern of interannual NAO variability.

Correlation analysis unravels a special relationship between the NAO and the first mode of North Atlantic storm activity and the emergence of a spatially coherent variability regime associated with the shifted NAO after the 1970's. Model experiments using a simplified AGCM (Hall model) driven by forcing diagnosed from NCAR/NCEP reanalysis data confirm the importance of the storm activity in the NAO shift and reveal the nonlinear dependence of the spatial pattern of the NAO on the NAO index, the pattern being shifted to the east (west) for high (low) NAO index, with confirmation being found in the observations. Therefore, it is suggested that the eastward shift of the NAO is a consequence of the relatively high NAO index during 1978-97 versus the relatively low index during 1958-77. The upward trend of the NAO is part of a hemispheric trend associated with a deepening of both the Icelandic and Aleutian lows. The trend is shown to strongly resemble the Cold Ocean Warm Land pattern and to be associated with a wave train emanating from the Indo-Pacific region of the tropical Pacific. The North Atlantic storm track is shown to feed back positively on the wave signal and give rise to a resonant NAO-like dipole. Non-stationary impacts of El Niño-Southern Oscillation on Euro-Atlantic interannual climate variablity are also investigated in the context of the 1970's climate regime change.

Acronyms

AGCM	Atmospheric General Circulation Model
AL-IL	Aleutian Low-Icelandic Low seesaw
AO	Arctic Oscillation
CGCM	Coupled General Circulation Model
COWL	Cold Ocean Warm Land
CPCA	Combined Principal Component Analysis
DJF	December, January, February
DJFM	December, January, February, March
ENSO	El Niño-Southern Oscillation
EOF	Empirical Orthogonal Function
EP	Eliassen-Palm Flux
GCM	General Circulation Model
GHG	Greenhouse Gas
IF	Ice Flux (through Fram Strait)
IPCC	The Intergovernmental Panel on Climate Change
ITCZ	Intertropical Convergence Zone
NAM	Northern Annular Mode
NAO	North Atlantic Oscillation
NAST	North Atlantic Storm Track
NCAR	National Center for Atmospheric Research
NCEP	National Center for Environmental Prediction
NH	Northern Hemisphere

NHST1	Leading Mode of Variability of the Northern Hemisphere Storm Track
PC	Principal Component
PDF	Probability Distribution Function
PDO	Pacific Decadal Oscillation
PNA	Pacific-North America
REOF	Rotated Empirical Orthogonal Function
RPCA	Rotated Principal Component Analysis
SCF	Squared Covariance Fraction
SH	Southern Hemisphere
SLP	Sea Level Pressure
SOI	Southern Oscillation Index
SST	Sea Surface Temperature
SVD	Singular Value Decomposition
SWT	Siberian Winter Temperature
UEA	University of East Anglia
Z500	500 hPa Geopotential Height

Acknowledgements

First, and foremost, I would like to thank my supervisor Dr. Richard Greatbatch. His insight, patience, generosity and kindness are deeply appreciated. I'm most grateful to him for guiding me into the realm of climate dynamics and I benefit most from his unique and insightful way of thinking and tackling the scientific questions.

Thanks to my committee members: Drs. Jinyu Sheng, Ulrike Lohmann and Harold Ritchie for their helpful comments.

Appreciation goes out to Dr. K. Andrew Peterson. Collabration with him has been very productive and his technical expertise expedited the completion of this thesis. I would also like to thank my colleagues and fellow students who helped along the way: Dr. Carsten Eden, Dr. Alex Medvedev, Mike Casey, Keath Borg, Doug Mercer, Chris Fogarty and Xiaoming Zhai.

I am indebted to Dr. Thomas Jung for helpful comments and discussion during the formulative stage of this thesis research, to Drs. Hai Lin, Jacques Derome and N. M. J. Hall for providing the model and model forcing, to Dr. Jeff Rogers for making his storm activity index available to me, to Dr. Viatcheslav Kharin for providing FORTRAN77 Rotated EOF subroutine. In particular, I'd like to thank Dr. Keith Thompson for teaching me the *Time Series* course. His lectures demonstrate the art of teaching. I am also grateful to him for helping with the statistical issues I encountered during my thesis study.

I thank Jackie Hurst for all kinds of help she has given me. She shows us life is also beautiful even without science.

Chapter 1

Introduction

1.1 Symptoms of Climate Regime Change

1.1.1 The global context

Amidst the often contentious debate on global warming, there is agreement that the Earth's surface temperature has increased by between 0.3 and $0.6°C$ over the last century (Houghton et al. [1995]). In addition, the heat content of the world oceans is thought to have increased by about 2×10^{23}J between the mid-1950s and mid-1990s, representing a volume mean warming of $0.06°C$ (Levitus et al. [2000]). Meanwhile, the increase in ocean heat content is at least an order of magnitude larger than the increase in heat content of any other component of the earth climate system. For example, the increase in atmospheric heat content during the same span of time is only about 6.6×10^{21}J (Levitus et al. [2001]). Recently, detection and attribution studies based on observations and models forced by observed and estimated anthropogenic greenhouse gases and aerosols can largely replicate the global warming signal (Levitus et al. [2001]; Reichert et al. [2002]; Barnett et al. [2001]; Stott et al. [2000]; Santer et al. [2000]; Gaffen et al. [2000]; Crowley [2000]; Tett et al. [1996]). This suggests that the observed climate changes are consistent with those expected from anthropogenic forcing, which broadens the basis for claims that an anthropogenic signal has been

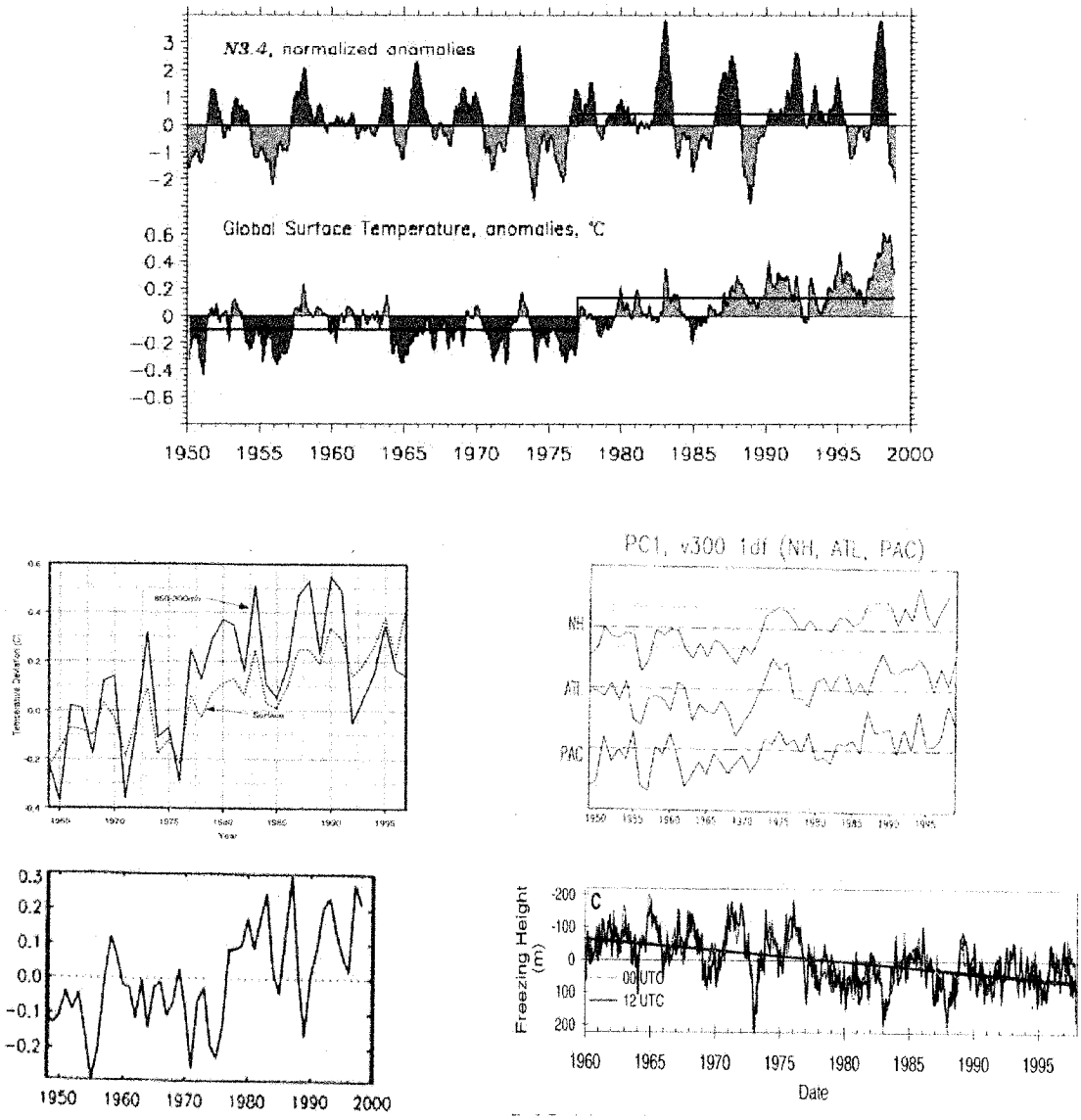

Figure 1.1: Top: Time series of Niño3.4 SST and the global annual mean surface temperature for 1950-1998 (from Trenberth et al. [2002]); Middle left: Time series for globally-averaged temperature for surface (dashed) and troposphere (solid) from radiosondes (from Lindzen and Giannitsis [2002]); Middle right: (top curve) PC time series of the leading winter (DJF) storm track EOF; (middle and bottom curves) same as above, but for leading PC for EOF analysis of the North Atlantic and North Pacific sector, respectively (from Chang and Fu [2002]); Bottom left: PC time series of the annual mean Pacific Ocean heat content integrated through 125 meters for the period 1948-1998 (from Stephens et al. [2001]); Bottom right: Tropical mean monthly anomalies of freezing-level height at 0000 and 1200 UTC, shown in red and blue, respectively. Note the vertical axis is inverted (from Gaffen et al. [2000]).

detected in the global climate system. Nevertheless, these models still have difficulties to replicate the regional structure of the observed climate change.

The temporal signal of the global warming has not been simply a linear increase. Rather there was an abrupt transition towards a warmer epoch around the late 1970's (Trenberth et al. [2002]). An abrupt increase occurred around that time in globally-averaged mid-tropospheric temperature (Lindzen and Giannitsis [2002]), North Pacific upper ocean heat content (Stephens et al. [2001]), northern hemisphere storm activity (Chang and Fu [2002]) and tropical mean freezing-level height (correlated well with mid-tropospheric temperature) (Gaffen et al. [2000]). Figure 1.1 summarizes all these symptoms of sudden transition. In the context of the climate transition, the low frequency modes of climate variability, with time scales from interannual to interdecadal, have also experienced some substantial changes, as discussed further in this thesis.

1.1.2 Pacific sector

Apart from the trend towards higher freezing-level height, the tropical Pacific atmosphere has shown greater warming at the surface than aloft since the late 1970's, resulting in a trend towards increased tropical lapse rate and decreased static stability (Gaffen et al. [2000]). These scenarios have been suggested to be driven by an enhanced hydrological cycle and increasing tropical sea surface temperature (SST) (Diaz and Graham [1996]). These tropical changes are also consistent with the fact that El Niño events have become more frequent and persistent in recent years (Wang [1995]; Trenberth and Hoar [1996]).

Coincident with these tropical changes, a so-called "regime shift" occurred during 1976-77 over the North Pacific and the surrounding land masses (Trenberth et al. [1998]; Trenberth and Hurrell [1994]). Since the "regime shift", the central North Pacific has been cooler than normal, due to stronger westerlies along $40°N$, which favor enhanced air-sea heat loss and lower SST[1]. Consistent with the wind changes, winter

[1]In contrast to the tropical dynamically coupled system, in mid-latitudes, only the atmospheric

season sea level pressure (SLP) and 500 hPa heights over the extratropical North Pacific have been lower, and the positive polarity of the Pacific-North America (PNA, Wallace and Gutzler [1981]) pattern has been prevalent. Accordingly, the North Pacific storm track shifted southward with enhanced storm activity across the North Pacific south of 40°N and downstream over the southern United States, and reduced activity farther north (Trenberth and Hurrell [1994]). Some researchers suggest that the upward trend in the PNA index, which is accompanied by a downward trend in SST over the central North Pacific, can be interpreted as an extratropical response to the rather abrupt rise in eastern equatorial Pacific SST that took place around 1976-1977 (e.g., Graham [1994]; Nitta and Yamada [1989]; Trenberth and Hurrell [1994]). Others argue that a positive feedback between the subtropical gyre and the overlying atmospheric circulation may also contribute to the decadal and interdecadal variability in the North Pacific (Latif and Barnett [1994]; Latif and Barnett [1996]).

Additional evidence has been put forward that decadal-centennial climate variability in the North Pacific has a tropical root in light of interhemispheric symmetries in paleoclimate change (Evans et al. [2001]). For instance, several of the largest decadal SST changes observed in the last 100 years are in phase in the North and South Pacific gyres (Linsley et al. [2000]). Zhang et al. [1997] documented the spatial signature of the interdecadal climate variability in the Pacific and compared it with the patterns associated with the El Niño-Southern Oscillation (ENSO) cycle. They found that interannual and interdecadal variability exhibit roughly similar spatial structure in each of the SST, SLP and wind stress fields, suggesting an ENSO-like forcing mechanism for the decadal change in the North Pacific. However, extending the analysis to the Southern Hemisphere and some other variables (e.g., wind divergence and specific humidity), Garreaud and Battisti [1999] unraveled different spatial patterns of atmospheric circulation anomalies for the ENSO-band and decadal ENSO-like variability, suggesting that different tropical forcing mechanisms are involved on

influence on the ocean has been relatively well understood and established, while the oceans' "back interaction" on the atmosphere is much less robust and has been a topic of heated debate (Kushnir et al. [2002]).

these two time scales. Gu and Philander [1997] proposed a tropical-extratropical interaction mechanism to explain the prolonged persistence of warm conditions over the tropical Pacific. The link between the extratropical and tropical ocean is the relatively shallow, wind-driven meridional circulation that involves the subduction of water parcels in the eastern regions of the subtropical oceans. The water then flows southwestward, essentially adiabatically along surfaces of constant potential density, to the equatorial thermocline. Here, upwelling transfers the parcels to the surface, thereafter the tropical easterly winds carry them poleward via Ekman drift. This meridional pathway allows a mechanism whereby the extratropical atmospheric teleconnection response can feed back to the tropics. For example, the response of the atmosphere to the warming in the tropical SST involves an intensification of the extratropical westerlies, leading to colder surface waters (mostly because of evaporation) in the extratropical regions that happen to be windows to the equatorial thermocline. The cold water pumped downward in those regions follows the mean flow to the tropics. Once the anomalously cool subducted water reaches the tropical strip many years later, it upwells to the surface, halts the initial warming, and initiates the cold conditions in the tropics. This argument implies a continual, interdecadal climate fluctuation with a period that depends on the time it takes for water parcels to travel from the extratropics to the equator. Most recently, from the observations over the past 50 years, McPhaden and Zhang [2002] showed that the tropical overturning circulation driven by equatorial easterly winds has been slowing down since the 1970's, causing a decrease in upwelling of about 25% in an equatorial strip between 9°N and 9°S. The resultant reduction in equatorial upwelling of relatively cool water is associated with the rise in equatorial SST of about 0.8°C. Warmer surface temperature in turn alters the patterns of deep convection in the atmosphere so as to favour weaker trade winds. Thus, the oceanic and atmospheric processes in the tropics work together to reinforce each other, similar to the positive feedbacks that occur during ENSO events. While, if the system is to oscillate on multidecadal timescales, then delayed negative feedback mechanisms, one candidate for which is the Gu and

Philander [1997] mechanism, must also be important.

1.1.3 Euro-Atlantic sector

Wintertime climate over the Euro-Atlantic region also underwent a change during the 1970's. The North Atlantic Oscillation (NAO), the primary mode of variability in the northern hemisphere winter atmospheric circulation, shows a trend toward the positive phase in its index during the last few decades (Hurrell [1995b]; Hurrell [1996]; Hurrell et al. [2003], see the upper and middle panels in Figure 1.2). A similar trend is found in the EOF manifestation of this primary mode, i.e. the Arctic Oscillation (AO) or Northern Annular Mode (NAM), as discussed by Thompson and Wallace [2000a] and Thompson et al. [2000b] (see the lower panel in Figure 1.2). There is a subtle difference between the NAO and the AO because they are defined differently. The NAO index is usually defined based on the SLP difference between stations over the Iceland and the Azores or Spain, while the AO/NAM index is based on empirical orthogonal function (EOF) analysis of the northern hemisphere SLP variability. There has been a heated debate as to which one is more dynamically fundamental (Hurrell et al. [2003]; Cash et al. [2002]; Ambaum et al. [2001]). Given the fact that the AO and NAO are very similar to each other on both spatial and temporal aspects, these two modes will be treated as one phenomenon in most of this thesis.

The NAO corresponds to a meridional displacement in atmospheric mass with centers of action near the Icelandic low and the Azores high. The NAO index measures the strength of mid-latitude westerly winds blowing across the North Atlantic. For the high (low) phase of the NAO, the westerly winds are strengthened (weakened). Dynamically, the NAO/AO is an internal mode of variability of the atmosphere and is substantially driven by the interaction between baroclinic transients and the low-frequency flow (e.g., Limpasuvan and Hartmann [2000]; Thompson et al. [2003]). Thus the existence of the NAO does not depend on the variability of the underlying SST or air-sea interaction (Barnett [1985]). Nevertheless, much effort has been made

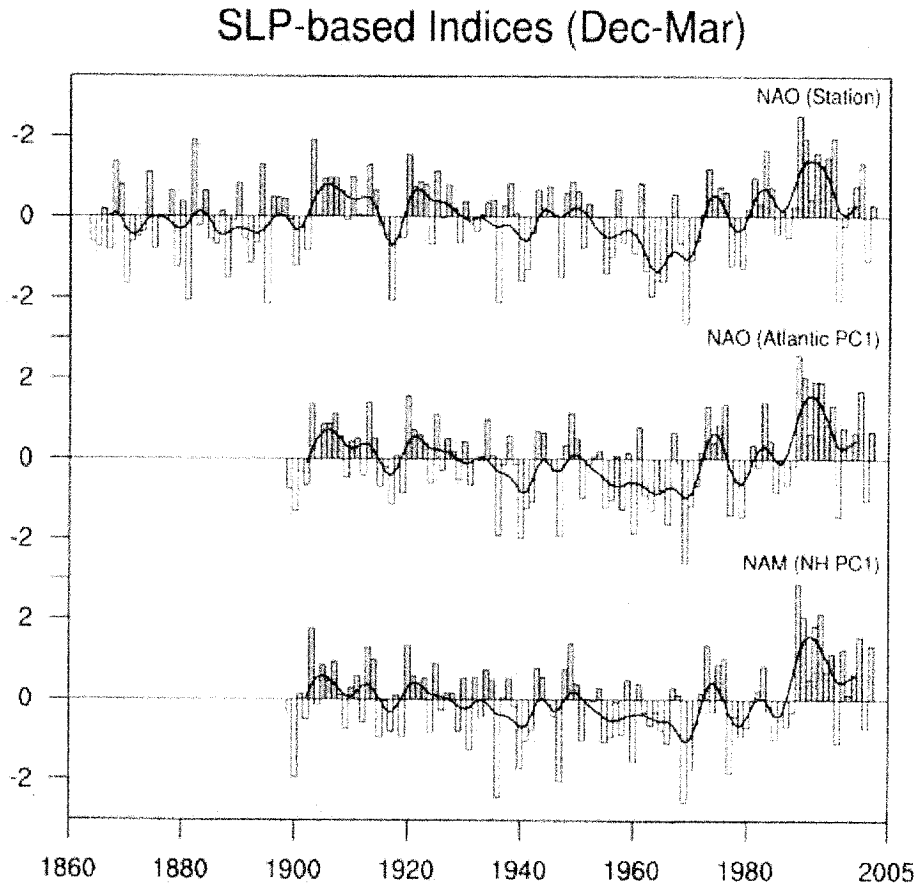

Figure 1.2: Normalized indices of the winter mean (DJFM) NAO/AO constructed from SLP data. In the top panel, the NAO index is defined as the difference in normalized SLP anomalies, Lisbon, Portugal minus Stykkisholmur/Reykjavik, Iceland, from 1864 through 2002. The average winter SLP anomaly at each station is normalized by the long-time mean (1864-1983) standard deviation at that station. In the middle panel, the NAO index is the principal component time series of the leading EOF of Atlantic-sector winter mean SLP. The station based index is correlated with the PC based index at 0.92 during the overlap period. In the lower panel, the index is the principal component time series of the leading EOF of northern hemisphere (north of $20°N$) winter mean SLP, i.e., the AO or Northern Annular Mode (NAM) index. In each case, the heavy solid lines represent the indices smoothed to remove fluctuations with periods less than 4 years. The indicated year corresponds to the January of the winter season. See http://www.cgd.ucar.edu/~jhurrell/nao.html for updated time series. (from Hurrell et al. [2003])

to hindcast the NAO using atmospheric circulation models (AGCM's) driven by historical SST and sea ice anomalies for the global ocean. For instance, using different AGCMs, Rodwell et al. [1999], Mehta et al. [2000] and Latif et al. [2000] were able to reproduce the low frequency (time scales of 6 years and longer) variability of the NAO in the ensemble mean of an ensemble of experiments driven by the observed time series of SST and sea-ice distribution. However, as argued by Bretherton and Battisti [2000], the reproduction of atmospheric variability in a hindcast ensemble experiment does not imply predictability if the variability in the coupled system, including the SST and sea-ice, is ultimately driven by unpredictable atmospheric noise. Moreover, the mechanisms by which the SST and sea-ice can influence the NAO variability are still not understood (See Czaja et al. [2003], for a summary of this problem)

Concerning the recent upward trend of the winter mean NAO or AO, Thompson et al. [2000b], using a Student's t test, showed that the linear component of the trend in the AO index is statistically significant above the 5% confidence level during the Northern Hemisphere winter. By synthesizing a time series with the same intraseasonal stochastic properties as the AO, Feldstein [2002] claimed that both the trend and the variance increase of the AO during the last 30 years of the 20th century are in excess of that to be expected if all the interannual variability was due to atmospheric intraseasonal stochastic processes. By corollary, coupling with the hydrosphere and/or cryosphere or forcing external to the climate system may contribute to the observed trend in the AO. Meanwhile, some climate models that include greenhouse gas and/or aerosol forcing have also shown a noticeable trend in the AO/NAO index (e.g., Gillett et al. [2000]; Shindell et al. [1999]; Fyfe et al. [1999]). However, caution should be used before jumping to the conclusion that the AO/NAO trend is driven by external or anthropogenic forcing. For example, Wunsch [1999] synthesized a stationary time series with the same spectral structure as the winter mean NAO index and showed that stationary time series can exhibit similar behavior to the observed NAO index, with extended decadal excursions from the mean and local

apparent trends, but without any special physical causality. Given the limited instrumental record of the NAO index, one should be very careful about rejecting the null hypothesis of stationarity of the NAO index, and claiming that one has entered a new climate state with so short a time series. In spite of the debate on the origin of the trend, progress has been made in understanding the direct forcing mechanisms for the North Atlantic climate change. Most notably, the trend of the tropospheric circulation during the second half of the 20th century (including the trend of the NAO) is successfully captured by Hoerling et al. [2001a]'s ensembles of experiments driven by the observed time series of SST specified only over the tropical ocean, suggesting a possible tropical source for recent North Atlantic climate change. These authors also conjectured that the warming over the tropical oceans might be attributable to the influence of increased greenhouse gases. Nevertheless, the question of how the tropical SST drives the North Atlantic climate change is not yet answered and is a topic that is explored further in this thesis.

In addition to the upward trend in the winter NAO index, the spatial pattern of the NAO has shifted eastward since the late 1970s, resulting in a link between the NAO and ice export through Fram Strait that did not exist previously. In particular, since the shift, northerly(southerly) wind anomalies over Fram Strait drive more (less) sea ice out of the Arctic through the Strait when the NAO index is positive(negative). The eastward shift of the NAO was first pointed out by Hilmer and Jung [2000] from the changing relationship between the NAO index and the hindcasted ice flux through Fram Strait. As will be shown in this thesis, use of the pressure difference across Fram Strait as a proxy for the ice flux through the Strait further confirms that a secular change in the relationship between the NAO and the ice flux did happen (Lu and Greatbatch [2002]). A natural question arises as to whether the NAO pattern shift is an expected behavior of the NAO internal to the atmosphere, or driven by some unusual external forcings, e.g. anthropogenic climate change? Attempting to answer this question, Jung and Hilmer [2001] analyzed the historical SLP data from 1908 to 1997 by dividing the record into eight overlapped 20-year periods. Only in the last

twenty years, i.e., 1978-97, was a pronounced longitudinal shift found in the northern center of action of the NAO. Jung and Hilmer also analyzed a coupled atmosphere-ocean-sea ice model ECHAM4/OPYC3 under present-day climate conditions (i.e., concentrations of greenhouse gases were fixed to the observed 1990 values), and could not find any link between the NAO and sea ice export through Fram Strait that would indicate an eastward shift in the spatial pattern of the NAO in different 19-year periods. Further, a Monte Carlo test was performed under the null hypothesis that the NAO index and the ice export through Fram Strait simulated by the coupled GCM are realizations of independent first-order auto-regressive (AR(1)) processes. In the 10,000 realizations simulated by the AR(1) processes, the 2.5th and 97.5th percentiles of the estimated cross-correlation coefficients (using a time window of 19 years) reach only -0.45 and 0.47, respectively, far below the 0.7 correlation that was found during 1978-97 by Hilmer and Jung [2000]. Hilmer and Jung therefore argued that the NAO shift is not a characteristic long-term property of the climate system and it is "unusual" in the context of natural climate variability. Using the same ECHAM4/OPYC3 coupled model, Ulbrich and Christoph [1999] found a systematic northeastward shift of the NAO's northern center in their scenario run driven by the IPCC IS92a GHG radiative forcing, while in the control run, using present day radiative forcing, the northern center of the NAO is quite fixed. These authors speculated on the causes for the eastward shift of the NAO and argued that the changing baroclinicity of the upper troposphere and the Atlantic storm track activity (as a stable feature of the scenario run) might be related. Thus, it is possible that the NAO shift may be related to an anthropogenic signal that has just begun to emerge during the last few decades. Further evidence for the shift and factors contributing to its cause are issues explored in this thesis.

1.2 Questions to be addressed

Among the variety of aspects of climate change evident during the last half of the 20th century, the change in the northern hemisphere tropospheric circulation and its consequences are the main subject of this study. Only the winter season (DJF) is considered in this thesis. In particular, the following questions are addressed. (i) What are the possible physical reasons for the recent NAO changes including the upward trend in the NAO index and the eastward shift of the NAO spatial pattern? (ii) Which climate variability mode is most representative for the multidecadal trend observed in the tropospheric circulation? What is the forcing mechanism for the trend? (iii) does ENSO impact on Euro-North Atlantic climate? If it does, how? Has the impact of ENSO on Euro-North Atlantic climate changed as the background climate has changed?

1.2.1 Possible causes for the NAO shift

The NAO is a large-scale atmospheric flow pattern with centers of action concentrated in the North Atlantic sector with a low pressure anomaly over Iceland and a high pressure anomaly over the Azores for the positive polarity of the NAO. This dipole pattern can be identified by teleconnection analysis (e.g., Wallace and Gutzler [1981]), while the dynamics that determine the loci of the centers of action of the NAO is an issue that is traceable to the existence of the storm track. In a map of the standard deviation of high-pass filtered 500 hPa height, which measures the storminess of the mid-latitude troposphere, two storm tracks stand out prominently in the northern hemisphere, one over the North Pacific and the other over the North Atlantic (Figure 1.3). The baroclinicity (which is measured by the maximum Eady growth rate σ_{BI} [2] and dominated by the vertical wind shear) upstream of the storm track provides the necessary conditions for the growth of transient eddies and hence determines the geographical distribution of the storm track. As argued by Hoskins and Valdes [1990],

[2] $\sigma_{BI} = 0.31 \cdot f \cdot |\frac{\partial \mathbf{v}}{\partial z}| N^{-1}$, where f is the Coriolis parameter, $\mathbf{v}$ is the horizontal wind, and $N = [(g/\theta)(\frac{\partial \theta}{\partial z})]^{1/2}$ is the Brunt-Väisällä frequency with the potential temperature θ.

in the framework of the atmospheric-only system, the direct thermal effect of the eddies ($\overline{v'T'}$) acts against the conditions that the storm track depends on, although the eddy vorticity flux tends to reduce this effect. It is the mean diabatic heating due to the sensible and latent heat release in the storm track region that maintains the necessary condition for the storm track, i.e., the mean maximum baroclinicity in the region. Thus, in this sense, the North Atlantic and Pacific storm tracks are self-maintaining. Originally, the diabatic heating for the atmosphere comes from the underlying ocean, which provides a source of moisture and heat. It can therefore be argued that it is the land-sea distribution and warm oceanic boundary conditions that settle the location for the storm tracks.

Near the axis of the storm track, the transient eddies associated with the storm track play a key part in driving the mid-latitude westerly jets. The wobbling and pulsing in the eddy-driven jet stream over the North Atlantic are the typical behaviors associated with the NAO. As mentioned above, the NAO is an internal variability mode in the atmosphere. Observational and model evidence unambiguously directs to the conclusion that a substantial amount of the NAO variability is sustained by the eddy vorticity/momentum flux in the middle-high latitudes associated with the North Atlantic storm track (Lau [1988]; James and James [1989]; Lau and Nath [1991]; Ting and Lau [1993]; Hurrell [1995a]; Thompson et al. [2003]). For example, Lau and Holopainen [1984] and Lau and Nath [1991] showed that lower tropospheric eddy heat and vorticity fluxes reinforce one another and force cyclonic circulation tendencies poleward of the storm track axes and anticyclonic tendencies equatorward. In the upper troposphere, the polarity of the circulation tendencies associated with eddy heat fluxes is reversed and values are considerably smaller than tendencies associated with eddy vorticity fluxes. The overall effect of the eddy forcing is to maintain a NAO-like barotropic circulation pattern. The importance of the transient vorticity flux in directly maintaining the extremes of the NAO, especially the importance of the flux by the transient rotational flow was examined by Hurrell [1995a].

In terms of the AO or NAM paradigm, a positive feedback mechanism for the

NAO/AO/NAM between the eddy momentum flux and the mean wind structure was further demonstrated by Limpasuvan and Hartmann [2000] and Hartmann et al. [2000]. As shown in Figure 1.4, when the AO/NAO is in its high phase, the zonal flow of the annular mode exhibits considerably stronger westerly winds and westerly vertical wind shear between $60° - 80°N$ than the low phase. The stronger westerly winds in the upper troposphere cause planetary waves to be less strongly refracted toward the pole, resulting in anomalous equatorward wave propagation and poleward momentum flux. The poleward momentum flux anomalies in turn support the high latitude westerlies and strengthen the polar vortex, thereby a positive feedback loop is completed. Analogous arguments may be invoked to infer the feedback that maintains the negative NAO/AO/NAM index phase. In the sense of this maintaining mechanism, the centers of action of the NAO are substantially regulated by the intensification and displacement of the storm track in the North Atlantic basin. This leads to the first candidate that could be potentially related to the NAO shift: the North Atlantic Storm Track (NAST). The first goal of this thesis study is to understand the relationship between the NAO and the NAST and the importance of eddy activity in driving the eastward shift of the NAO.

The NAO shift could also be related to the changing mean state in different decades, i.e., the low NAO index period of 1958-77 (hereafter, P1) and the high NAO index period of 1978-97 (hereafter, P2). It has been reported by Kwok [2000] that during the prolonged period of positive phase of the NAO, the ice flux and the NAO index are significantly correlated, but the correlation is reduced during the negative NAO years. Seeing this, one may conjecture that the eastward shifted NAO pattern of interannual variability during P2 might arise from the changed mean state during P2 when the average DJF NAO index is 0.48 compared to the negative average index of -0.74 during P1. Model studies have suggested that the climate variability mode or climate regime can be strongly dependent on the background state. For instance, by introducing a concept of "neutral vector", Marshall and Molteni [1993] interpret the flow regimes as quasi-stationary vectors with slowest growth rate as defined by the

Figure 1.3: Northern Hemisphere winter (DJF) storm track in terms of the root-mean-square of high-pass filtered 500 hPa height. A binomial filter with a maximum response in the 2-8-day period range is used. See Figure 3.2 for detailed description of the filter.

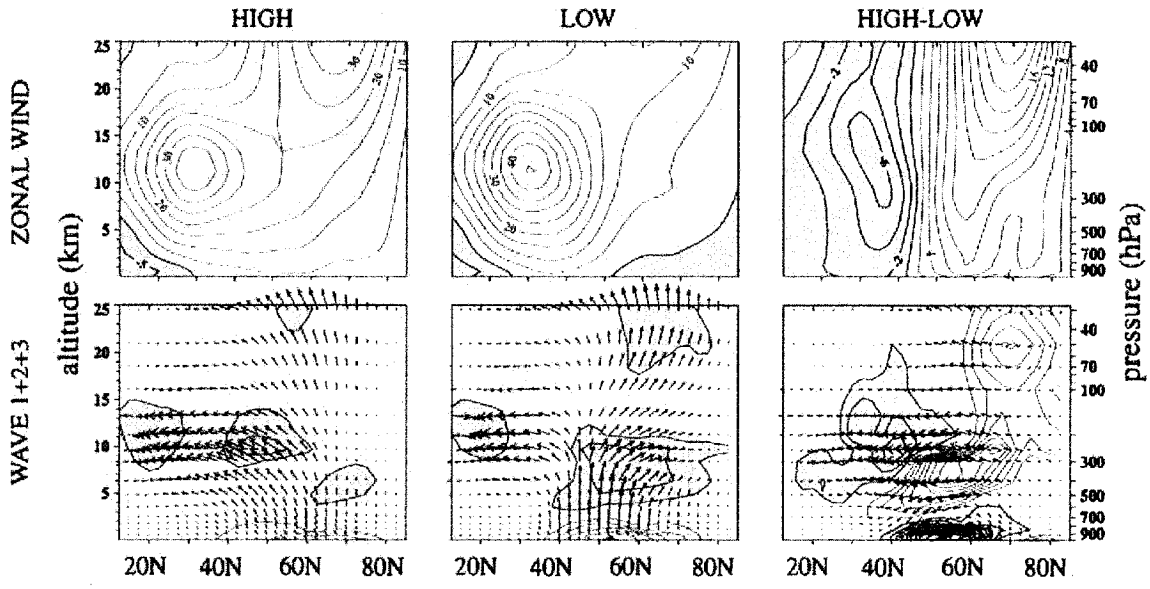

Figure 1.4: Composites for periods of high and low AO/NAM index and their difference (Left, Center and Right) during the December-March period. The zonal wind composites are on the top (units are m/s). The Eliassen-Palm (EP) flux cross sections for the sum of zonal wavenumbers 1 to 3 are on the bottom. Positive contours are red. (from Hartmann et al. [2000])

smallest eigenvalues of a self-adjoint operator derived from a model linearized about a basic state. The leading neutral vector computed using the wintertime climatology as a basic state exhibits a dipole pattern reminiscent of the NAO over the North Atlantic sector. Their sensitivity experiments with alternate basic states showed that the spatial patterns of the leading neutral vectors are strongly controlled by the form of the basic state. Strong dependence on the basic states has been also reported by Ting and Lau [1993]. Thus, the effect of changing mean states between P2 and P1 on the spatial pattern of the NAO will be investigated using a linearized AGCM in this thesis study.

1.2.2 Understanding the trend

During the last 50 years or so, the wintertime NH climate has undergone some significant changes (see Figure 1.1). To understand these changes, we ask and tackle the following two questions: first, how does the atmospheric circulation trend project onto the climate variability modes such as the AO/NAO, PNA, ... etc.? Can we identify a climate regime pattern for the pattern of the observed circulation trend? Second, how are the changes in the multidecadal trend driven? Understanding the forcing mechanism should lead to some insight into the atmospheric circulation change. The Arctic Oscillation (AO), because it accounts for a large part of the warming over the NH in recent decades (Thompson et al. [2000b]), has attracted considerable attention. However, some other circulation patterns of low-frequency variability also contribute to the northern hemisphere climate trend. Among these are, for example, the Cold Ocean Warm Land pattern (COWL, Wallace et al. [1996]), the seesaw pattern (Honda et al. [2001a]; Honda and Nakamura [2001b]), and the circulation pattern associated with the first mode of the Northern Hemisphere storm track activity (Chang and Fu [2002]). But much less attention has been paid to them.

Let us look at the COWL index and the COWL pattern first. The COWL index is defined in terms of the areally weighted average of the lower tropospheric temperature (500-1000 hPa thickness) poleward of 40°N. The weight function is positive (negative)

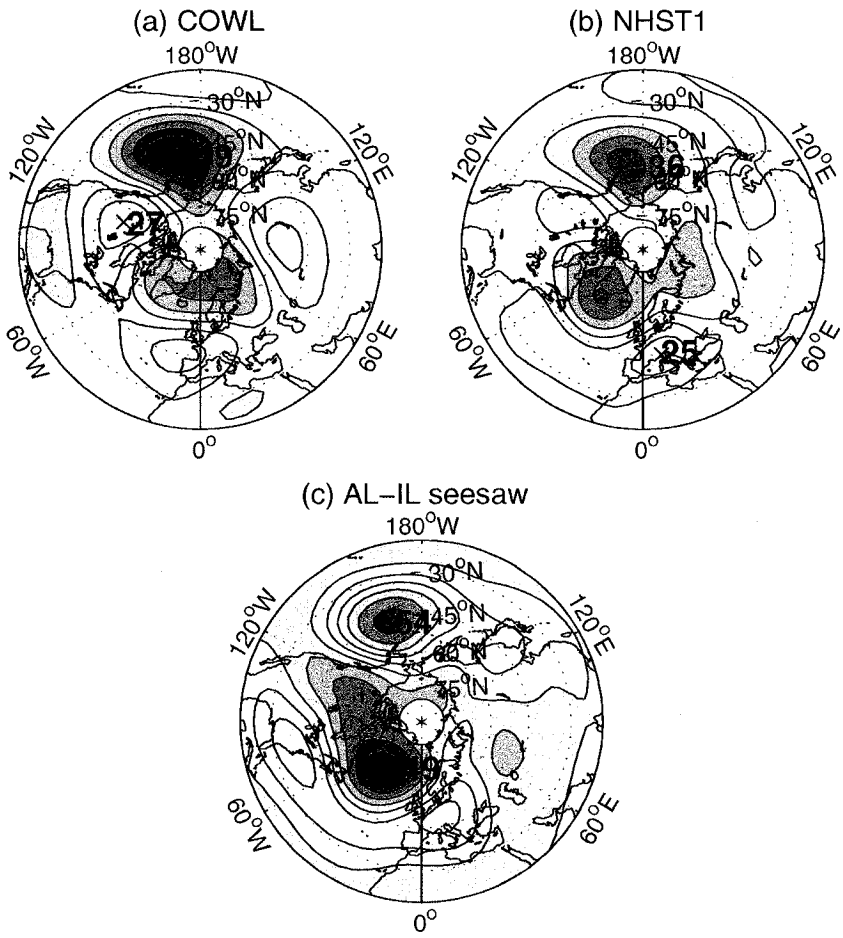

Figure 1.5: Regression patterns of winter(DJF) mean 500 hPa height against (a) the COWL index; (b) NHST1 index and (c) AL-IL seasaw index. All the plots contour at 10m/std of index.

and constant over the land (ocean) and the constants are determined so as to make the average of the weight function over all grid points poleward of 40°N identically equal to zero. Thus the COWL index picks out a temperature pattern contrasting the opposite thermal tendency between the land and the ocean. The 500 hPa height regression pattern associated with the COWL is characterized by positive height anomalies over western North America and Russia and negative height anomalies over the North Pacific and Barents Sea, indicative of a northward displacement of the jet stream over the high-latitude Eurasian continent and a strengthened westerly wind over the latitude belt of the subtropical jet in the North Pacific and the eddy driven jet in the North Atlantic sector (see Figure 1.5a). The COWL regime can also be derived directly from nonlinear regime extraction statistics, like cluster analysis (Palmer [1999]; Corti et al. [1999], see their cluster A in Fig. 3a) or nonlinear principle component analysis (Monahan et al. [2001], see their Fig. 3b), suggesting that the positive phase of the COWL pattern is a preferred mode of circulation in the northern hemisphere. Though COWL is a natural climate mode and its existence does not depend on dynamical air-sea interaction or external radiative forcing (Broccoli et al. [1998]), from the nonlinear dynamical perspective, such as proposed by Palmer [1993] and Palmer [1999], an external forcing may change the frequency of occurrence of a preferred flow regime like COWL.

Chang and Fu [2002] have examined the principal modes of variability of the northern hemisphere circulation from the perspective of the storm tracks, using the variance of the high pass filtered 300 hPa meridional wind component as a measure of the amplitude of baroclinic wave activity. In their leading EOF, the amplitude of the Pacific and Atlantic storm track varies in unison. The corresponding time series of the principal component (PC) shows a pronounced upward transition during the mid 1970's (see Figure 1.1). This mode will hereafter be referred to as NHST1 mode. The associated pattern in the 500 hPa height field, as inferred from linear regression onto the PC of the NHST1 mode, is characterized by simultaneous fluctuations in the depth of the Aleutian and Icelandic lows (Figure 1.5b). The same circulation

pattern associated with this storm track mode is found all the way up to the upper troposphere. Since Chang and Fu's streamwise zonally-symmetric circulation pattern is dominated by an interdecadal trend, it cannot be identified from teleconnection or EOF analysis, which tends to pick out coherent patterns at interannual time scales. In fact, in the observed statistics, pressure (or geopotential height) fluctuations in the vicinity of the Icelandic and Aleutian lows tend to be negatively, rather than positively correlated at interannual and short time scales. The so-called Icelandic and Aleutian lows seasaw (AL-IL seesaw, hereafter) was first pointed out by Honda and Nakamura [2001b] who noted that the anti-correlation between the two lows starts to emerge from January and becomes significant from February to March. Here the AL-IL seasaw index (AII) is simply defined as the difference in the normalized, areally averaged 500 hPa geopotential height between the Aleutian ($30° - 65°$N, $160°E - 140°W$) and Icelandic ($55° - 75°$N, $60°W - 0°E$) lows. The corresponding AL-IL seasaw spatial pattern on 500 hPa height can then be obtained by regressing the AII onto the 500 hPa height fields (shown in Figure 1.5c). For the climate variability modes we have introduced so far, including the NAO/AO, COWL, NHST1 and AL-IL seesaw, each illustrates different facets of the structure of circulation variability, and each has exhibited some long-term change in its indices. So one may ask which mode has the most merit in representing the multidecadal circulation trend observed over the past 50 years? If we can identify a mode for this trend, what physical insight might it lead to? So, at first, we treat each of these perspectives equally and compare them with the Northern Hemisphere circulation trend to see which is most representative for the trend. After the identification, intensive model experimentation will be carried out focusing on this mode as well as the AO/NAO. Hopefully, the model examination on this mode will shed some light on the mechanism driving the circulation trend.

As aforementioned, Hoerling et al. [2001a] succeeded in capturing the circulation pattern of the trend since 1950 by specifying the time evolving SST over the tropical oceans and thus related the trend to the tropical ocean warming during the past half-century. Recent measurements show that the energy budget of the tropics has

varied substantially in the past two decades. Wielicki et al. [2002] found that during the 1990s, the long wave energy emitted from the tropics increased and the reflected solar radiation decreased by a smaller amount, resulting in a net loss of energy [3] from the tropics (between 30°S and 30°N) relative to earlier years in the record. Chen et al. [2002] showed that the change in the tropical energy budget was associated with a shift in position and intensity of convection, clouds, and large-scale tropical circulation. Convection, cloudiness, and upward motion decreased in the vicinity of Indonesia. At other longitudes, convection increased along the Intertropical Convergence Zone (ITCZ). This reorganization of convection ends up with stronger upward motion of air masses near the equator and stronger sinking motion in the subtropics, a decadal-time-scale strengthened tropical Hadley circulation. So an important question arises as to the tropical root for the low-frequency Northern Hemisphere circulation change, in particular, the importance of tropical diabatic processes in driving the extra-tropical circulation. As pointed out by Trenberth et al. [1998], there are two on-going challenges pending further scientific exploration: (a) improved knowledge of the tropical forcing; and (b) determining reliably the atmospheric response patterns to those forcings. Contribution will be made to these two challenges during the course of tackling the forcing mechanisms of the tropospheric circulation trend in this thesis.

1.2.3 ENSO impact on the Euro-North Atlantic Sector

The ENSO phenomenon, as the most prominent climate variability mode in the earth climate, has been extensively studied. The association between ENSO and climate anomalies over the Pacific basin and North America has been well documented (see Trenberth et al. [1998] for a review). Relatively less so is the ENSO impact on the climate of the North Atlantic region. However, the ENSO-Europe connection has been detected during the extreme events of ENSO. In what we call the "canonical" Euro-Atlantic impact of ENSO, composites of the difference in winter mean SLP over

[3] Net flux is defined as solar insolation minus short wave reflected flux minus long wave emitted flux.

the Euro-Atlantic sector for warm minus cold events indicate a statistically significant signal with a positive anomaly over northern and northeastern Europe and a negative anomaly in a zonal belt stretching from the east coast of the United States to the Black Sea, reminiscent of the negative NAO (Fraedrich and Müller [1992]; Fraedrich [1994]; Merkel and Latif [2002]). These composite pressure anomalies are qualitatively consistent with the European Grosswetter response showing enhanced cyclonic (anticyclonic) activity over central Europe during warm (cold) ENSO events (Fraedrich [1990]). The sensitive tail end of the North Atlantic storm track, in association with different phases of ENSO, shifts in such a way as to result in higher temperature and precipitation over northern (and the reverse over central and southern) Europe in the cold event composite. It has also been noted that the warm extremes are associated with highly variable winters; cold extremes tend to produce more persistent response with less variation between individual events, thus resulting in an impression that the European climate is influenced more strongly by La Niña than by El Niño events (Pozo-Vázquez et al. [2001]).

Nevertheless, the impact of ENSO on the Euro-Atlantic sector is not robust on interdecadal time scales. For example, Rogers [1984] found the canonical response in SLP data from 1940-1979, but found a somewhat different signal during the period 1900-39. van Loon and Madden [1981] have also found non-stationary teleconnections associated with ENSO by correlating the winter SLP from Darwin with SLP from several European stations. Only patterns from the second half of the record (1940's to 80's) clearly show the structure of correlation as expected from Fraedrich [1994]'s composites. Recently, Rimbu et al. [2003] detected a shift in the late 1970's in the correlation between the Nino3 index and the Red Sea coral record and attributed the shift to non-stationarity in the ENSO teleconnection pattern. A related non-stationarity between ENSO and rainfall over Israel has been reported by Price et al. [1998]. Mariotti et al. [2002] and Rodo et al. [1997] report further evidence of non-stationarity between ENSO and rainfall over Europe.

Since the late 1970's, the tropical circulation and its relationship to global climate changed, with El Niño events becoming more frequent and persistent in recent years (Wang [1995]; Trenberth and Hoar [1996]). During this time, the amplitude of El Niño also increased (An and Wang [2000]; Xue [2003]). These changes were accompanied by a notable modification in the evolution pattern of the coupled ENSO system (Trenberth et al. [2002]): during the 1960's and 70's the warm SST anomalies expanded westward from the South American coast into the central equatorial Pacific (Rasmusson and Carpenter [1982]); after 1980, the warm SST anomalies propagated eastward across the basin from the central Pacific or developed concurrently in the central and eastern Pacific (Wallace et al. [1998]). Seeing this and that the "regime shift" in the Pacific and the spatial pattern shift in the interannual variability of the NAO both occurred at the late 1970's, it is compelling to ask if the extratropical tele-connection associated with ENSO also experienced some changes at that time. The elaboration on it will be laid out in Chapter 5 focusing on the ENSO's impact on the Euro-North Atlantic region.

1.3 Thesis Outline

The materials of this thesis will be laid out as follows:

Besides statistical methods, numerical modelling is the key methodology in this study. So, before looking into any scientific issue, the configuration of a simplified atmospheric GCM as well as the way the model is forced will be first presented in Chapter 2. Effort will be made to understand the NAO shift in Chapter 3, starting with a correlation analysis applied to the NAO index, Rogers' storm track index (Rogers [1997]), a proxy index for ice flux through Fram Strait, and Siberian winter temperature. The correlation analysis is followed by ensembles of AGCM experiments applying a NAO-related forcing, which is inferred by regressing the model forcing computed for each winter against the observed NAO index. A linearized model will also be applied to investigate the effects of eddy forcing, diabatic forcing and the

changed background state on the NAO and its eastward shift.

Chapter 4 focuses on interpreting the climate change since the 1950's in terms of climate variability modes and understanding its driving mechanism. Not only in the circulation pattern, but in its relationship to the Northern Hemisphere storm track and tropical diabatic forcing, a "COWL-like" mode stands out among others as the dominant pattern representing the climate change. The forcing mechanism for this mode is then further examined using the AGCM and compared with the forcing mechanism for the AO. For this purpose, model experiments using both a full nonlinear and a linearized model are implemented in this chapter.

The issue of how the NH extratropical teleconnection associated with ENSO changed between the pre- and post-1970's is addressed in Chapter 5. In this thesis, a concluding remark is presented at the end of each chapter except Chapter 6. Therein, an overall summary will be given for the whole thesis.

Chapter 2

Model Configuration

2.1 The Hall atmospheric model

The model used here is a dry atmospheric primitive equation model (Hall [2000], Hall model hereafter), which describes the motion of an inviscid, adiabatic, hydrostatic, perfect gas surrounding a rotating, spherical planet, driven by a time-independent forcing. Model equations are written in terms of vorticity, divergence, temperature and surface pressure (ζ,D,T and p_*) and solved spectrally with a horizontal resolution of T21 (approximately 5.625° in latitude and longitude) on 5 equally spaced σ levels (approximately, 900 hPa, 700 hPa, 500 hPa, 300 hPa and 100 hPa height levels).

For simplicity, following the convention of Hall [2000], the equation describing the model's evolution with time can be written as

$$\frac{\partial \Psi}{\partial t} = N(\Psi) + \mathbf{f}, \tag{2.1}$$

where Ψ is the model state, representing the values of ζ, D, T and p_* in the model, $N(\Psi)$ represents all the nonlinear terms and some damping effects (the damping terms are specified in a linear form), and $\mathbf{f}$ is the forcing term, which, in this study, is time independent. To derive the forcing, a statistical equilibrium state is assumed in each winter. We do a time average and form the time-mean budget equation of (2.1)

by splitting Ψ into a long-time mean $\overline{\Psi}$ and an instantaneous perturbation Ψ'. Thus

$$\overline{\frac{\partial \Psi}{\partial t}} = \overline{N(\Psi)} + \mathbf{f}, \tag{2.2}$$

where

$$\overline{N(\Psi)} = N(\overline{\Psi}) + \overline{E(\Psi')} \tag{2.3}$$

As shown by (2.3), nonlinearity in the model can be divided into parts associated with the climatology state $\overline{\Psi}$ and eddy flux $\overline{E(\Psi')}$. If the climate system is in statistical equilibrium, or in other words, the average of the time derivative term over the averaging period is small in amplitude compared to the individual terms on the right hand side, the $\overline{\frac{\partial \Psi}{\partial t}}$ term on the left hand side of equation (2.2) can be approximated to be zero, which leaves the balance between $\overline{N(\Psi)}$ and $\mathbf{f}$, i.e.,

$$\mathbf{f} = -\overline{N(\Psi)} \tag{2.4}$$

or, using (2.3),

$$-N(\overline{\Psi}) = \mathbf{f} + \overline{E(\Psi')} \tag{2.5}$$

This, by nature, turns out to be a good approximation for the solstice seasons, but is less reliable for the equinox seasons. Inserting the observed atmospheric states (denoted by Φ) into (2.4) in place of Ψ, a time-independent "diabatic" forcing $\mathbf{f}$ is obtained in terms of the action of the nonlinear operator N on the observed states Φ, i.e., $\mathbf{f} = -\overline{N(\Phi)}$. In this thesis, $\mathbf{f}$ is calculated using daily mean observed states Φ, as described in Section 2.2. Likewise, replacing Ψ in (2.5) with Φ, the left hand side, $-N(\overline{\Phi})$ represents the maintenance of the time-mean flow against its own advective tendencies and against damping. In the atmosphere, $-N(\overline{\Phi})$ is due to "diabatic" forcing $\mathbf{f}$ and transient-eddy flux convergence $\overline{E(\Phi')}$, therefore representing the sum of these two effects. If we set $-N(\overline{\Phi})$ as forcing, this would be the appropriate forcing for a model that had no explicit representation of transient-eddy fluxes. The forcing specified in this way will be applied to the linearized model experiments wherein the climatology, $\overline{\Phi}$, about which the model is linearized, is maintained by $-N(\overline{\Phi})$. The second term, $\overline{E(\Phi')}$, often dubbed the "transient-eddy forcing", represents the effect

of the observed transient fluxes in the time-mean budget. This "eddy forcing" can be derived by subtracting the "diabatic forcing" $\mathbf{f}$ from $-N(\overline{\Phi})$, i.e., $\overline{E(\Phi')} = -N(\overline{\Phi}) - \mathbf{f}$. When the model is driven by $\mathbf{f}$, as in our nonlinear model experiments, the model must develop its own transient-eddy activity. The forcing associated with this transient activity, $\overline{E(\Psi')}$, must agree with $\overline{E(\Phi')}$ if the model is to reproduce the observed mean state, $\overline{\Phi}$.

2.2 Calculation of the forcing term

As introduced above, there are two ways to drive the model. For the full nonlinear model, only a diabatic forcing $\mathbf{f} = -\overline{N(\Phi)}$ is applied to drive the model and the the model develops its own transient-eddy activity. For the model linearized about a climatology, a forcing $-N(\overline{\Phi})$ containing both diabatic and transient-eddy effects is used. We outline the method of calculating the forcing in the following.

The effect of the N operator on any initial condition $\Psi_\mathbf{0}$ can be found by running the model without forcing for one time step, giving the instantaneous tendency

$$(\frac{\partial \Psi}{\partial t})_{unf} \approx \frac{\Psi^+_{unf} - \Psi_\mathbf{0}}{\delta t} = N(\Psi_\mathbf{0}) \tag{2.6}$$

where the subscript unf denotes an unforced integration of the model and the superscript $+$ refers to the state after one time step. The time step of integration is δt. Thus, using (2.4), $\overline{N(\Phi)}$ can be found by averaging the result of setting $\Psi_\mathbf{0} = \Phi_\mathbf{i}$, where subscript $\mathbf{i}$ identifies one realization of Φ among n observations. Thus

$$\mathbf{f} = -\overline{N(\Phi)} = -\frac{1}{n\delta t}\sum_{\mathbf{i}=1}^{n}\{\Psi^+_{\mathbf{i}unf} - \Phi_\mathbf{i}\} \tag{2.7}$$

Likewise the forcing for the linearized model $-N(\overline{\Phi})$ can be found by setting $\Psi_\mathbf{0} = \overline{\Phi}$ without stepping through the entire time series of data. Thus,

$$-N(\overline{\Phi}) = -\frac{\Psi^+_{unf} - \overline{\Phi}}{\delta t} \tag{2.8}$$

We now explain more how the model is linearized. Specifying the model state as $\Psi = \overline{\Phi} + \Psi_\mathbf{p}$, where $\Psi_\mathbf{p}$ is a small perturbation to the observed climatology, and

setting the forcing $\mathbf{g} = -N(\overline{\mathbf{\Phi}}) + \mathbf{g}'$, where $\mathbf{g}'$ is a small perturbation to the forcing maintaining the climatology $\overline{\mathbf{\Phi}}$, the model equation becomes

$$\frac{\partial \mathbf{\Psi_p}}{\partial t} = \mathbf{L}_{\overline{\mathbf{\Phi}}}(\mathbf{\Psi_p}) + \mathbf{g}', \tag{2.9}$$

where $\mathbf{L}_{\overline{\mathbf{\Phi}}}$ is a linear operator determined by the climatological state about which the model is linearized and terms of quadratic or higher order in perturbation amplitude have been neglected. Thus (2.9) is the associated time-dependent linear perturbation model. The linearized version of this model has been used by Hall and Sardeshmukh [1998] to examine the first eigenmode of $\mathbf{L}$ of the climatological mean circulation, and by Jin and Hoskins [1995] to study the direct response to a perturbation in tropical forcing. Here the same technique will also be applied to investigate the direct response to the forcings for different climate modes. It should be noted that running the model in this linearized fashion does not require changing the original nonlinear codes as long as the perturbation amplitude does not grow too large.

The data used to compute the forcing are the daily means from the NCAR/NCEP reanalysis. The period of analysis used in this study spans 51 winters (Dec.1st to Feb.28, totally 4590 days of realizations) from 1948/49 to 1998/99. Horizontal velocity (u and v), temperature and geopotential height on a 144×73 grid are linearly interpolated onto a 128×64 Gaussian grid. Orography is not represented explicitly in the model and surface pressure is calculated by integration of the barometric equation from the 1000 hPa height to sea level using the 1000 hPa temperature. In the remainder of the paper this quantity will be referred to as the sea level pressure (SLP) in both observations and model results. Other data provided on pressure surfaces are linearly interpolated onto the model's sigma levels. Since the model is solved in spectral space for ζ,D,T and p_*, the data fields are spectrally analyzed at T21 to be input into the model in terms of the spectral coefficients for ζ, D, T and p_*.

The forcing calculated using (2.7) mimics processes not explicitly included in the model code, most importantly the diabatic forcing of the atmosphere due to incoming solar radiation, latent and sensible heat release associated with deep convection and the midlatitude storm track (Hoskins and Valdes [1990]), and since the model has

a flat bottom, the effect of the missing orography. Hereafter, for the purpose of convenience, this forcing will be called "diabatic forcing" in this thesis. The forcing calculated from (2.8) for the linearized model ($-N(\overline{\mathbf{\Phi}})$) includes both the "diabatic" and "eddy" effects and will be dubbed "diabatic plus eddy forcing". Time series of "diabatic only forcing" (i.e., $-\overline{N(\mathbf{\Phi})}$) and "diabatic plus eddy forcing" ($-N(\overline{\mathbf{\Phi}})$) are obtained from the 51 years of data. Based on equation (2.5) the latter minus the former gives the time series of the "transient-eddy forcing".

Chapter 3

The Eastward Shift of the NAO

3.1 A changed regime

3.1.1 Motivation

Given the importance of the NAO for northern hemisphere (especially European) climate variability (Kushnir [1999]; Greatbatch [2000]) and the possibility that anthropogenic forcing may be implicated (Hilmer and Jung [2000]; Ulbrich and Christoph [1999]), it is important to understand what caused the eastward shift of the NAO pattern. As a starting point, we make use of correlation analysis to find some clue.

We know that the poleward eddy flux of momentum associated with synoptic storms is important for maintaining the different phases of the NAO (Limpasuvan and Hartmann [1999]; Greatbatch [2000]; Thompson et al. [2003]). This prompted us to examine the relationship between the NAO and storm activity over the North Atlantic to see if this relationship can shed any light on the eastward shift. It turns out that the first mode of North Atlantic storm track activity defined by Rogers [1997] is associated with a dipole pattern of SLP that has some similarity to that of the NAO. Rogers' storm track mode is defined as the first rotated empirical orthogonal function (REOF) of the root mean square of high-pass SLP variability. Rogers did not identify this SLP pattern as the NAO because its centers of action are more eastward shifted

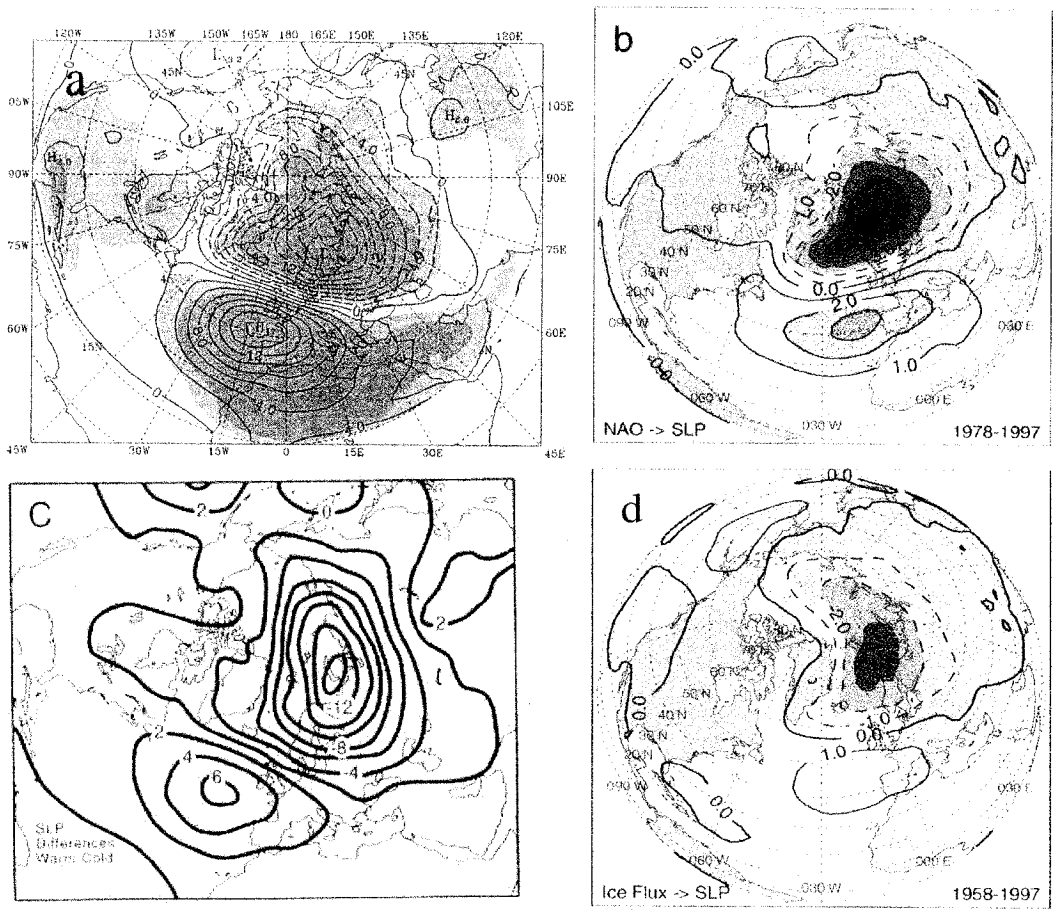

Figure 3.1: (a) The mean SLP difference (mb) occurring between months with extreme positive and negative scores of the first rotated pattern of the combined principal component analysis (CPCA) of monthly Atlantic root-mean-squares of high-pass filtered SLP and monthly mean SLP, 1900-1992 (from Rogers [1997]). Lighter and darker shading represent areas where the differences in pressure are statistically significant with 95% and 99% confidence; (b) Regression pattern of the NAO index against winter (DJF) mean SLP (hPa) during 1978-1997 (from Hilmer and Jung [2000]). Statistically significant slope parameters (5% confidence level) are colored; (c) The monthly mean SLP differences between the 30 warmest and the 30 coldest months in Siberia since 1950 (from Rogers and Mosley-Thompson [1995]); (d) The regression pattern of SLP against the time series of modeled ice volume export through Fram Strait over the period 1958-1997 (from Hilmer and Jung [2000]).

compared to the prototype NAO. This SLP pattern (see Figure 3.1a) nevertheless bears a great resemblance to the NAO pattern during the decades of 1978-97 (see Figure 3.1b), with one center of action over the Bay of Biscay, and the other over northern Scandinavia and the Barents Sea. This hints at a special role of Rogers' leading mode of NAST activity in the eastward shift of the NAO. The relationship between this storm track mode and the NAO will be the focus of this correlation analysis.

Meanwhile, the mild Siberian winters during the 1980's are ascribed by Rogers and Mosley-Thompson [1995] to an increase in cyclone activity in the northeast Atlantic Ocean and the high Arctic Oceans. Cyclone activity in these areas is a feature of the positive phase of the first REOF of storm activity found by Rogers [1997] as referred to above. Furthermore, the SLP difference between extreme warm and cold Siberian winters shown by Rogers and Mosley-Thompson [1995] (see their Figure 3.1c) has a strong similarity to the SLP pattern (Figure 3.1d) associated with ice export through Fram Stait shown by Hilmer and Jung [2000]. It follows that ice export through Fram Stait, Siberian winter temperature (SWT), and cyclone activity over the high latitude North Atlantic, all have some connection with the NAO and its eastward shift, although the precise relationship is unclear. Here we use cross-correlation analysis to clarify their relationship.

3.1.2 Data

The basic data set used here is 47 years (1953-1999) from the NCEP/NCAR reanalysis (Kalnay et al. [1996]). Only winter months (December, January and February; DJF) are considered. Kwok and Rothrock [1999] and Kwok [2000] have demonstrated a high correlation (r = 0.89) between the area flux of ice through Fram Strait and the average monthly gradient in SLP across the Strait. We therefore use the winter mean (DJF) SLP difference across the Strait ($(81°N, 15°W)$ minus $(80°N, 10°E)$), normalized with respect to its own standard deviation, as a proxy for ice export (denoted by IF). Following Hurrell [1996], the NAO index (denoted by NAO) is

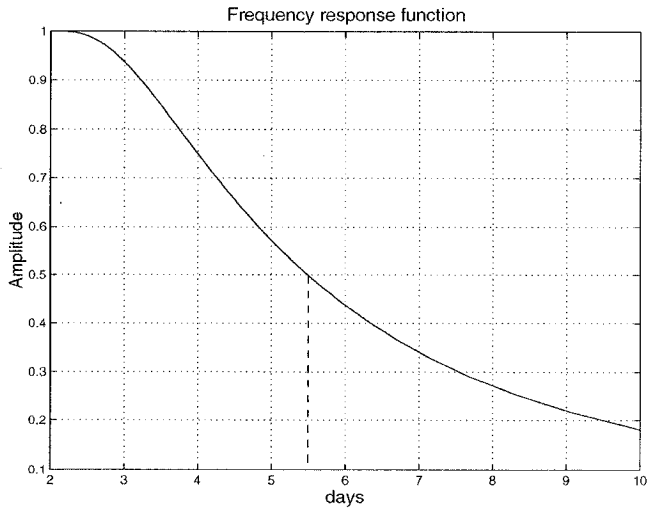

Figure 3.2: Frequency response function of the filter applied on the 12Z SLP data. The half-power cutoff is at 5.5 days as marked by the dashed line.

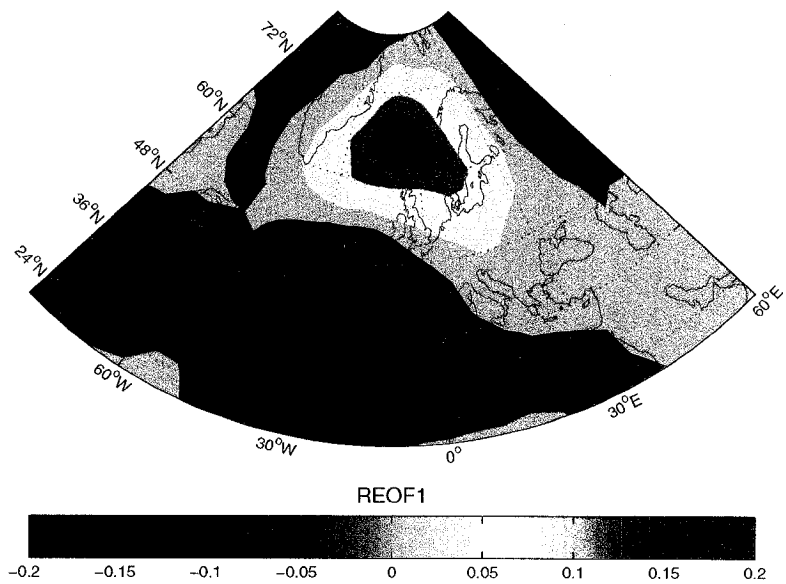

Figure 3.3: The first Rotated Empirical Orthogonal Function of the root mean square high-pass filtered SLP during the winter months (DJF) from 1953-1954 to 1998-1999. The REOF analysis is applied over a region shown in the figure, that is spanning from 20° to 80°N, and from 80°W to 60°E. The pattern is non-dimensional.

defined as the difference in normalized SLP anomalies between Lisbon, Portugal and Stykkisholmur, Iceland. The only difference from Hurrell [1996] is that we use DJF for the winter season rather than DJFM. The index of Siberian winter temperature (SWT) is simply a normalized time series of the area mean temperature over Siberia spanning $55° - 70°N$, $70° - 100°E$. It is calculated by using the monthly mean 1000 hPa temperature product from the NCEP/NCAR reanalysis data. To compute a storm index, we follow the procedure of Rogers [1997] and apply it to once daily 12z SLP data from the NCEP/NCAR dataset spanning the period 1 December–28/29 February from 1953-1954 to 1998-1999. The data are high-pass filtered using a binomial filter. The frequency response function of the filter is shown in Figure 3.2. The filter has maximum response in the 2-8-day period range (with half-power cutoff at 5.5 days), typically corresponding to the passage of synoptic systems. A varimax rotated empirical orthogonal function analysis (REOF) was performed on monthly rms values of the high-pass filtered data extending from 20° to $80°N$, and from $80°W$ to $60°E$. The first component pattern is a dipole centered in the northeast Atlantic and Norwegian Sea and over the eastern Atlantic around Portugal (Figure 3.3). It is this storm activity mode that is associated with the SLP pattern shown in Rogers (1997)'s Fig. 6 (i.e., Figure 3.1a here), and which resembles the shifted NAO pattern during 1978-1997. We obtain a winter storm index, ST, by averaging the principal component time series for the three winter months and normalizing so as to be consistent with Rogers' index. Rogers' index spans the winter months from 1900 to 1992. During the overlap period (1954-1992), the correlation coefficient between his winter index and ST is 0.94, the difference from a correlation of 1 being attributable to the different data set used here. This verification allows us to reconstruct a longer storm index by connecting our 1954-1999 index to Rogers' index truncated after 1954. All four climate indices are shown for the period 1954-99 in Figure 3.4a.

We also make use of the monthly mean SLP data set from the Climate Research Unit at the University of East Anglia (UEA), UK. This SLP record is 123 years long spanning from 1873 to 1995 and available on a 10° longitude × 5° latitude grid.

However, because of lack of data coverage over the Eurasian continent in the early part of the record, we use only data after 1940.

3.1.3 Results

The running cross-correlations between pairs of indices using a window-length of 20 years are shown in Figure 3.4b (choosing window lengths of 15 or 25 years does not significantly change the results). The correlations of the ice flux proxy with the other three indices are depicted by solid curves. All three solid curves show a rapid rise from near zero correlation in the first 20 year period centered around 1960 to much higher correlations that jump above the 1% significance level (using Student's t-test) around 1980. This is the same behavior as seen in Fig. 10 of Jung and Hilmer [2001] who compared model-simulated ice volume export through Fram Strait with the NAO index. The jump in the correlations shown by all three solid curves suggests the establishment of a new climate regime in which Fram Strait ice export suddenly becomes phase locked with the NAO, the storm index, and Siberian winter temperature, having previously been unconnected to any of these variables.

Note that the NAO is most highly correlated with the storm index. What is interesting, however, is that the link between the NAO and this particular mode of storm activity (the first rotated EOF of rms high-pass variability) did not hold up in the early part of the century. Figure 3.5c shows the same running cross-correlation, but this time between the 100 year extended storm index (Figure 3.5b, using Rogers' data before 1954) and Hurrell's winter (DJF) NAO index (Figure 3.5a) over the period 1900-1999, the dashed curve using Rogers' data after 1953. There is a long-term increasing trend during all the 20th century, and it is only after the early 1960s that this mode of storm activity became significantly linked (at the 1 % level) to the NAO. Indeed, in the early part of the century, the link was weak. Figure 3.6a shows the result of regressing the UEA winter mean SLP on the storm index using data from 1940 to 1995. The pattern is very similar to Rogers [1997]'s SLP pattern obtained from CPCA (Figure 3.1a). In particular, there is a northern center over

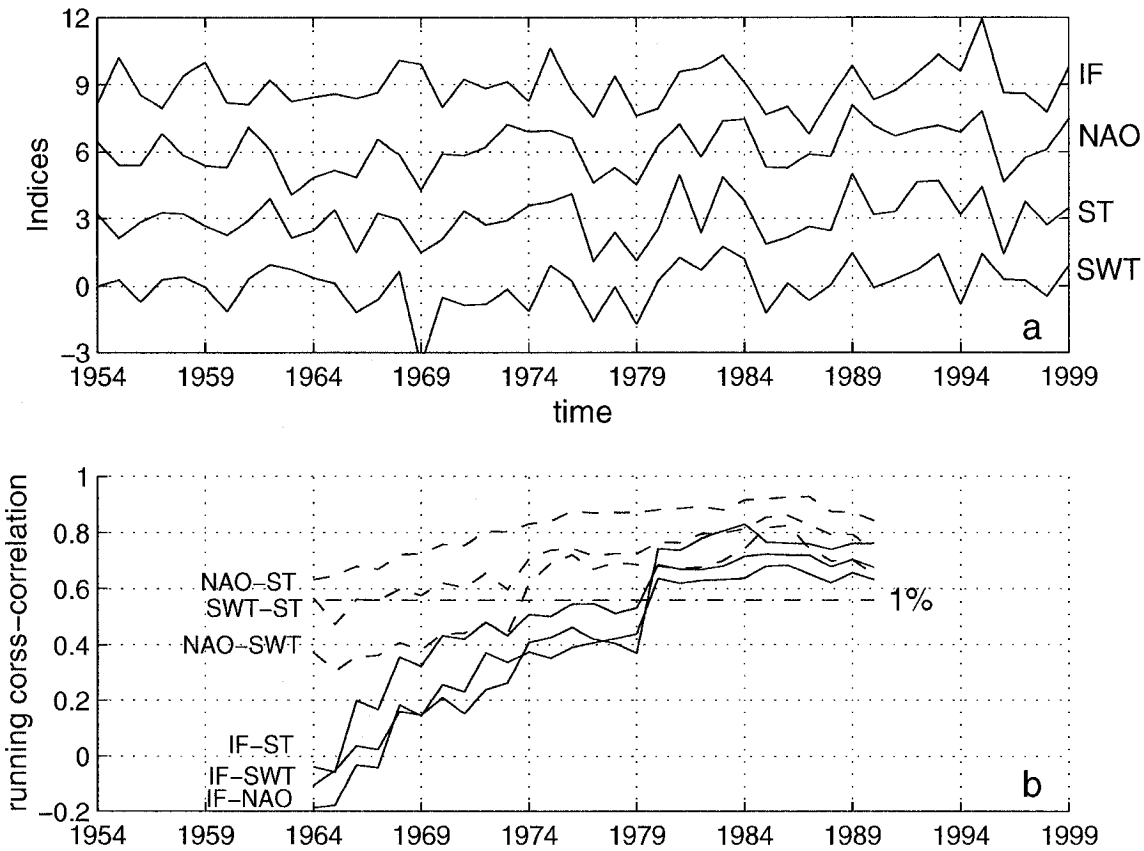

Figure 3.4: (a) Winter mean(DJF) time series of the ice flux proxy IF, the NAO index NAO, the storm index ST, and the Siberian winter temperature index SWT. Note the vertical offset of 3 units between indices for plotting purposes; (b) Running cross-correlation functions (20 year window) between every two time series in a). The 1%-confidence level (dash-dot) indicates correlation coefficients which are significantly different from zero.

northern Scandinavia and the Barents Sea and a (weak) anomalous south-north wind component over Fram Strait. Given the high correlation (above 0.8) between the storm index and the NAO index during the 1980's and 90's it is not surprising that the pattern in Figure 3.6a is also very similar to the shifted NAO pattern shown in Figure 3.6b. Viewed in this way, the eastward shift in the NAO can be interpreted as the result of the century long increase in the correlation (see Figure 3.5c) between the NAO index and the principal component of Rogers' first rotated EOF of rms high-pass variability. There is a controversy that seems not to fit in with this view and entails an explanation. As shown by the curve *NAO-ST* of Figure 3.4b, the correlation between the NAO and the storm track index is also significant in P1, though weaker than in P2, while only in the later period does the shift happen. This can be explained by the fact that Rogers' first storm activity mode accounts only for 40% of variance of the NAO during P1, in contrast to 70% during P2. Indeed, during P1, some other modes of North Atlantic storm track variability are also important for the NAO variability (not shown).

We now discuss the other two dashed cross-correlation curves shown in Figure 3.4b, *SWT-ST* and *NAO-SWT*. The link between the cyclone activity and Siberian winter temperature has been addressed by Rogers and Mosley-Thompson [1995]. These authors attributed the mild Siberian winters of the 1980's to an increase in the frequency of cyclones that enter the extreme northeastern Atlantic and traverse the Barents and Kara Seas bringing strong westerly flow into Siberia along with extensive cyclone warm sectors. The high correlation (greater than 0.7) between the storm index and SWT since the mid 1970s concurs with this view. Since they were not aware of the shift in the NAO, Rogers and Mosley-Thompson did not relate the mild Siberian winter temperatures to the NAO. Curve *NAO-SWT*, denoting the correlation between SWT and the NAO index shows that the 20 year correlation became significantly different from zero (at the 1% level) sometime during the 1970's, and that the NAO accounts for as much as 60% of the variance of SWT in recent decades.

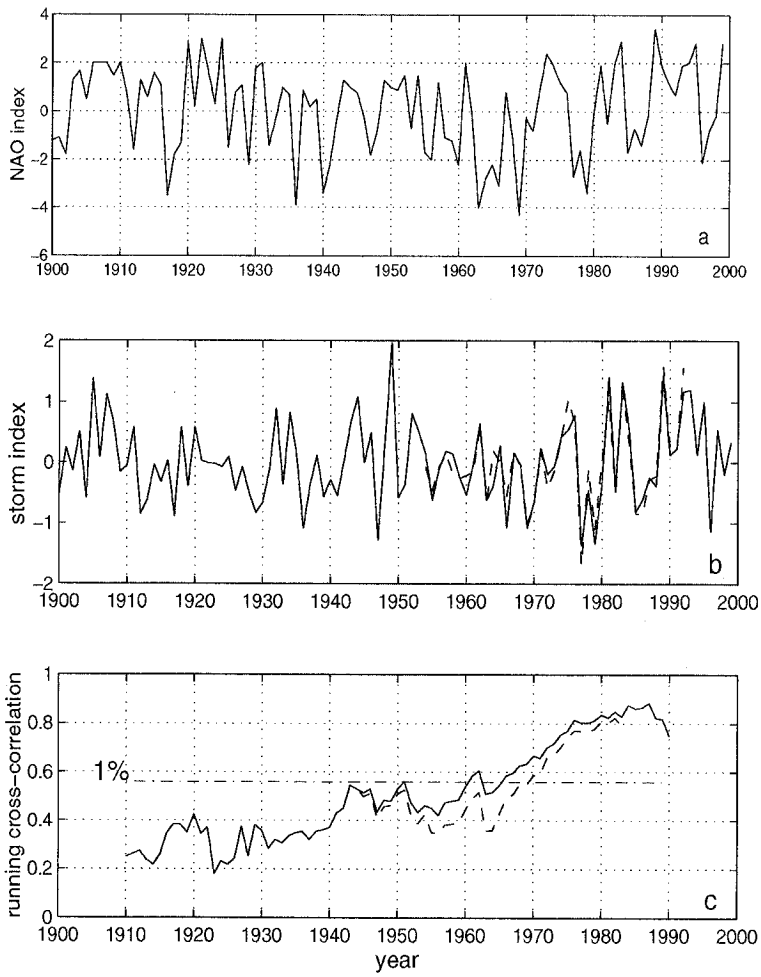

Figure 3.5: (a) Hurrell's winter (DJF) NAO index during 1900-1999; (b) Storm index from 1900 to 1999 reconstructed by connecting Rogers' 1900-1953 time series to the index calculated by using NCAR/NCEP 12z SLP from 1954 to 1999. Dashed curve is the later part of Rogers' index (1954-1992). (c) Running cross-correlation function (20 year window) between the storm index and Hurrell's winter (DJF) NAO index during 1900-1999. The dashed cross-correlation function comes from using the dashed part of Rogers' storm index shown in (b). The straight dash-dot line is the 1%-confidence level.

The high association of SWT with the NAO is further verified by the great resemblance between the SLP regression pattern (not shown) against SWT and the NAO pattern during the period of NAO shift.

We may summarize the whole story as follows. Since the mid 1950s, the first REOF mode of the North Atlantic storm track activity has become more and more dominant over the NAO, with the result that the NAO spatial pattern shifted eastward to imitate the SLP pattern of the first mode of storm activity. After 1970's, when a shifted NAO pattern was established, the NAO index, this storm activity mode, the Fram Strait ice flux proxy and Siberian winter temperature all started to be significantly correlated with each other. This suggests the emergence of a new, spatially coherent climate regime during the last few decades of the 20th century.

To gain more confidence in the NAO shift, in the coming sections, we will put our investigation in a framework governed by physical laws of the atmosphere to see whether the shift in the NAO pattern between P1 and P2 can be reproduced by the simplified atmospheric model (Hall model) that was introduced in Chapter 2. If the model can do so, it suggests the shift comes from certain physical rationale, adding weight to the robustness of the shift. Further, a series of ideal model experiments will be carried out in order to shed light on the mechanism of the shift.

3.2 Simulating the NAO and its shift

Ensembles of experiments are carried out with the Hall model for each winter separately using the model forcing diagnosed as described in Section 2.2. Each ensemble consists of 30 ensemble members, which differ only in the choice of initial condition, these being chosen randomly from the 4550 realizations of winter daily mean data available in the NCAR/NCEP reanalysis. Each ensemble member is integrated for 4 months and the analysis is carried out on the final 3 months. The NAO index is calculated using the difference in normalized SLP anomalies between the model's Gaussian grid boxes located over Portugal and Iceland respectively, and compared with

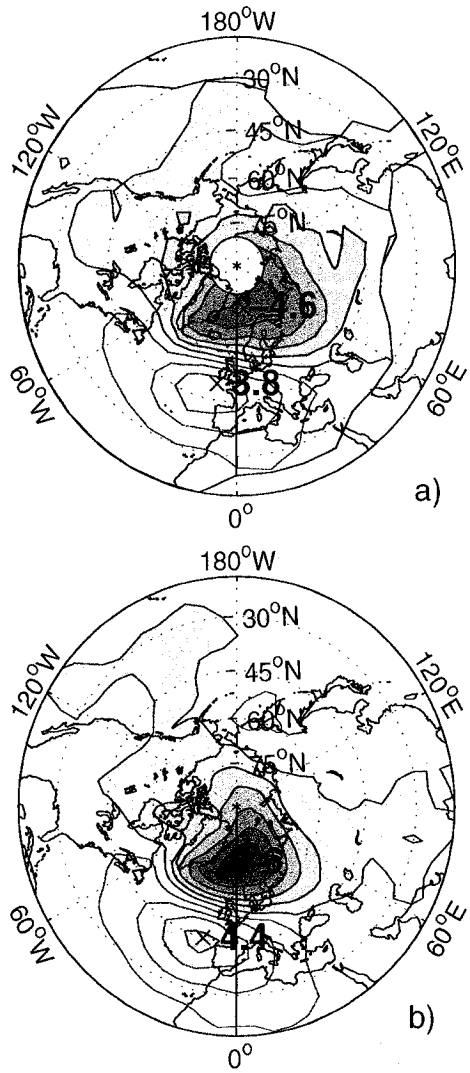

Figure 3.6: (a) Pattern obtained by regressing UEA winter (DJF) mean SLP against the reconstructed storm index using data from 1940 to 1995; (b) Pattern obtained by regressing NCAR/NCEP winter mean SLP against the NAO index using data from 1978-1997. Contour interval is $1hPa$.

the NAO signature in the NCAR/NCEP reanalysis projected onto the same Gaussian grid. In all cases the SLP anomalies used to calculate the NAO index are normalized by the standard deviation of the winter SLP anomalies in the NCAR/NCEP data set so that the modeled NAO index can be compared directly with the observed one in amplitude. The NAO index calculated from the NCAR/NCEP reanalysis is essentially the same as that of Hurrell [1995b], the correlation between the two indices being 0.95.

Due to the inherent simplicity of the model, we are able to run large member ensembles (typically 30 members), with multiple forcing regimes. This represents a vital improvement in statistics over what a conventional AGCM may offer. As well, since the forcing in our model is diagnosed from data, our model has the advantage of eliminating some of the uncertainty in the way fully interactive AGCM's compute their forcing.

Figure 3.7 shows a plot of the model's NAO index for the ensemble mean (red line) and the observed NAO index calculated from the NCAR/NCEP reanalysis (green line). The agreement between the model results and the reanalysis is remarkable. The NAO index for the ensemble mean and that calculated from the reanalysis correlate at 0.8, significantly different from zero at the 1% confidence level. Likewise, the average correlation between an individual ensemble members's NAO index with the NCAR/NCEP NAO index is 0.74. As well, the amplitude of our model response is comparable to that in the observations. The linear trend of the NAO is depicted by a straight line which least squares fits the NAO index. The simulated ensemble mean trend (red line) overestimates the observed trend (green line) by a factor of 2. We also regressed the model's ensemble mean SLP against the ensemble mean NAO index and obtain a pattern (Figure 3.8b) in amplitude and shape similar to that of the reanalysis data (Figure 3.8a). As such, making use of the forcing diagnosed from the data, the Hall model is even more skillful in reproducing the observed NAO index than the model simulations driven by specified boundary forcings, as in Rodwell et al. [1999] and Mehta et al. [2000].

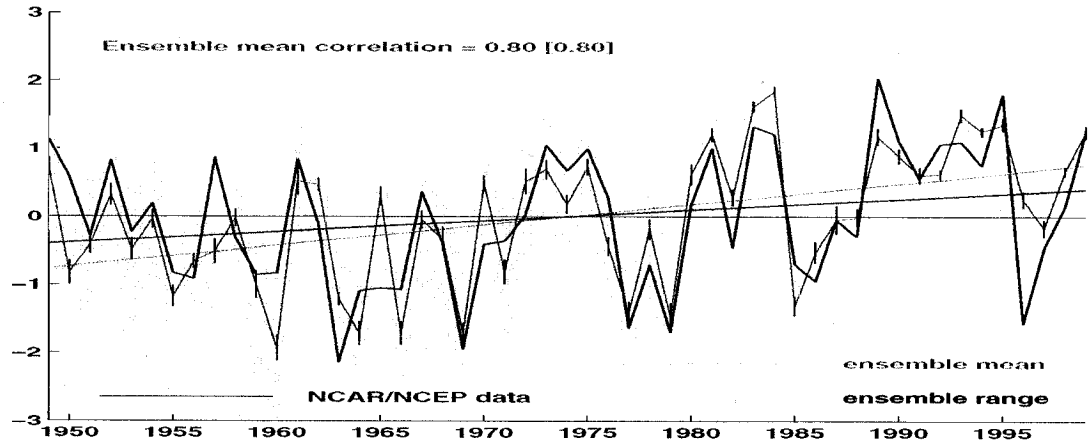

Figure 3.7: Time series of the NAO index. The green line is the observed NAO index computed from the NCAR/NCEP data, and the red line is the NAO index computed from the ensemble mean SLP field produced by the model. The shading indicates the spread in the individual ensemble members. The straight lines indicate the trend. The correlation coefficient between the ensemble mean and the observed NAO index is displayed as red numbers. The bracketed number is the correlation of the detrended time series.

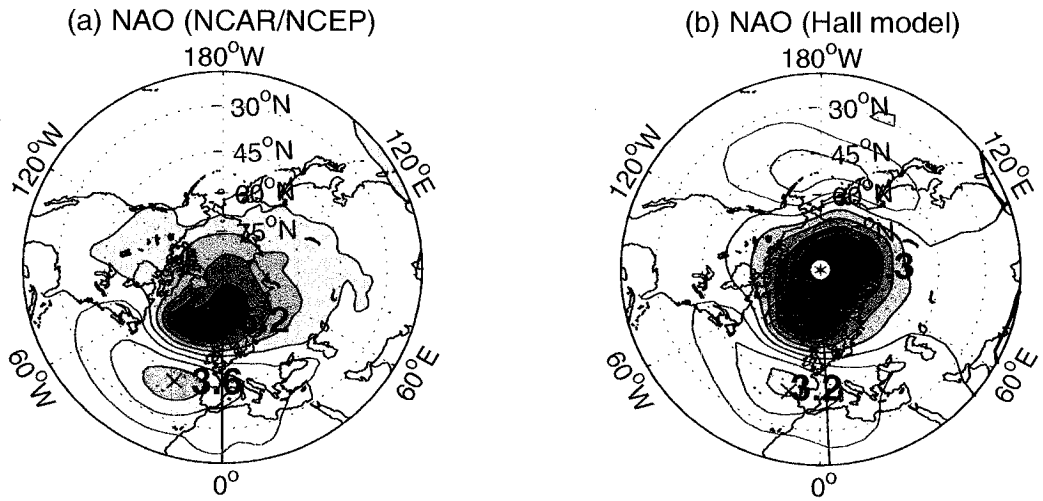

Figure 3.8: (a) Linear regression of the observed SLP (NCAR/NCEP) against the observed NAO index; (b) Linear regression of the model ensemble mean SLP against the model NAO index. The amplitudes correspond to one standard deviation of the NAO index. Contour interval is 1hPa.

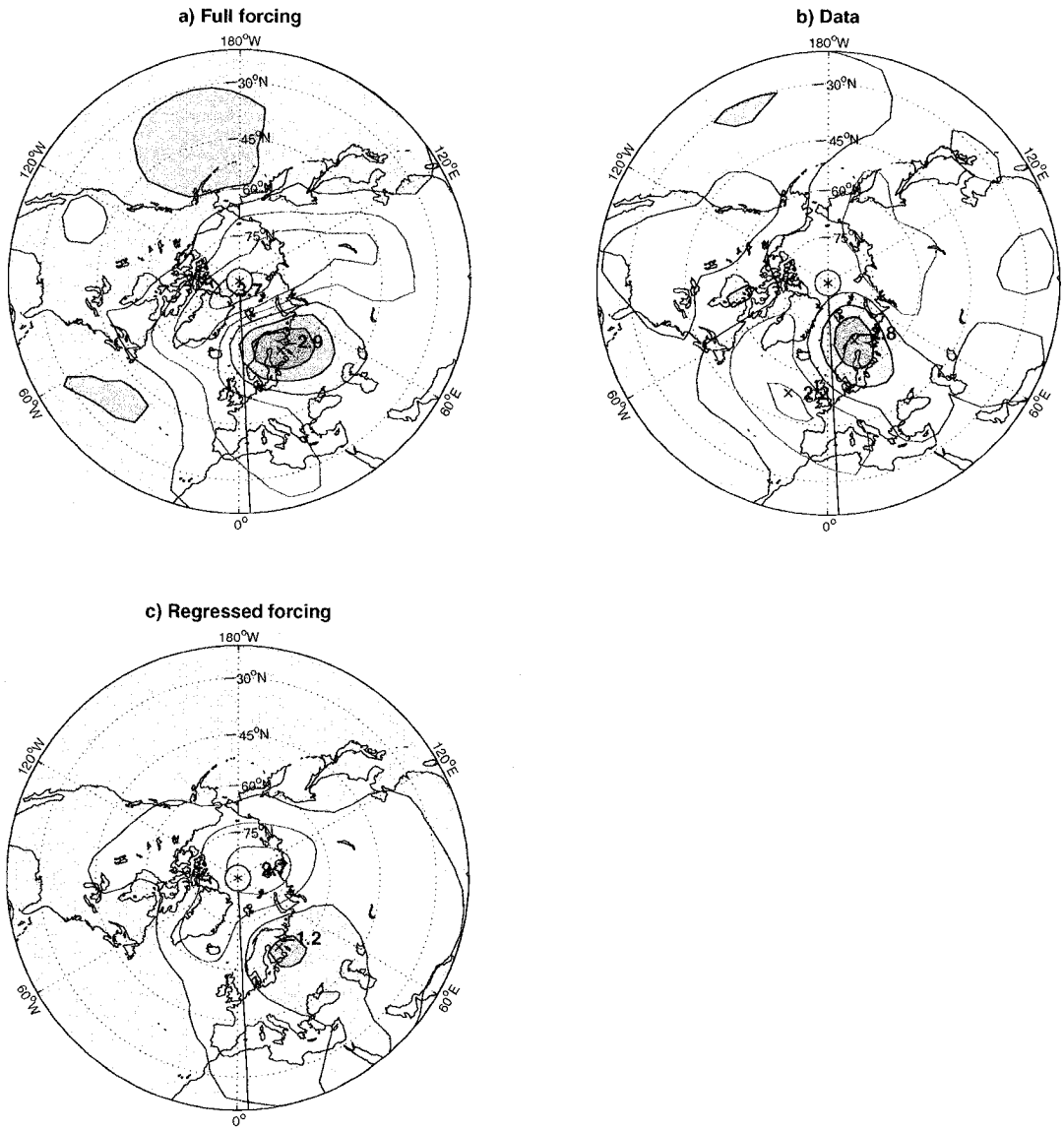

Figure 3.9: Difference between the regression patterns of winter mean SLP against the NAO index for periods 1978-1997 minus 1958-1977. (a) Full global forcing case; (b) NCAR/NCEP reanalysis data; (c) Regressed forcing case with the strength of the forcing specified as the observed NAO index. Contour interval is 1hPa.

Seeing the model's skill in reproducing the variability of the NAO, we can move on to analyzing the pattern shift of the NAO, a second order variability associated with the NAO. Following Hilmer and Jung [2000], we regress the detrended ensemble mean SLP anomalies against the detrended ensemble mean NAO index separately for the two periods 1958-77 and 1978-97 considered by Hilmer and Jung [2000]. The difference between those two fields is plotted in Figure 3.9a, as well as the result of the same analysis applied to the NCAR/NCEP data (Figure 3.9b). The generally good agreement between model and observations shows that our model captures the eastward shift.

3.3 Regressed forcing experiments

From the model results in the previous section, we see that the NAO variability at interannual time scales is substantially determined by the specified forcing. However, the role of the model forcing in the dynamics of the shift is not clear in the context of the previous ensemble experiments because the model response is nonlinear. To unravel the effect of model nonlinearity, two sets of idealized experiments are carried out using the special setup of the model forcing described as follows. First, the forcing for each winter is regressed against the observed NAO index[1]. Multiplying the regressed forcing pattern by a specified value for the NAO index, and adding to the climatological forcing which is the average of the forcing of all the 51 winters, then gives a forcing to drive the model. Thus, in these experiments, the pattern of the anomalous part of the forcing is fixed in shape and any distortion in the pattern of the NAO response can be attributed only to the nonlinear dynamics intrinsic to the model; that is eddy fluxes and changes in the mean flow from winter to winter.

In the first set of experiments, we multiply the regressed forcing pattern (i.e., NAO-related forcing) by the value of the observed time series of the NAO index, giving a time series of 51 model forcings corresponding to the observed time series of

[1]Index used is the DJF seasonal index as found on http://www.cgd.ucar.edu/~jhurrell/nao.html

the NAO index from 1948/49 to 1998/99. For each specified value of the NAO index, 30 ensemble runs are carried out. The analysis is based on the last 3 months of the total 4 month run.

In this set of experiments, the simulated NAO index is highly correlated with the observed index at 0.98, suggesting the overwhelming dominance of the regressed part of the forcing for determining the NAO in the model, lending confidence to the way in which we extract the model forcing associated with the NAO. As to the difference in the regressed SLP pattern between P1 and P2, in this case, as shown in Figure 3.9c, there is again good agreement with the observed one (Figure 3.9b), except for a reduction in amplitude. Note that the spatial pattern of the anomalous forcing in this experiment is the same for every year, differing only in its amplitude which is given by the observed NAO index. If the dynamics is linear, then the model response would have the same spatial structure in every year and there would be no eastward shift. The presence of the difference pattern in Figure 3.9c can therefore only be attributed to nonlinear dynamical processes.

In the second set of experiments, it is not the observed NAO index but a series of specified NAO indices that defines the strength of the NAO forcing. An ensemble of experiments are carried out for each specified value of the NAO index from -5 to 5 at increments of 0.2. The purpose of specifying the NAO index in this way is to see how the NAO response changes systematically with different strength of NAO forcing.

First, we compare the NAO index computed from the ensemble mean with the originally assigned NAO index. The two are generally in good agreement (Figure 3.10), although there is a tendency for the ensemble mean NAO index to be weaker than the specified index for all positive values and all values less than -1 of the specified NAO index. Clearly the discrepancy is an another aspect of nonlinear behavior of the model.

Next we analyze how the spatial structure of the NAO changes with the strength of the forcing. The first step is to define a linear NAO response pattern (Figure 3.11) by regressing the ensemble mean SLP against the specified NAO index. The pattern

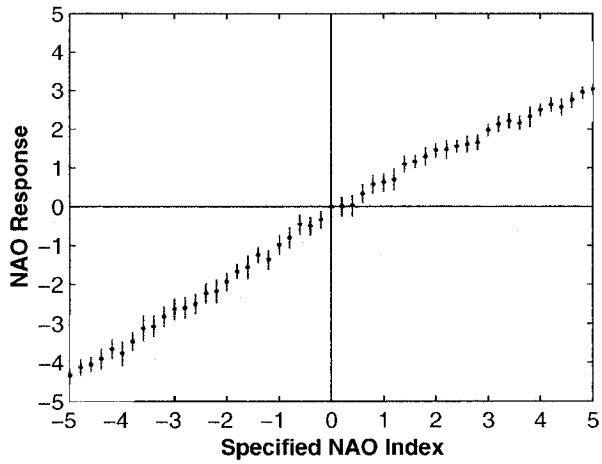

Figure 3.10: Plot of the model NAO index computed from the ensemble mean SLP as a function of the specified NAO index. The shading shows the range of spread of the individual ensemble members. The vertical red bar denotes the 95% significance interval for the ensemble mean NAO index.

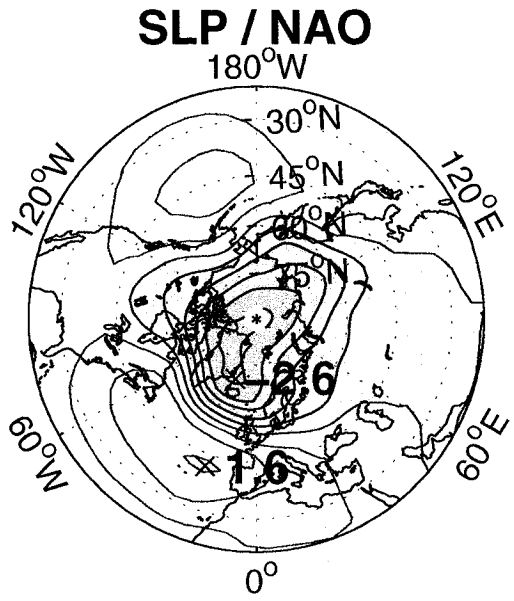

Figure 3.11: Linear regression of the ensemble mean SLP against the specified NAO index for the second set of regressed forcing experiments. The plot is normalized to correspond to a specified NAO index of +1. Contour interval is 0.5 hPa.

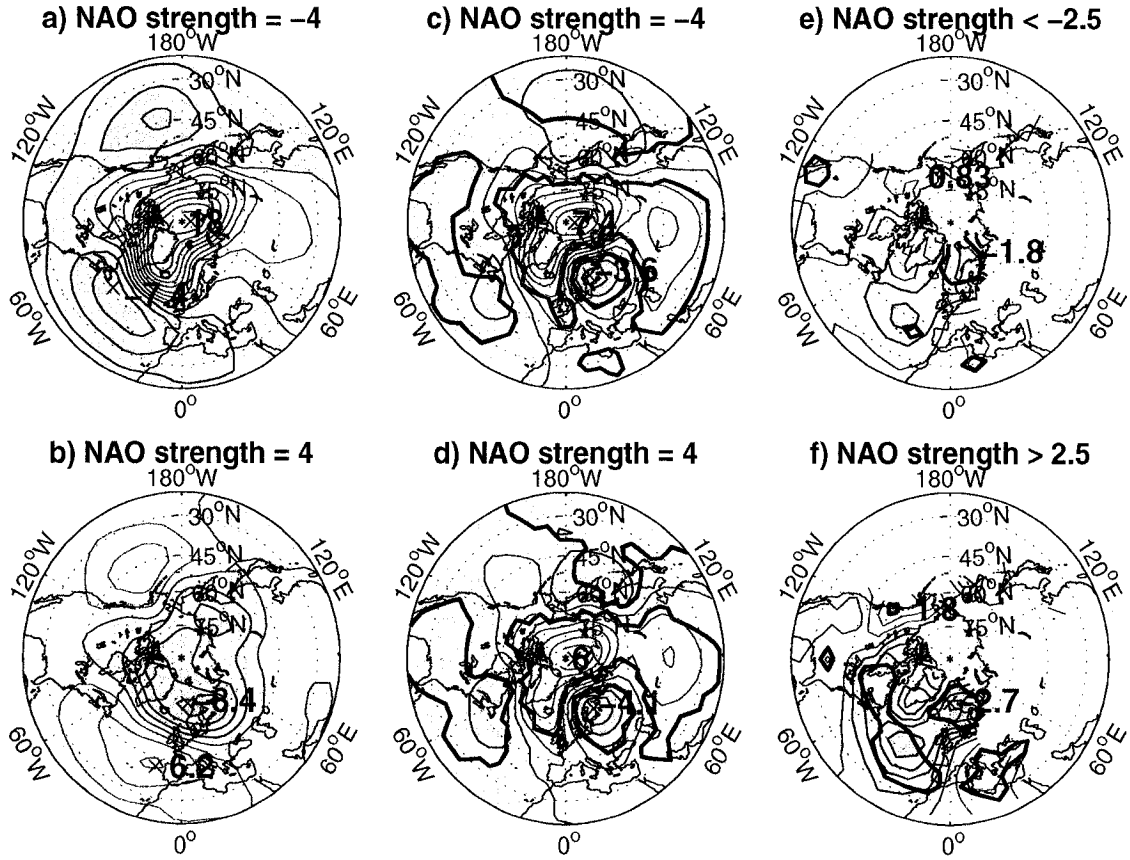

Figure 3.12: (a) Plot of the ensemble mean SLP anomaly for a specified NAO index of -4. Anomalies are expressed as departures from climatology (the ensemble mean with a specified NAO index of 0). Contour interval is 2hPa; (b) Similar to (a), except for specified NAO index of +4; (c) and (d) Nonlinear component of SLP response in (a) and (b), respectively. Plotted is the difference between the SLP anomaly in (a) and (b) and the product of the specified NAO index with the regressed pattern shown in Figure 3.11. Regions significantly different from zero at the 5% confidence level, as determined by a t-test using all 30 ensemble members, are confined within the heavy black contour lines. Contour interval in (c) and (d) is 1hPa; (e) Observed departure from linearity for NAO index less than -2.5. Plotted is the composite SLP departure from climatology minus the product of the composite average NAO index and the pattern obtained by linear regression of the winter mean SLP against the NAO index for the whole data set. Regions significantly different from zero at 10% confidence level are confined within the heavy black contour lines. Contour interval is 0.5hPa; (f) Similar to (e), except for NAO index greater than +2.5.

is very similar to the standard SLP pattern associated with the NAO (Hurrell [1995b], see also Figure 3.8a). Multiplying this regression pattern by the specified NAO index gives the expected linear response to that forcing. Nonlinearity distorts this pattern, as illustrated in Figures 3.12a and 3.12b where we show the ensemble mean SLP for specified NAO indices of +4 and −4 as a departure from model climatology (the ensemble mean with a specified index of 0), and in Figures 3.12c and 3.12d which show the difference from the expected linear response. The similarity of the difference pattern in Figures 3.12c and 3.12d is remarkable, and is typical of the model behavior for absolute values of the specified NAO index above 2. Repeating the calculation of the nonlinear distortion pattern for each individual ensemble member, we are able to perform a local t-test. The regions which are significantly different from zero at 5% confidence level are denoted by heavy black contour lines in Figures 3.12c and 3.12d.

Both extreme positive and extreme negative values of the specified NAO index are associated in the model with anomalously low pressure over Scandinavia and anomalously high pressure over southern Greenland. The result is an eastward shift in the spatial pattern of the NAO in association with anomalously high index, and a westward shift in association with anomalously low index, as can be seen by comparing Figures 3.12a and 3.12b with Figure 3.11 (bearing in mind that when the NAO is negative, the positive and negative contours in Figure 3.11 are reversed). Furthermore, the patterns in Figures 3.12c and 3.12d are very similar to the observed change in the SLP pattern associated with the NAO between P1 and P2 (Figure 3.9). Thus we suggest that the eastward shift in the NAO pattern between P1 and P2 is a consequence of the high index during P2 (average DJF index of 0.48) versus the low index of P1 (average DJF index of -0.74), which implies a difference in interannual regression patterns between P1 and P2 akin to the sum of Figure 3.12c and 3.12d.

In order to quantify the amplitude of the spatial pattern associated with the nonlinear distortion we calculate a shift index, which is simply the SLP difference between $60°N/50°W$ and $65°N/25°E$, the approximate centers of the anomalous high over southern Greenland and the anomalous low over Scandinavia in Figures 3.12c

and 3.12d. Figure 3.13 shows that the relationship between the shift index and the specified NAO index is predominantly quadratic.

To see if the quadratic relationship holds up in the observations, we analyze monthly mean SLP data for the winters (defined as December-March) of 1873-74 to 1994-95 using the University of East Anglia (UEA) SLP data (Jones [1987]). We first use linear regression to find the standard SLP pattern associated with the monthly NAO variability, a counterpart of Figure 3.11. Then, for months with mean NAO index both below -2.5 and above 2.5, composite fields of anomalous SLP (departure from each month's climatological SLP) are obtained. The linearly regressed pattern is then multiplied by the average NAO index for each composite and removed from the SLP composites to produce Figures 3.12e and 3.12f. Regions significantly different from zero at the 10% level (using Student's t-test) are denoted by the heavy black contour line. Note that due to the limited spatial coverage of the earlier data record, only the contours over the North America and the Euro-North Atlantic regions are plotted in Figures 3.12e and f. We see that in the observations (Figures 3.12e and 3.12f), as in the model (Figures 3.12c and 3.12d), the departure from linearity is similar for both large positive and large negative NAO index, although there are differences in the details of the spatial pattern associated with the model compared to the observations. Nevertheless, for both extremes, the departure from linearity shows anomalously low pressure over Scandinavia and relatively higher pressure over Southern Greenland compared to Scandinavia in both the model and the observations. Note however, only the low pressure over Scandinavia differs significantly from zero. Observational estimates are also made of the shift index displayed in Figure 3.13. Both UEA and NCAR/NCEP data sets lend support to the finding from the model: eastward shift for positive NAO values and westward shift for negative values. In view of the quadratic relationship between the shift pattern (which is characteristic of a northerly wind anomaly along the east coast of Greenland) and the NAO index, it may not be a coincidence that the Great Salinity Anomaly of the 1960's and 1970's (Dickson et al. [1988]) has been associated with anomalously large ice export

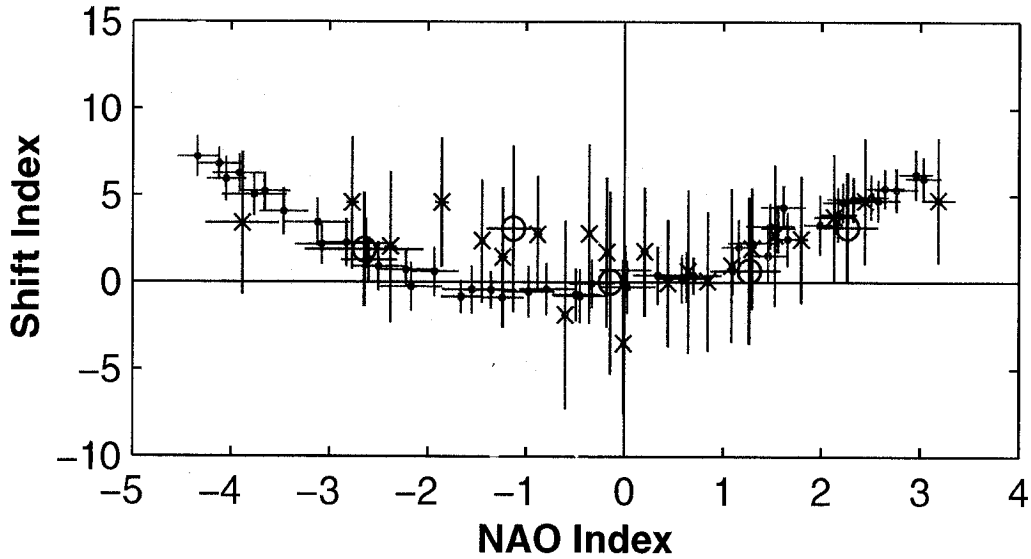

Figure 3.13: Plot of the shift index as a function of NAO index. Red cross hatches are ensemble mean shift index versus ensemble mean NAO index, with shaded regions showing the range of the shift index for each each ensemble. Blue cross hatches (○) are computed using 50 winters of the NCAR/NCEP data set sorted by NAO index into 5 bins of 10 members each, while green cross hatches (×) are for the East Anglia data set sorted into 22 bins of 22 members each. Cross hatches denote the 95% significant interval for the ensemble or bin mean.

through Fram Strait during the extreme negative NAO winters of the late 1960's (e.g., Aagaard and Carmack [1989]; Häkkinen [1993]).

Most recently, Cassou et al. [2003] (see also Hurrell et al. [2003]) applied a clustering algorithm over the Atlantic domain to identify winter climate regimes using monthly mean SLP data from 1900 to 2001. Two of the regimes correspond to the positive and negative phases of the NAO. Remarkable spatial asymmetries are found between the two NAO regimes. In particular, the main difference in the northern center is the northeastward extension of SLP anomalies during the months when the NAO is in its positive regime. In addition, the authors emphasized that these spatial asymmetries are not dependent on the analysis period: they are evident in subperiods of the ~100-year long SLP data set. The same results are obtained when the NAO

index is defined as the PC time series of the leading EOF of Atlantic SLP. These results overlap our notion of "quadratic relationship" as implied by Figures 3.12 and 3.13 and provide further observational evidence for it.

3.4 Linearized model experiments

As noted above, by assigning the strength of NAO related forcing in the regressed forcing experiments to be the observed NAO index, the first set of idealized experiments captures only about a half of the amplitude of the observed shift pattern (Figure 3.9c). It follows that the amplitude of the shift in the observed pattern is not fully explained by the nonlinear dynamics unraveled by the idealized model experiments. In the regressed forcing experiments, the spatial structure of the NAO-related model forcing is fixed. However, since the diabatic forcing due to latent heat release in the storm track depends on the storm track itself (Hoskins and Valdes [1990]), we expect in reality the forcing seen by the model during P1 to be different from that seen during P2. Therefore, account should also be taken of the effect of changing diabatic forcing between P1 and P2 to fully understand the shift. Thus, in a framework of linear dynamics, we investigate the NAO pattern of interannual variability, considering the effects of different diabatic forcing, eddy forcing and advection by the different mean states during P1 and P2.

First, we obtain the NAO related "diabatic plus eddy forcing" for P1 and P2 by regressing the $-N(\overline{\Phi})$ forcing (see Section 2.2) against the observed NAO index separately for each of the P1 and P2 periods. In the same way, the NAO related "diabatic forcing" (i.e., $-\overline{N(\Phi)}$) was also derived for each period. As indicated by (2.5), subtraction of the "diabatic forcing" from the "diabatic plus eddy forcing" gives the NAO related "eddy" forcing. In order to take into account the advection by the background flow, the model is initialized by certain climatological mean states (denoted by $\overline{\Phi}_c$) maintained by a prescribed climatological forcing, which is calculated using (2.8), but with $\overline{\Phi}$ set to be $\overline{\Phi}_c$. The NAO regressed forcing, as a perturbative

forcing is then added to the climatological forcing after being weighted by 0.1. This small weighting will make the perturbative part of the response several orders smaller than the climatological part so as to delay the onset of baroclinic instability and not to interfere with the basic balance between the initial climatological state and the climatological forcing. The departure from the climatological state is then the direct linear response to the perturbative forcing.

Three pairs of experiments are conducted for P1 and P2. The setup of these experiments is summarized in Table 3.1. In the first two pairs, the model is linearized about the climatology for the whole 1949-99 period, and the direct responses to the NAO related "diabatic forcing" (in pair 1) and "diabatic plus eddy forcing" (in pair 2) are examined. In the third pair of experiments, the effects of different background states between P1 and P2 are also taken into consideration. For each experiment, the model is run for only 30 days and the direct response to the NAO-related forcing is seen before baroclinic instability sets in (Jin and Hoskins [1995]). The perturbation response within this time consists of quasi-stationary planetary waves, in a medium of realistic background flow, maintained by the anomalous NAO-related forcing. The configuration of the linear experiments has its advantage that the NAO-related forcing can be linearly split into its dynamic components.

Table 3.1: Setup of linear experiments

	basic state or initial condition	forcing
pair 1	1949-99	diabatic (P1/P2)
pair 2	1949-99	diabatic plus eddy (P1/P2)
pair 3	P1/P2	diabatic plus eddy (P1/P2)

The spinup time for each linear model run is about a week. So, only the average of model output from day 10 through day 16 is the subject of analysis. Figures 3.14a and b show the 7 day mean SLP response to the NAO related model forcing during P1 and P2. To compare the model with the observations, the values plotted have been multiplied by 10 to recover the corresponding values to that of one standard deviation

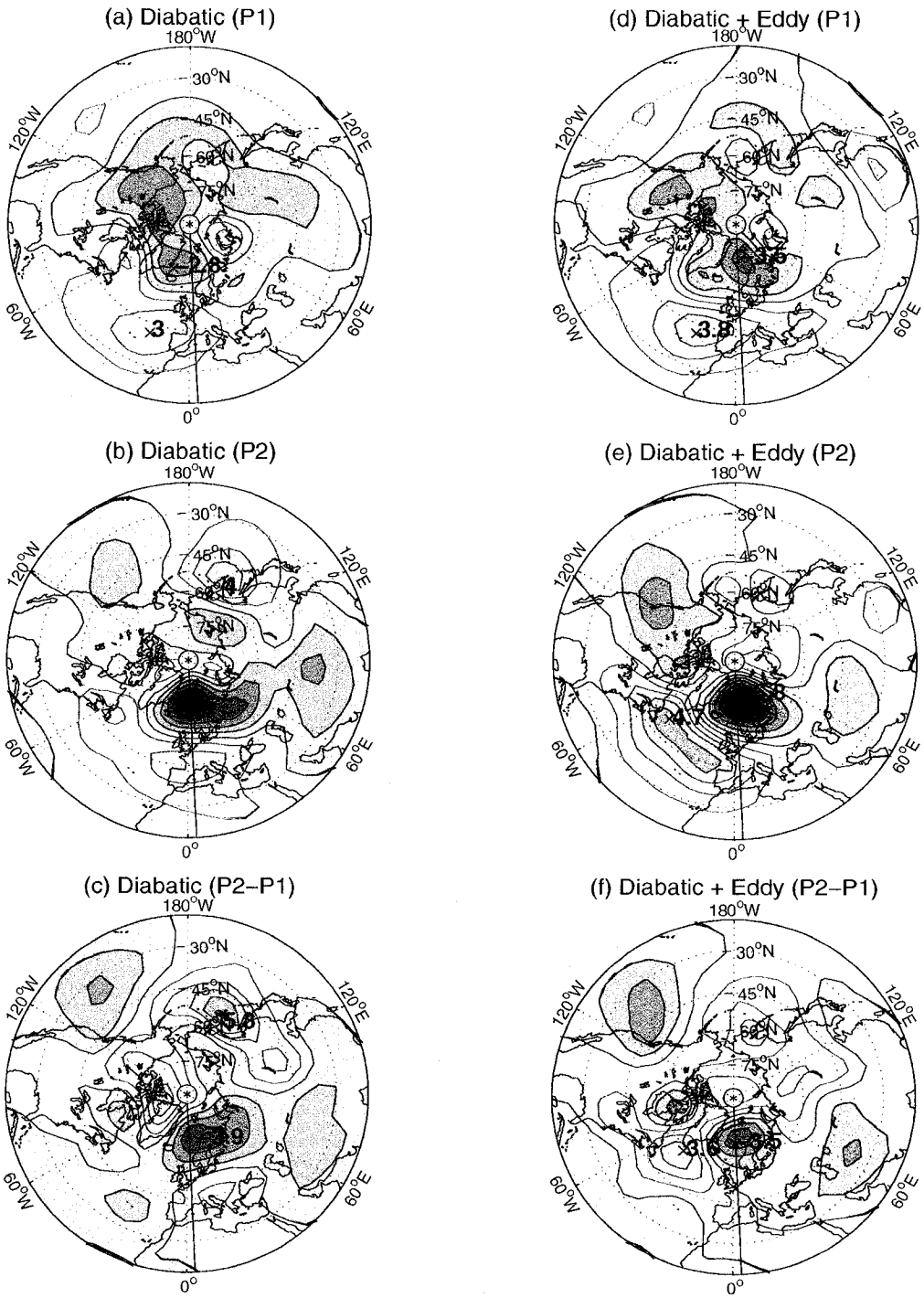

Figure 3.14: (a) and (b) Linear SLP response to the NAO regressed diabatic forcing during P1 and P2, respectively; (d) and (e) Similar to (a) and (b), except using the diabatic plus eddy forcing related to the NAO; (c) SLP difference pattern as a result of (b) minus (a); (f) SLP difference pattern as a result of (e) minus (d). Amplitudes correspond to one standard deviation of the NAO index, and the contour interval is 1hPa.

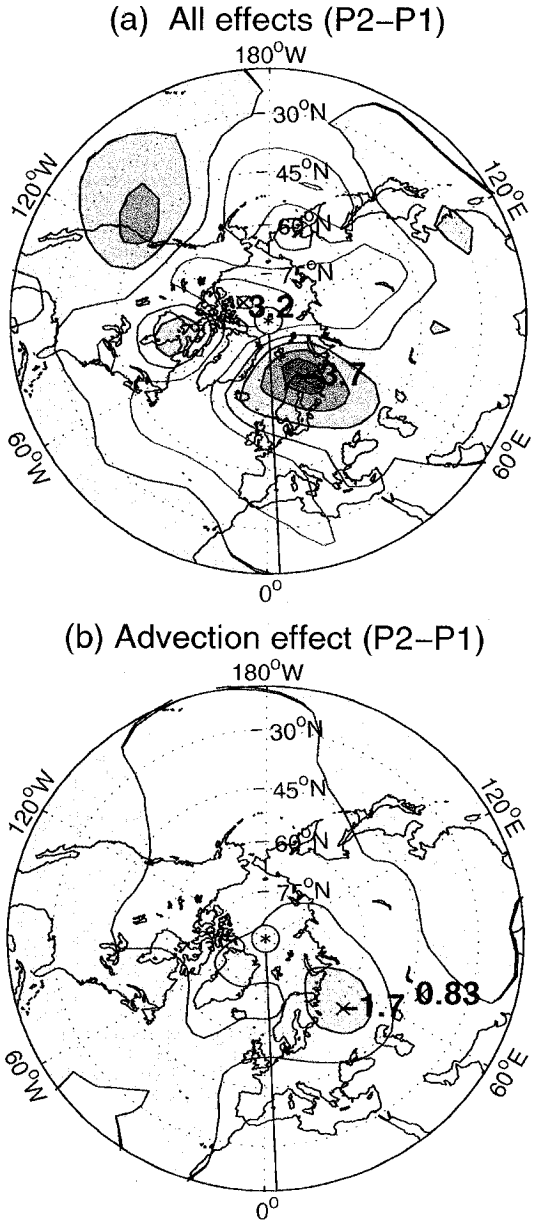

Figure 3.15: (a) SLP difference pattern as a response to the difference in the diabatic plus eddy forcing associated with the NAO between P2 and P1 and the different advection effects due to the different background states during P2 and P1; (b) SLP difference pattern as a result of different advection effects by changed background states. It is obtained by subtracting Figure 3.14f from (a).

of the normalized NAO index. In the Euro-Atlantic sector the dipolar SLP structure of the NAO is substantially reproduced by the model in both periods except some small dubious features near the Kara sea (for P1 case) and near the pole (for P2 case). Even though account has only been taken of the anomalous diabatic forcing, the modeled difference pattern, i.e., subtraction 3.14a from 3.14b, is reminiscent of the observed shift pattern of the NAO, with a low SLP anomaly over Scandinavia and the Barents Sea and with a high anomaly to the west (Figure 3.13c), but more northward displaced than in the observations (Figure 3.9b). The dipolar structure within the zonal range from $20°W$ to $60°E$ hints at a possible connection to the meridional displacement of the North Atlantic storm track between P1 and P2. This serves as a reminder that the diabatic effect of the storm track is an important part of the "diabatic forcing" dubbed here. Adding the eddy forcing to the diabatic forcing improves markedly the performance of the linear model, resulting in more realistic NAO patterns in both periods (see Figure 3.14d and e). In addition, the resemblance of the modeled difference pattern (shown in Figure 3.14f) to the observed shift pattern (see Figure 3.9b) is remarkable in terms of the locations and strength of the Scandinavian low and the high to the west and southwest. As such, the linearized model driven by the "diabatic plus eddy forcing" reproduces reasonably well the eastward shift of the NAO. A third pair of experiments are carried out driven by the NAO regressed forcing for P1 (P2) period, but this time with the model linearized about the P1 (P2) climatology. Now not only the forcing but the sensitivity to the basic climatology is taken into consideration. The great similarity between Figures 3.15a and 3.14f implies that the advection effect of changing background flow from P1 to P2 is not a major contributor to the shift, though it tends to reinforce the deepening of the low over Scandinavia as depicted by Figure 3.15b, the difference between Figures 3.15a and 3.14f.

3.5 Summary and Discussion

We have investigated the nature of the eastward shift of the NAO using a combination of correlation analysis and modelling. The correlation analysis reveals that, after the late 1970's, when an eastward shifted NAO pattern was established, not only the NAO and the ice flux through Fram Strait, but Roger's first NAST mode and Siberian winter temperature are all tied up strongly, suggesting an emergent, spatially coherent climate regime during the last few decades of the 20th century. The monotonic increase throughout the 20th century in the correlation between the indices of Rogers' first storm activity mode and the NAO shown in Figure 3.5c indicates a special role played by the NAST in the NAO shift. The full nonlinear model experiments using the regressed forcing associated with the NAO reveal a SLP pattern with a low over Scandinavia and a high over southern Greenland, which is dubbed "the NAO shift pattern". Its time index shows a quadratic relationship with the strength of the NAO. A corroborative evidence for this relationship has been provided by an independent clustering analysis by Cassou et al. [2003]. This leads reasonably to an explanation for the shift, namely, that the shift is a consequence of the persistent high NAO index during P2 versus persistent low NAO index during P1. As such, to understand the eastward shift of the NAO, we need to understand why the high NAO phase was prevalent during P2 and the low index prevalent during P1, i.e., the upward trend in the NAO index since the 1950's, an issue tackled in the next chapter. What drives the shift is the effect of different nonlinear eddy forcing regulated by the strength of the NAO, while the advection effect by different mean flow between the persistent negative NAO index during P1 and positive index during P2 only plays a secondary role. On the other hand, given the fact that the eddy activity regulated by the strength of the NAO can in turn alter the distribution of the diabatic heating released in the North Atlantic storm track, this then could project differently onto the diabatic forcing pattern associated with the NAO during P1 and P2, a factor not considered in the idealized nonlinear experiments with fixed forcing pattern. To take into account the effect of changing model forcing for the NAO between P1 and P2, linearized

model experiments have been implemented using the forcing regressed against the NAO index during P1 and P2 respectively. The results show that the NAO shift can be partly attributable to the changed "diabatic" forcing; while the eddy forcing, as indicated by the experiments driven by the "diabatic plus eddy forcing", plays an indispensable role in shaping a realistic shift pattern.

In a coupled GCM simulation, Ulbrich and Christoph [1999] found an increase in storm activity over northwest Europe, as well as an upward trend in the model's NAO index and an eastward shift in the model's NAO under increasing greenhouse gas forcing, behavior that was not found in a control run with fixed greenhouse gas forcing. Meanwhile an increase in storm track activity as well as a decrease of mean surface pressure at the downstream tail of the storm track are common features in scenario runs in many different CGCM simulations under increasing greenhouse gas forcing (Carnell et al. [1996]; Hall et al. [1994]; Ulbrich and Christoph [1999]). Since we have documented a link from the eastward shift of the NAO pattern to the upward trend in the NAO index, it is not a surprise to see the NAO shift and the NAO trend concur in Ulbrich and Christoph's scenario run under increasing greenhouse gas forcing. However, the mechanisms that drive the trend of the NAO and hence the NAO shift in reality could be quite different from that in Ulbrich and Christoph's scenario run. For example, in the next chapter the observed upward trend of the NAO index is shown to be related to forcing from tropical Indo-Pacific, but it is not clear if this is also the case in Ulbrich and Christoph [1999]'s model. Further, as documented by Deser et al. [2003], interdecadal transitions have occurred before (such as around 1925, 1947, 1977) in the Indo-Pacific region. The associated variation in the tropical forcing, which is shown in Chapter 4 to be the vital source of the trend observed in the extratropical tropospheric circulation (including the NAO) during the last 50 years, could largely stem from natural climate variablity, although the anthropogenic forcing may also have contributed to the recent transition in the late 1970's. Whether the trend in the NAO index and the shift in the NAO pattern are consequences of the increasing greenhouse gas forcing or naturally arise from the internal climate system

or both is still an open question, pending further investigation.

Chapter 4

Understanding the Trend

This chapter addresses the multidecadal trend in the tropospheric circulation by analyzing its spatial structure and investigating its driving mechanism.

4.1 The trend and the COWL

During the last 50 years or so, the tropospheric circulation underwent a significant change. In particular, in winter time, the trend in NH SLP shows a synchronous deepening trend of the Aleutian low and Icelandic low, as well as a tendency towards lower than normal pressure over Siberia and higher than normal pressure over western North America and western Europe (Figure 4.1a). These features penetrate barotropically up to the mid troposphere and higher, resulting in a similar spatial circulation pattern at the 500 hPa level (Figure 4.1b). The baroclinicity can be expressed by the 500-1000 hPa thickness (Figure 4.1c), which, in some sense follows the spatial structure of 500 hPa height field except for some areas over North Europe, North Africa and East Asia. The 500-1000 hPa thickness is also a good proxy for the lower tropospheric air temperature, whose spatial distribution can well be accounted for by the advection of the climatological temperature by the anomalous tropospheric circulation associated with Figure 4.1a and b. The zonal structure of wave number 3 in the trend of 500-1000 hPa thickness leads to some cancellation of the

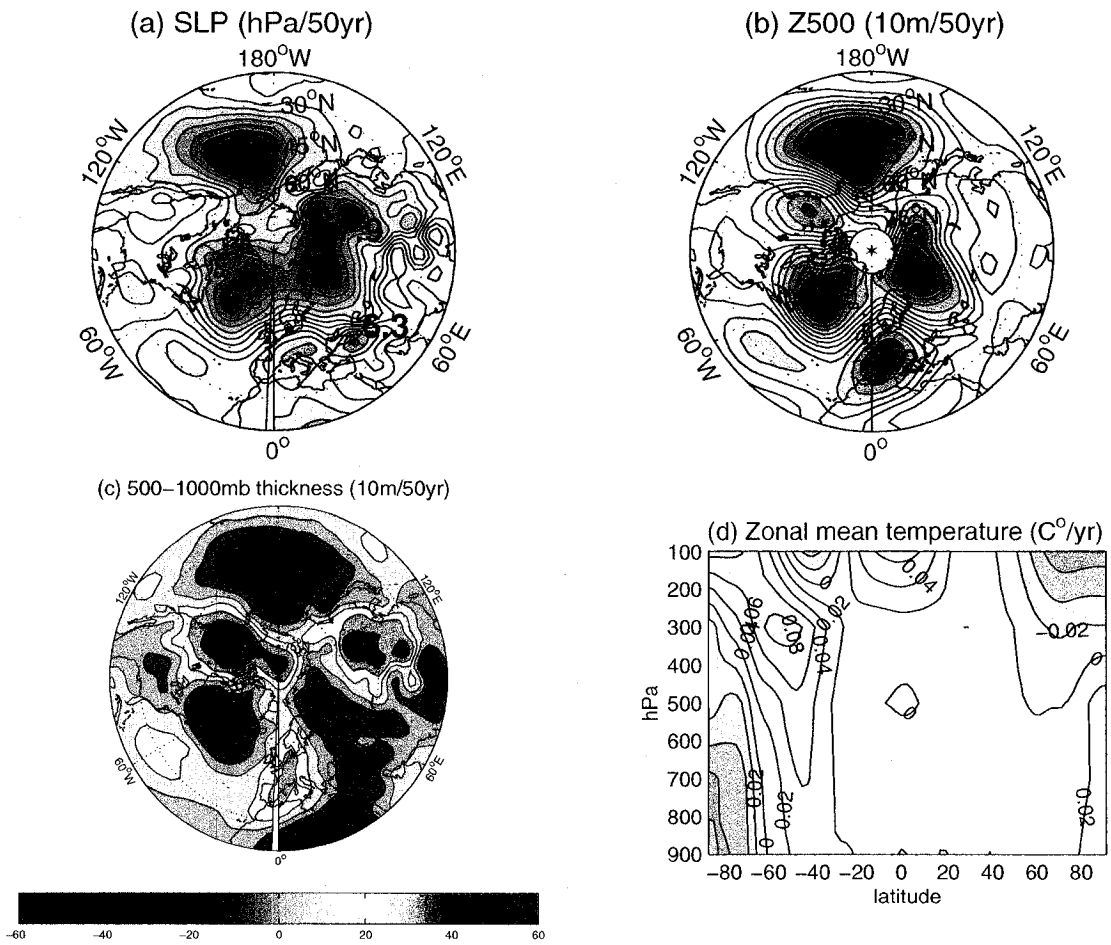

Figure 4.1: The least squares linear trend in (a) SLP; (b) 500 hPa height; (c) 500-1000 hPa thickness and (d) zonal mean air temperature. Using NCAR/NCEP reanalysis data during the 51 winters (DJF) from 1949 to 1999.

temperature trend in the zonal mean (Figure 4.1d). Figure 4.1d nevertheless shows a warming trend in the lower tropical stratosphere and mid-latitudes of the Southern Hemisphere and a cooling trend over the upper troposphere and lower stratosphere (troposphere) near the northern (southern) polar zones. The dataset used for Figure 4.1 is the NCAR/NCEP reanalysis. Considering the fact that much less abundant instrumental data in the Southern Hemisphere are fed into the reanalysis procedure, the temperature trend in the Southern Hemisphere may not be as reliable as that in the Northern Hemisphere. Meanwhile, the temperature data on the upper levels also suffer from instrument change which have affected the temperature trends (Andell [2000]; Gaffen [1994]). In particular, the implementation of satellite data since 1979 in the NCEP reanalysis might introduce some inhomogeneities (or discontinuities) in tropopause temperature between the presatellite and postsatellite periods, thus limiting the usefulness of the data for study of decadal-scale variability over the upper levels near the tropopause (Randel et al. [2000]). For those reasons, only the changes in the Northern Hemisphere troposphere will be the focus of this study.

The 500 hPa geopotential height field is chosen to represent the tropospheric circulation. Here, we examine the tropospheric circulation trend in terms of climate variability modes and try to identify a most representative mode for the trend, which may in turn throw some light on the mechanism of the trend. One of the most important questions concerning the trend is how it is driven. So first, a Singular Value Decomposition (SVD) analysis is applied to the model forcing for the temperature equation (discussed in Chapter 2) over the tropical Indo-Pacific region ($40°S - 40°N$, $60°E - 60°W$) and mean 500 hPa height fields over the northern hemisphere ($20°S - 80°N$) for each of the winters of 1949-99. SVD is a technique that isolates spatial patterns in two fields that tend to occur synchronously with one another and could be physically related to each other by some linear dynamics. (See Bretherton et al. [1992] for the details of SVD techniques and Wallace et al. [1992] for an example of an application to SST and 500 hPa height over Pacific). Choosing the tropical Indo-Pacific as the SVD analysis domain for the diabatic forcing is prompted by the

result of Hoerling et al. [2001a], namely that the changes in tropical SSTs only can drive almost as much of the trend of the winter 500 hPa height field as the global specification of the SST and sea ice. Using the whole tropical band ($40°S - 40°N$) including the tropical Atlantic does not change the results of the SVD analysis.

The first SVD mode explains 50% of the covariance (in terms of squared covariance fraction, SCF, computed as explained in Bretherton et al. [1992]) between these two fields and the correlation between the first pair of expansion coefficients is 0.76. The expansion coefficient for the right (forcing) and left (Z500) vectors are denoted by a(t) and b(t) respectively in Figure 4.2c. A striking feature of b(t) is an upward transition that occurred in the late 70's, indicating a "regime shift" as observed in other climate indices and as discussed in Section 1.1. To gain confidence in the robustness of this SVD mode, a companion EOF analysis is also carried out on both fields separately. The first EOF of diabatic forcing is almost identical to the first right singular vector (Figure 4.2b) and its principal component time series (PC) is significantly correlated (r=0.52, at 1% confidence level) with the PC of the second EOF of Z500 field, which itself is spatially correlated with the pattern of the Z500 trend at as high as 0.81 (and correlated with the left vector at 0.85). The great similarity between the first SVD left vector (Figure 4.2a) and the observed trend in 500 hPa height (Figure 4.1b) suggests that the SVD analysis picks out the tropical diabatic forcing that is related to the trend. This diabatic forcing mode has high loadings over the central equatorial Pacific, western subtropical Pacific and the northwest of Australia (Figure 4.2b), and these regions will be the focus of examination for driving the trend. Given the fact that the tropical diabatic forcing is dominated by the latent heat release associated with convective precipitation, the diabatic forcing pattern revealed by the first SVD is probably dominated by the precipitation anomalies associated with the tropical SST anomalies shown in Figure 4.2d. This latter figure is derived by regressing the winter mean SST for each of the 51 winters against the time series of b(t). Indeed, the diabatic forcing field shown in Figure 4.2b does share some common features with the precipitation trend in Figure 4 of Hoerling et al. [2001a], which is driven by the

specified time series of tropical SST.

The second SVD mode explains 20% of SCF between the two fields and the second left singular vector (for the Z500 field) bears great resemblance to the AO pattern on 500 hPa height. However, no similar link is found between the 500 hPa version of the AO, i.e, the leading EOF of 500 hPa height, and any EOF mode of the tropical diabatic forcing. Therefore, no further effort is made toward understanding the second SVD mode.

Besides the close relationship to the trend and the second EOF of Z500 field, the first SVD mode also has an intimate connection to the circulation pattern associated with the PC of the first EOF of northern hemisphere storm activity (NHST1) obtained by Chang and Fu [2002]. This can be seen by comparing Figure 4.2a with the 500 hPa pattern shown in Figure 1.5b (Section 1.2). Like the time series b(t) associated with the first SVD mode, the first PC time series of Chang and Fu (2002) shows an upward transition during the period of 1970's, and is associated with an increase in storm activity over both the North Atlantic and North Pacific basins. All these patterns mentioned here share a common feature with the "COWL" pattern (Figure 1.5a, Section 1.2), i.e., congruent deepening of Aleutian and Icelandic lows. To put things in perspective, all the Z500 patterns of climate variability modes including the trend, AO, COWL, NHST1, AL-IL seasaw (as introduced in Section 1.2, see Figure 1.5c) and the left vectors of the leading two SVD's, after area weighting, are projected onto the first two EOF's of the northern hemisphere ($20°S - 80°N$) winter mean Z500 fields. All the patterns have been normalized by the area-weighted standard deviation of their spatial variance on the grid used for the analysis (2.5° in latitude by 5° in longitude). The results are shown in Figure 4.3. The leading two EOF's, consistent with others (Kimoto and Ghil [1993]; Corti et al. [1999]), are Z500 versions of the AO (EOF1) and PNA (EOF2). Each pattern is plotted as a colored line with its end point defined by the projection coefficients of the pattern on both EOF's. The length of the line represents the extent to which the pattern can be expressed by the leading two EOF's and the angle from the axes indicates the relative spatial similarity of the

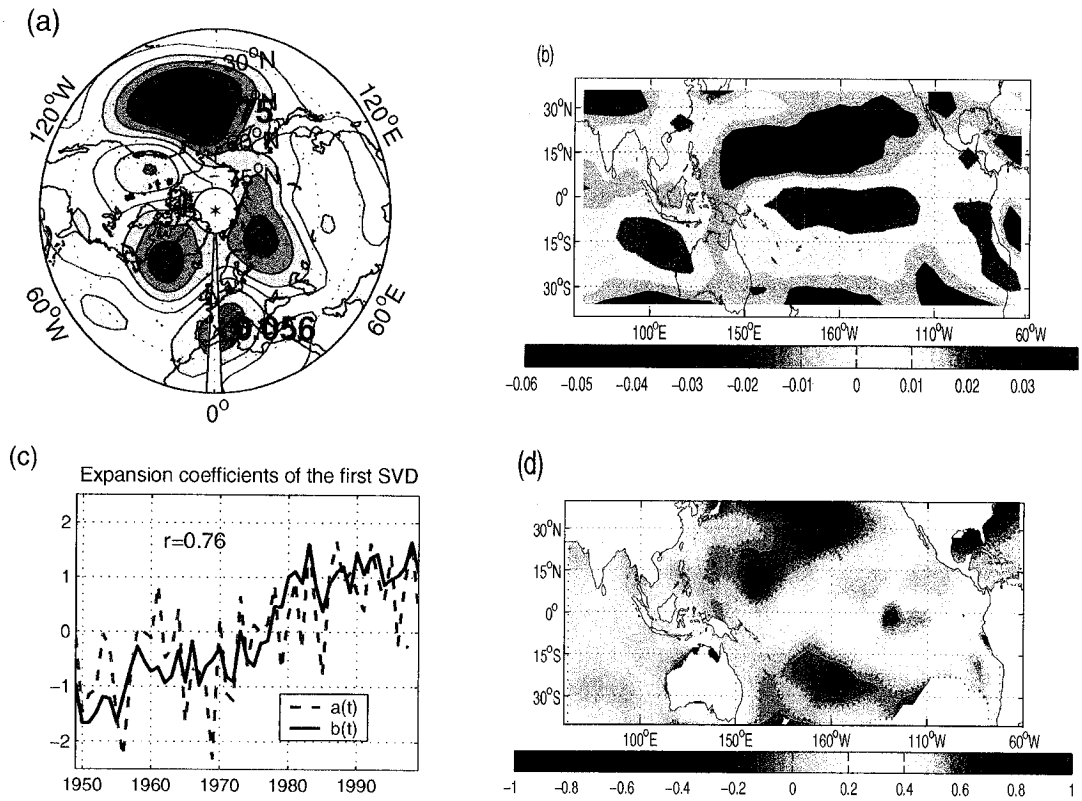

Figure 4.2: (a) and (b) show the first pair of vectors from the SVD analysis on northern hemisphere 500 hPa height and tropical Indo-Pacific ($40°S-40°N$, $60°E-60°W$) forcing for the temperature equation of the Hall model. (a) is the normalized pattern of the left vector for 500 hPa height and (b) is the right vector for tropical forcing (vertically integrated). The contours have no units and only the spatial pattern matters; (c) shows the expansion coefficients for the first SVD. a(t) is for 500 hPa height and b(t) for the tropical forcing; (d) is the regression of winter mean SST against time series b(t). The unit in the color bar is °C.

pattern to the EOF's. The patterns associated with a tropical diabatic source (SVD1, magenta), northern hemisphere storm track variability (NHST1 mode, green) and the land-ocean thermal contrast (COWL, cyan) all cluster around the EOF2 ordinate with the trend pattern (red), indicating their common linkage to the recent climate change. Indeed, all these patterns are significantly spatially correlated with each other. The spatial correlation coefficients among them are summarized in Table 4.1. Given the 1800 grid points for each pattern, the correlations shown in the table are all significantly different from zero. Thus, this group of patterns can be categorized as "COWL-like". Among these, the trend pattern is almost identical to the SVD1 pattern and the COWL pattern is almost identical to the EOF2 pattern. In the subspace, the 500 hPa patterns of the leading two SVD's coincidentally parallel to the leading two EOF's, but with the order of modes reversed in SVD's due to the selection of a COWL-like pattern by the tropical diabatic forcing. Note that the COWL-like pattern is a PNA teleconnection wave train over the North Pacific and neighboring continents, except having an NAO-like tail trailing off over the North Atlantic region.

Table 4.1: Spatial correlations between the COWL-like patterns

	Trend	COWL	NHST1	SVD1	EOF2
Trend	1	0.70	0.89	0.98	0.81
COWL		1	0.78	0.78	0.94
NHST1			1	0.88	0.85
SVD1				1	0.85
EOF2					1

Shown in blue in Figure 4.3 is the projection of the AO on the first two EOF's of 500 hPa height. Note that the AO index is defined as the first PC time series associated with an EOF analysis of winter mean SLP, following Thompson and Wallace [2000a], and that the AO pattern used here is obtained by regression of winter mean 500 hPa height against the AO index. We see that the AO lies in the middle of the

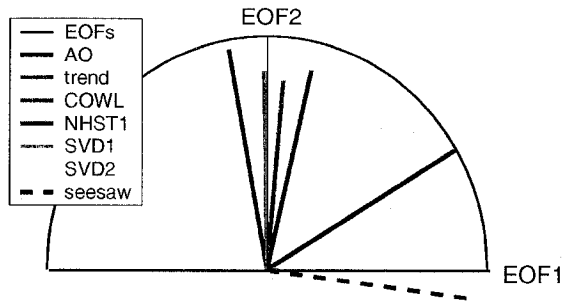

Figure 4.3: Projection of 500 hPa height patterns in the subspace spanned by the leading two EOF's. The end point of each colored line is defined by the projection coefficients on the EOF's.

first quadrant biasing somewhat towards the EOF1 axis with the length of the projection close to unity, indicating that the AO variability can be largely accounted for by the leading two EOF's. The large angular difference of the AO from the "COWL-like" group indicates the limitation of the AO in portraying the climate change during the last 50 years or so. The dashed blue line represents the Z500 pattern of AL-IL seasaw, which lies beside the axis of EOF1 and almost orthogonal to the pattern of the trend in the subspace of the EOF's. From Figure 4.3, an argument can be made that the "COWL-like" modes more closely represent recent climate change than the AO and AL-IL seasaw (see also Corti et al. [1999]). As will be unraveled by the upcoming model experiments, the forcing mechanisms for the COWL and AO are characteristically different too.

4.2 Ensemble experiments for each winter from 1949-1999

In this section, three sets of ensemble experiments are conducted to investigate the forcing source for the trend in the tropospheric circulation as well as the variability of the AO and NAO.

The experimental procedure is the same as in Peterson et al. [2002]. For each set of experiments, an ensemble of 30 model runs is carried out using the time-independent proxy diabatic forcing computed for each winter from 1949-1999 as described in Chapter 2. The ensemble members differ only in the choice of initial condition, these being chosen randomly from the 4550 winter daily mean realizations in the NCAR/NCEP reanalysis. Each ensemble member is integrated for 4 months and the analysis is carried out on the final 3 months. For the first set of ensemble experiments, the forcing for each winter is specified globally to drive the Hall model. We begin by examining the AO and the linear trend in the ensemble mean model results. Figure 4.4a shows the ensemble mean AO index in the model (red line) as well as the observed AO index as derived from the NCAR/NCEP reanalysis (green line). The AO index, whether from the model output or the reanalysis, is calculated as the projection of the winter (DJF) mean SLP on the first EOF of the winter mean SLP from the NCAR/NCEP reanalysis, and normalized by the standard deviation of the observed PC of this mode, as in Lin et al. [2002]. The model ensemble mean captures the interannual variability of the AO with a correlation with the observed index of 0.66 (significant at the 1% confidence level). The upward trend of the AO index is also captured, although the trend in the model is somewhat overestimated compared with that in the data.

The least-squares linear trend in ensemble mean 500 hPa height is plotted in Figure 4.5b and compared with the observed trend (Figure 4.5a). The model is able to reproduce the observed trend reasonably well (the spatial correlation between the modeled and observed trend is 0.59), with the exception that the deepening trend of the Aleutian low seen in the observations is missed by the model, an issue we will revisit later when discussing results from the linearized model. The missing North Pacific center serves as an explanation for the overestimation of the AO trend in the model: the North Pacific low center in the observed trend projects negatively on to the AO pattern because of the high geopotential height anomaly associated with the positive AO pattern over the North Pacific. Since the deepening of the Aleutian low is missing in the modeled trend, this effect is to increase the projection of the modeled

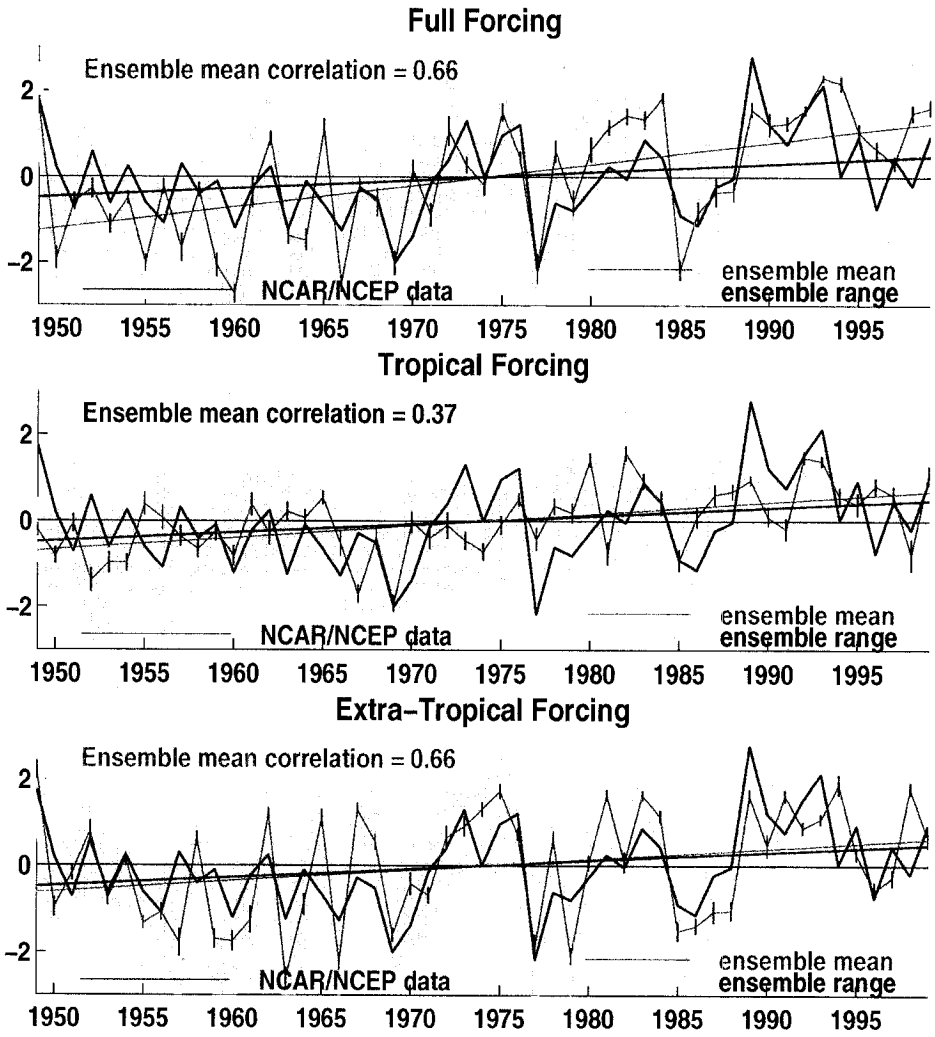

Figure 4.4: Time series of the AO index for three different forcing scenarios. The green line is the observed AO index computed from the NCAR/NCEP data, and the red line is the AO index computed from the ensemble mean SLP field exactly as in Lin et al. [2002]. The shading indicates the spread in the individual ensemble members. The straight lines indicate the trend. Also shown are the correlation between the AO index computed from the ensemble mean SLP and the observed AO index.

trend on to the AO pattern, and hence to spuriously enhance the upward trend of the AO in the model.

As aforementioned, Hoerling et al. [2001a] found that the evolution of tropical SST is influential on the low frequency trend of the extratropical atmospheric circulation. In an effort to address the relative importance of tropical and extratropical forcing, two additional sets of model experiments were conducted. In these experiments, we force the model using the derived forcing for each winter only in the tropics ($36°S \leq y \leq 36°N$) or only in the extratropics ($y \geq 36°N$, and, $y \leq 36°S$), with the climatological forcing (averaged over the 51 years) applied elsewhere, as described in Appendix A and Greatbatch et al. [2003]. The AO index from these two sets of experiments is shown in Figures 4.4b and c respectively. For the tropical forcing case, the correlation with the observed AO index is 0.37, and after removing the trend, the correlation reduces to only 0.28. By contrast, the AO signal driven by the extratropical forcing accounts for almost as much as variance (44%) as the global forcing case, indicating the dominance of extratropical over tropical forcing for influencing the interannual variability of the AO. As to the trend of the AO, denoted by the straight red lines in Figure 4.4, it seems that both the tropical and extratropical forcing are equally important contributors to the trend of the AO in the model. But caution should be used for this interpretation considering the model's deficiency in capturing the trend over the North Pacific.

Seeing that the model shows skill in the North Atlantic sector, we analyzed the regional representation of the AO, i.e., the NAO, by calculating the NAO index based on the two point pressure difference between Iceland and Lisbon, following Hurrell [1995b]. The NAO index for the three sets of experiments, as well as from NCAR/NCEP reanalysis is plotted in Figure 4.6. It is noted that the model performs better in capturing the interannual variability and the trend of the NAO than for the AO. The correlation between the NAO index in the ensemble mean and the observed NAO index is 0.8 and 0.78 for the global forcing and extratropical forcing cases, respectively. Similar to the case of the AO, an argument also holds for the

NAO that the modeled NAO variability mostly stems from the extratropical forcing. Notwithstanding this, the trend of the NAO is mostly driven by the tropical forcing, in agreement with Hoerling et al. [2001a]. Indeed, the trend in 500 hPa height field driven by the tropical forcing (Figure 4.5c, its spatial correlation with the Figure 4.5a is 0.54) shows a strong projection on the NAO or the AO in the Euro-Atlantic region and a strong similarity to the observed trend everywhere except over the North Pacific, again, suggesting the importance of tropical forcing for the trend. The trend due to extra-tropical forcing (Figure 4.5d, its spatial correlation with Figure 4.5a is 0.12) bears an annular feature but with its node line farther to the north compared to the AO and thus moderately projecting on to the AO. In the North Atlantic region, the dipole structure apparent in the extratropical forcing case is so tightened up to the high latitudes that the NAO index picked up from Figure 4.5d is rather small. However, the different projection upon the AO and the NAO by the extratropically driven trend may not lead to differentiating the AO from the NAO, given the model's deficiency in capturing the change in the North Pacific. This deficiency is likely the result of the misrepresentation of eddy activity by the model nonlinearity (as will be shown in Section 4.3.2). In order to compensate for this deficiency, in the next section we put the question in a linear framework, wherein the direct effect of model forcing can be unscrambled from the nonlinear dynamics in the full model.

4.3 Regressed forcing experiments

In an attempt to bypass the deficiency of the nonlinear model described in the previous section, namely that the model-generated internal eddy activity could operate differently from the real world over the North Pacific, in the first part of this section, we take a linear approach using a version of the model linearized about the observed climatologically-averaged state for the 51 winters. In addition, it is worthwhile to investigate the linear dynamics of the trend in its own right.

To elaborate on this approach, at first a forcing (containing both "diabatic" and

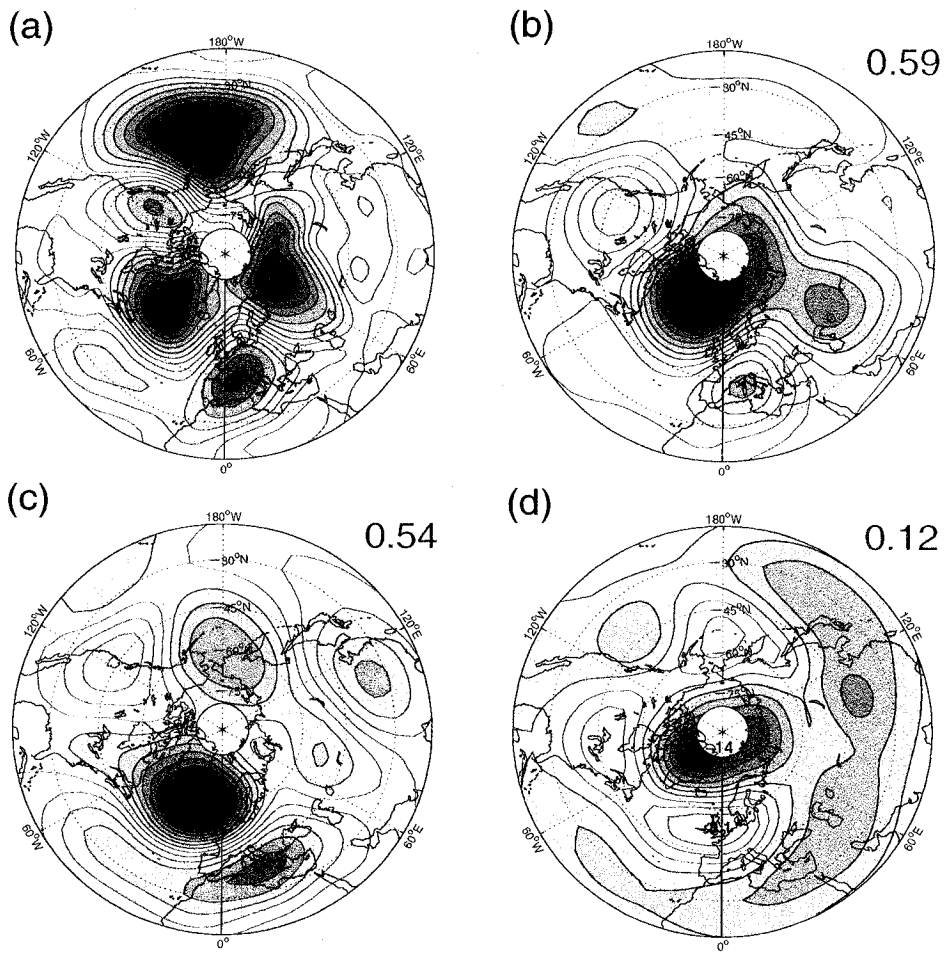

Figure 4.5: (a) The observed linear trend of 500 hPa height during winters from 1949-1999; (b), (c) and (d) show the linear trend of model ensemble mean 500 hPa height when the model is driven by global, tropical and extratropical forcing, respectively. C.I.=2m/10yr. The number in the upper right corner refers to the spatial correlation between the patterns of the modeled and observed trend.

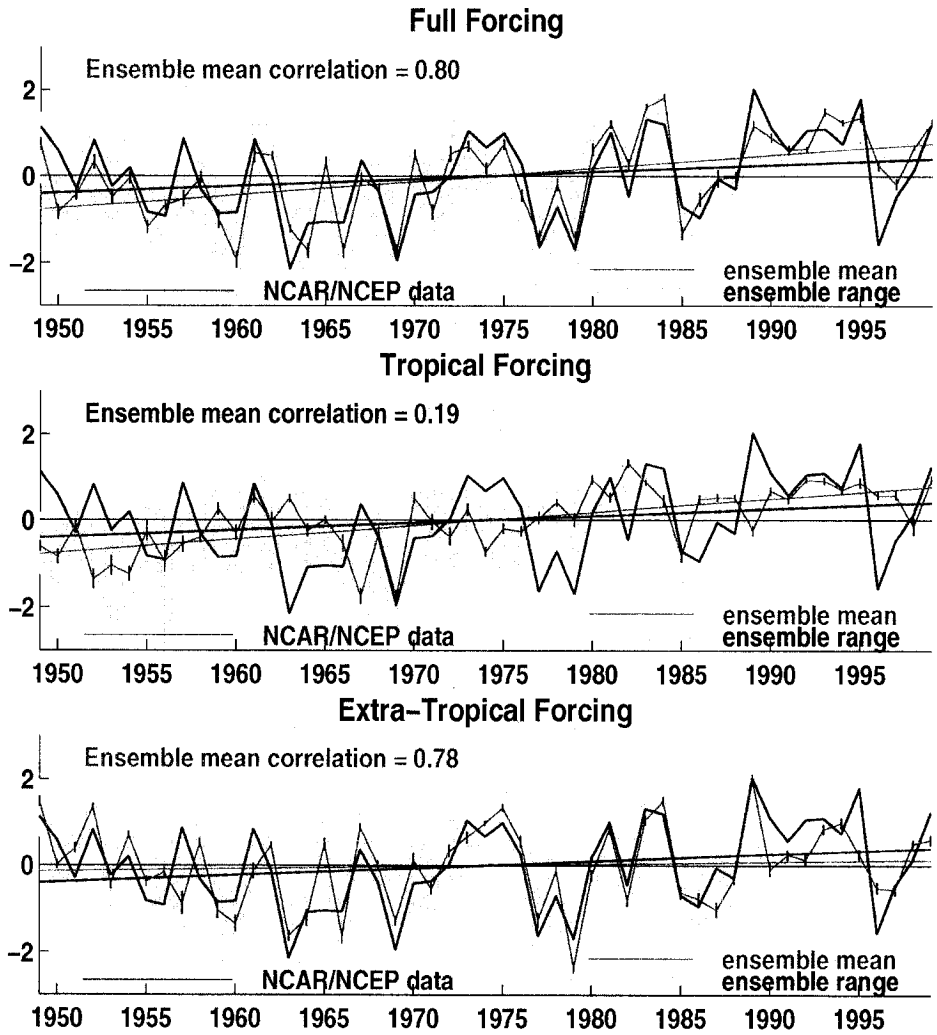

Figure 4.6: Time series of the NAO index for three different forcing scenarios. The green line is the observed NAO index computed from the NCAR/NCEP data, and the red line is the NAO index computed from the ensemble mean SLP field produced by the model. In each case, the NAO index is exactly computed as Peterson et al. [2002]. The shading indicates the spread in the individual ensemble members. The straight lines indicate the trend. Also shown are the correlations between the NAO index computed from the ensemble mean SLP and the observed NAO index.

"eddy" effects) is calculated from equation (2.8) with the initial condition set to be the climatology of the 51 winters. When run with this forcing, the model will remain at the climatological state, which is also the state about which the model is linearized, unless either additional anomalous forcing is added or the climatological state is unstable to small perturbations. Next, a forcing for the SVD1 or AO is obtained by regressing the model forcing computed for each winter against the time series b(t) in Figure 4.2c or the AO index, respectively. The regressed forcing, as a perturbation forcing is then added to the climatological forcing after being weighted by 0.1. This small weighting will keep the perturbative part of the response small and delays the triggering of baroclinic instability. Each experiment is run for only 30 days and the direct response to the regressed forcing is seen before baroclinic instability eventually sets in (Jin and Hoskins [1995]). Exactly the same strategy has been implemented in Section 3.4 to investigate the eastward shift of the NAO.

As before, three sets of linear experiments were carried out by specifying the regressed forcing over the globe, the tropics ($36°S \leq y \leq 36°N$) and the extra-tropics ($y > 36°N$, and, $y < 36°S$) for the SVD1 and AO respectively. The 500 hPa response averaged from day 10 to 16 is summarized in Figure 4.7. The actual response to the weighted regressed forcing has been multiplied by a factor of 10 (so that the forcing is scaled up to the realistic magnitude corresponding to one standard deviation of the respective regression time series) in order to compare with the observations.

4.3.1 Results for the AO

As to the relative importance of tropical and extratropical forcing for the AO in the linearized model, the right column of Figure 4.7 clearly indicates that the AO is predominantly driven by the extratropical diabatic forcing, while the tropical forcing only plays a minor role. It is of particular interest that in the extratropical and global forcing cases, the linear response to the regressed AO forcing shows a deepening of the Icelandic low with high pressure anomalies to the south. The increasing baroclinicity

[1] due to the changing vertical wind shear over the North Atlantic (Figure 4.8a) tends to enhance the North Atlantic storm track which in turn should feed back on the linear stationary response. Thus, it may be argued that the diabatic forcing associated with the North Atlantic storm track orchestrates the interaction between the mean flow and eddy flux and hence controls the variability of the AO. The same argument has been invoked to interpret the existence of the climatological storm track (Hoskins and Valdes [1990]). If the global AO-regressed forcing is applied to drive the full nonlinear Hall model, the nonlinear response (Figures 4.8c and d) captures more features of the observed AO pattern on 500 hPa height (Figure 4.8b) than the linear cases (Figures 4.7 b and f) and shows quite an amount of linear dependence on the sign and strength of the AO-regressed diabatic forcing. This result underscores the importance of the feedback from eddy activity associated with the storm track in shaping a more realistic AO response to the specified AO-related model forcing and indicates a somewhat linear dependence of transient eddy forcing on this AO-related model forcing.

Despite the fact the AO is not driven directly by the tropics on interannual time scales, we have seen that the tropically-driven trend in the nonlinear model (Figure 4.5c) does project on the AO/NAO. This implies that different mechanisms are responsible for exciting the AO on interannual time scales compared to the trend.

4.3.2 Results for SVD1

The response to the SVD1 related forcing is displayed in the left column of Figure 4.7. These panels should be directly compared to the regression pattern of 500 hPa height field against the SVD1 expansion time series b(t), which is not shown because it is almost identical to the trend pattern (Figure 4.5a) if the latter is multiplied by a factor of 1.5. Alternatively, to directly compare with the amplitude of the

[1] measured by maximum Eady growth rate $\sigma_{BI} = 0.31 \cdot f \cdot |\frac{\partial \mathbf{v}}{\partial z}| N^{-1}$, where f is the Coriolis parameter, $\mathbf{v}$ is the horizontal wind, and $N = [(g/\theta)(\frac{\partial \theta}{\partial z})]^{1/2}$ is the Brunt-Väisällä frequency with the potential temperature θ. The growth rate here is computed on the 500-300 hPa level and $0.01 s^{-1}$ is used as an approximation for N on this level.

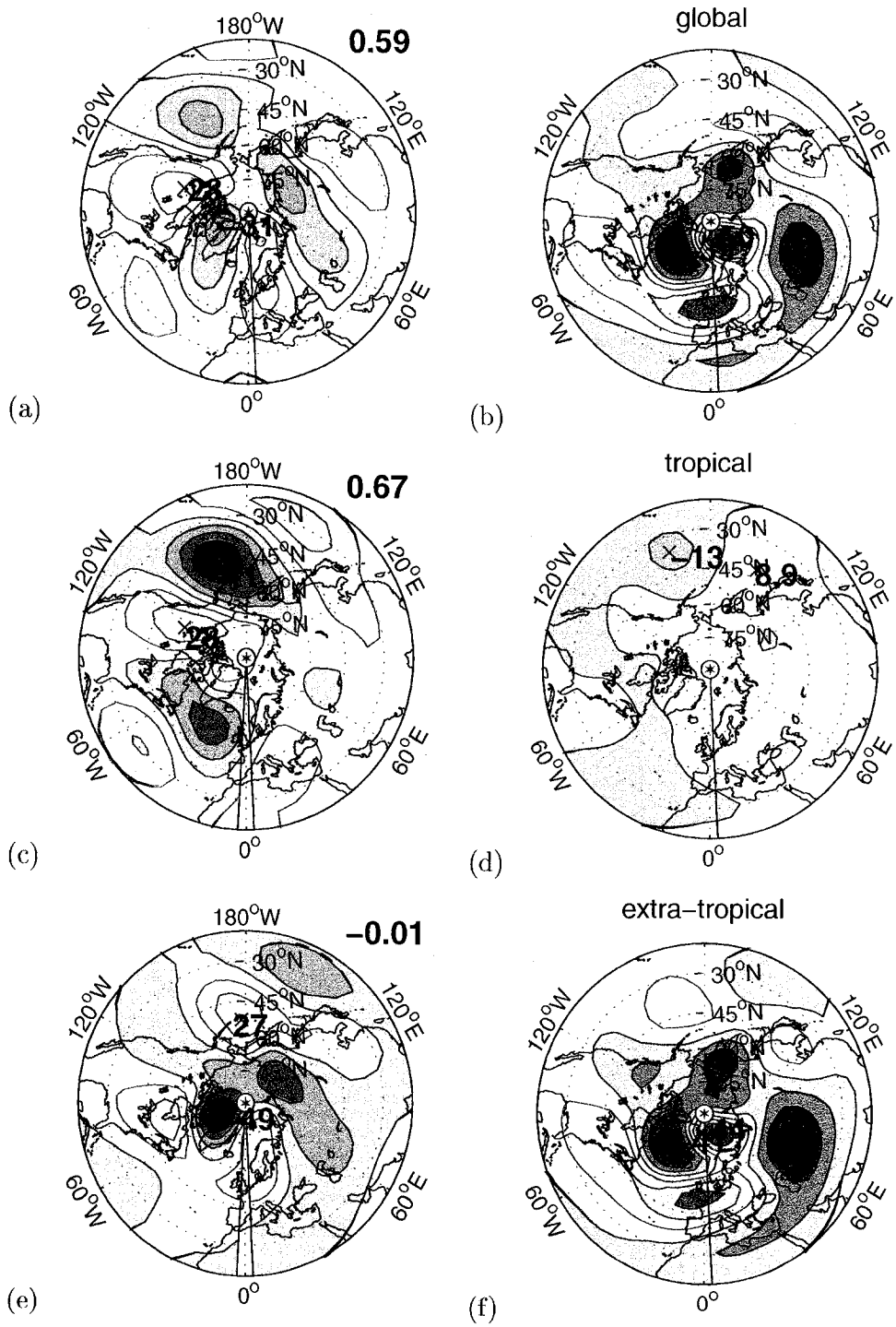

Figure 4.7: Left column: linear Z500 response to SVD1 regressed forcing. The number in the upper right corner refers to the spatial correlation with the pattern of the observed trend shown in Figure 4.5a; right column: linear Z500 response to AO regressed forcing. C.I.=10 m/std of index; top: the forcing is specified globally; middle: tropically; bottom: extratropically.

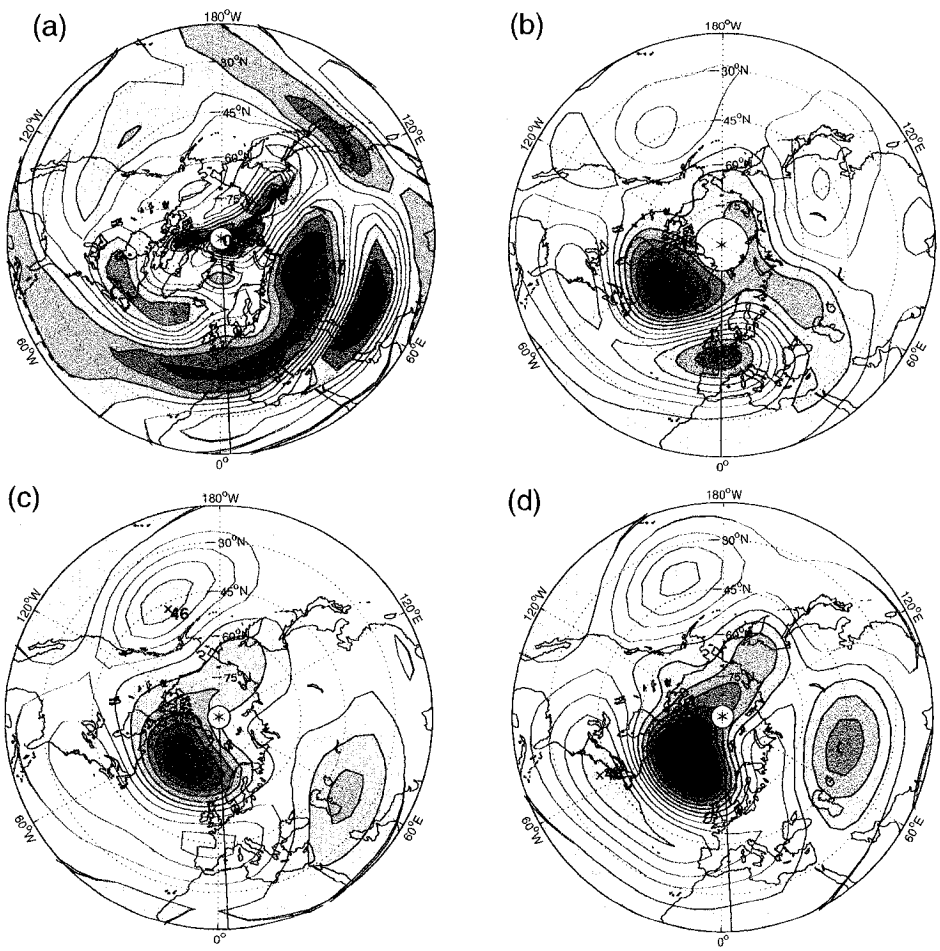

Figure 4.8: (a) Changes in the maximum Eady growth rate σ_{BI} on the 500-300 hPa level in a linear experiment driven by the global AO regressed forcing. C.I.=0.01 day^{-1}; (b) The regression of the NCAR/NCEP 500 hPa height against the observed AO index. The amplitude corresponds to one standard deviation of the AO index; (c) and (d) are the response of 500 hPa height in the nonlinear model to the AO regressed forcing with an amplitude of ± 1 standard deviation, respectively. Note that, for the purpose of comparison, the actual model response to the minus forcing has been reversed in (d). C.I.=10m/1 std of AO index in (b), (c) and (d).

observed trend (Figure 4.5a), the linear results shown in the left column of Figure 4.7 should be divided by 1.5. It is seen that the linear model can reasonably capture the amplitude as well as the spatial pattern of the observed trend. In contrast to the trend simulated in the ensemble experiments from 1949-1999, the deepening of the Aleutian low is reasonably well captured by the global SVD1 forcing applied to the linear model (the spatial correlation between Figures 4.7a and 4.5a is 0.59). Perhaps the most remarkable deficiency of the linear model is the exaggeration of the positive height anomaly extending from Northern Europe northward to the Barents Sea, although this tendency is present in both the observations and the nonlinear model as evidenced by the positive anomaly in Figures 4.5a,b over western Europe. This deficiency of the linear model suggests the importance in reality of nonlinear interaction between the diabatic forcing and the eddies over the Euro-Atlantic sector. On the other hand, the fact that the linear model does better over the middle latitudes of the North Pacific than the nonlinear model suggests that the trend over this area is more directly accounted by linear dynamics. Collectively, the relatively better (worse) performance of the full nonlinear model over the North Atlantic (Pacific) sector versus the relatively better (worse) performance of the linearized model over the North Pacific (Atlantic) sector implies different roles of the modeled nonlinear eddy dynamics in explaining the trend over the two sectors.

When only the tropical portion of the SVD1 related forcing is superimposed upon the climatological forcing to drive the model (Figure 4.7c), we immediately see the importance of a hemispheric wave train which emanates from the central and western tropical Pacific and ends over the North Atlantic and Western Europe. The particular arrangement of the highs and lows gives rise to a strong projection on to the observed trend pattern (the spatial correlation to the observed trend pattern is 0.67). The remarkable similarity of the tropical-driven pattern (Figure 4.7c) to the observed trend (Figure 4.5a) corroborates the notion of Hoerling et al. [2001a] that the trend in the NH tropospheric circulation during the past half century originated from the tropics. This tropical root can be further elucidated by comparing Figure 4.7c with

the tropically-forced case shown in Figure 4.5c. In Figure 4.5c, a standing wave train reminiscent of its linear counterpart is discernible over eastern Asia, the North Pacific and North America, but with the North Pacific lobe much damped and shifted poleward. Downstream over the North Atlantic sector, a pronounced dipole is fully developed and shaped like the NAO in the nonlinear model. These differences from the linear result are most likely due to the local effects of the model-generated eddies, which tend to reinforce (damp) the original signal of the wave train over the North Atlantic (North Pacific). In addition, the extratropical forcing local to the Pacific wave train also tends to counteract the wave train, as can be seen from the linear response to the extra-tropical SVD1 related forcing (Figure 4.7e, its spatial correlation to Figure 4.5a is -0.01), wherein, the wave pattern over the Pacific sector is out of phase with that of the tropical forcing case, suggesting that the extratropical forcing is orchestrated, at least in the North Pacific sector, by the tropically forced signal, but acts to reduce the magnitude of the tropical signal. By factoring the possible reasons for the trend into tropical diabatic forcing, local eddy forcing and local diabatic forcing, we have shown that for the trend towards a low pressure in the North Pacific, the only source is from the tropical diabatic forcing. The trend in the North Atlantic is also tropically seeded, but in this sector the eddy forcing associated with the North Atlantic storm track positively feeds back on the original wave signal resulting in a resonant dipole over the North Atlantic.

This argument is further confirmed by another two ensembles of supplementary nonlinear experiments, in which the nonlinear response to the tropical diabatic forcing associated with the SVD1 is investigated. Figures 4.9a and b show the ensemble mean 500 hPa response of the nonlinear model to the regressed forcing associated with SVD1 with an amplitude of minus one standard deviation and plus one standard deviation, corresponding roughly to years 1962 and 1980 respectively in Figure 4.2c. For the purpose of comparison with Figure 4.7c, the model response in Figure 4.9a has been multiplied by -1. For the same reason, all the plots shown hereafter for the response to minus one standard deviation SVD1 forcing are of opposite sign to

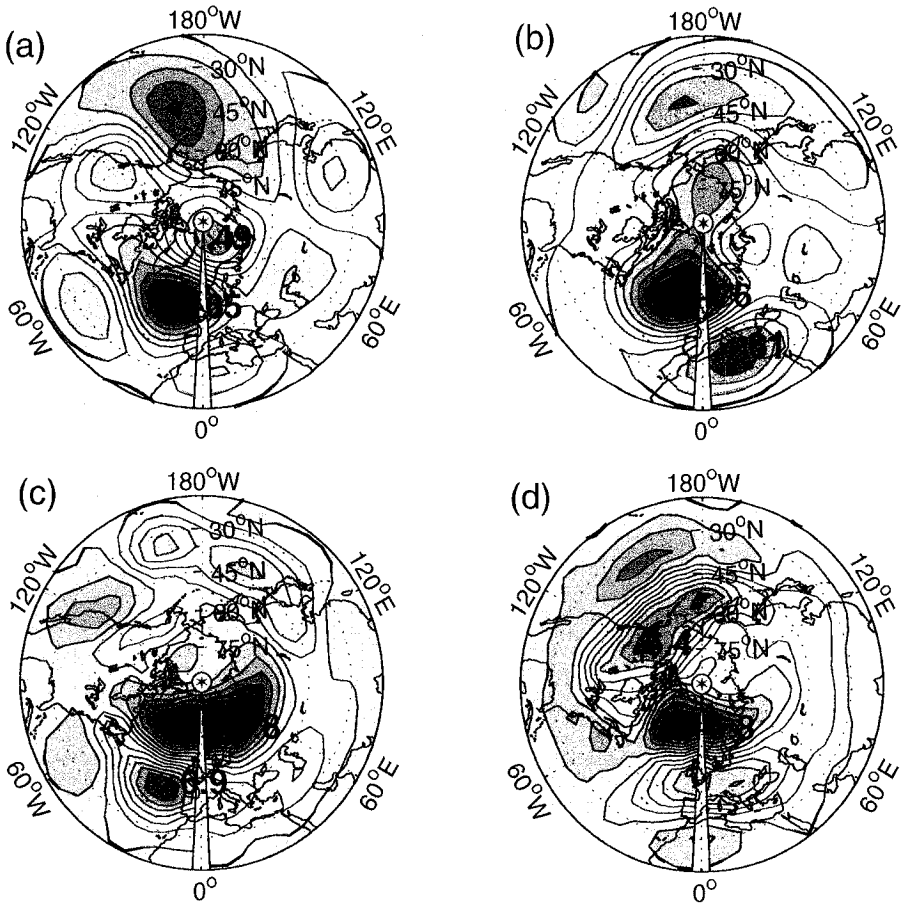

Figure 4.9: (a) and (b) are the response of 500 hPa height in the nonlinear model driven by SVD1 tropical forcing with an amplitude of minus and plus one standard deviation, respectively; (c) and (d) are the same as (a) and (b) except that they show the change in the 500 hPa storm track (in terms of root-mean-square high-pass filtered 500 hPa height) in response to the imposed forcing. Note that (a) and (c) show the model response multiplied by -1. C.I.=10m/1 std of index for 500 hPa height field and C.I.=m/1 std of index for 500 hPa storm track.

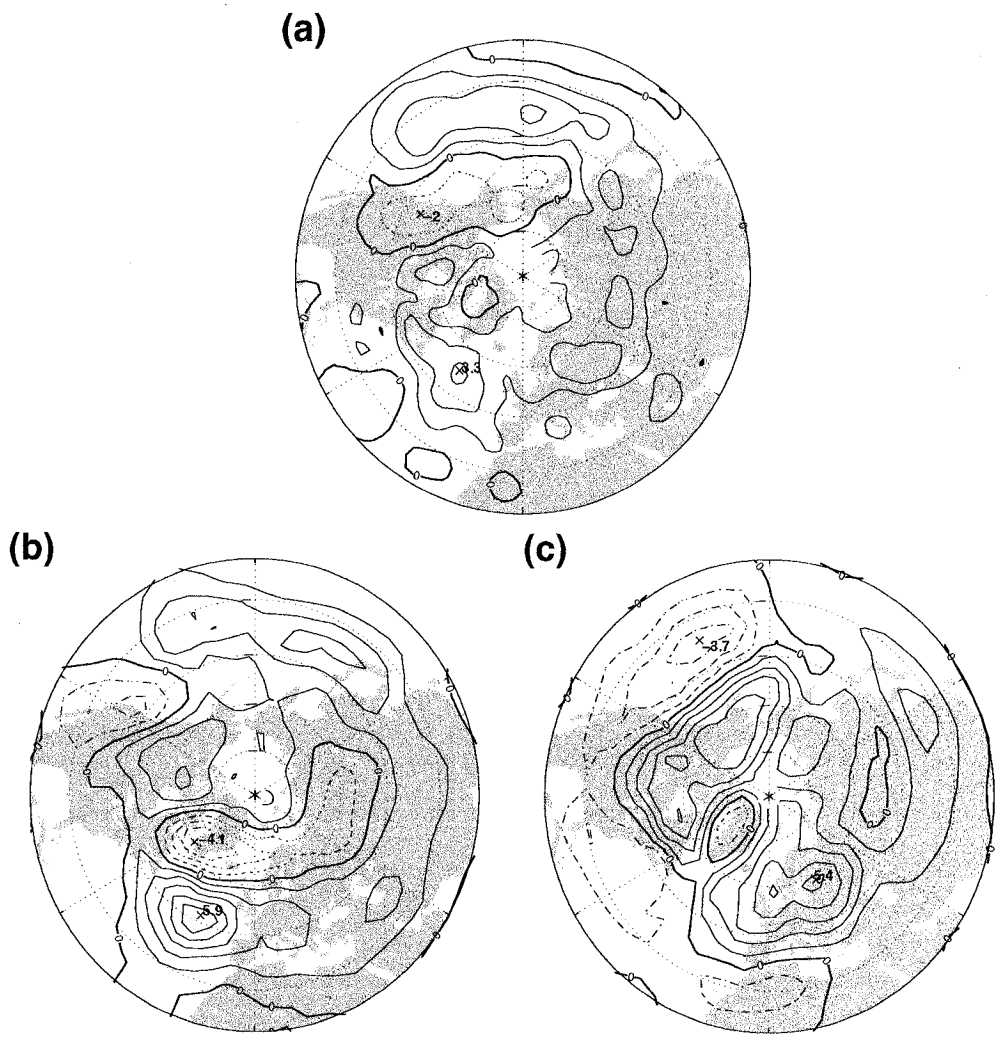

Figure 4.10: (a) the regression of the observed root-mean-square high-pass filtered 500 hPa height variability against the time series of b(t); (b) and (c) are the same as Figs. 4.9(c) and (d) except for global SVD1 forcing, respectively. C.I.=m/1 std of index.

the actual model response, and will be referred to as the "minus response" (and likewise, the "plus response" for plus one standard deviation SVD1 forcing). We can see that the "minus response" in Figure 4.9a is quite similar to that of the linear model (Figure 4.7c), whereas there is a marked difference over the North Pacific in the "plus response" in Figure 4.9b, indicating a strong departure from linearity over the North Pacific. By contrast, over the North Atlantic, the effect of nonlinearity is to enhance the linear response in both cases. This is consistent with our previous findings, namely that the model's nonlinearity acts to weaken (or even reverse) the model's linear response to tropical forcing over the North Pacific, but enhance the linear response over the North Atlantic. This behavior of the nonlinear model can be related to the change in the model storm tracks (represented by the root mean square of the high pass filtered 500 hPa variability) induced by the tropical forcing. These changes are shown in Figure 4.9c,d. As expected, the storm track over the North Atlantic is shifted in such a way as to enhance the linear wave response in that sector for both "minus" and "plus" response cases, whereas over the North Pacific, the storm track response to the two opposite signs of SVD1 forcing are highly asymmetric and nonlinear. Hoerling et al. [2001b] have thoroughly investigated the extratropical climate response to the opposite phases of ENSO and attribute the nonlinearity to the nonlinear relationship between tropical Pacific rainfall and SST and the fact that convection responds to the total rather than the anomalous SST. By contrast, in this study, the anomalous diabatic forcing pattern is fixed in shape, merely changing sign between the "minus" and "plus" cases, yet the model behavior in the 500 hPa height and storm track response over the North Pacific is highly nonlinear, and might be a symptom of model deficiency over this area. So great caution should be taken to interpret the model results over the North Pacific sector. For comparison with observations (Figure 4.10a), we show the change in the model storm track in the nonlinear model when the forcing associated with SVD1 is applied globally. As before, there is general agreement between the change in the model storm track and the observations over the North Atlantic sector, although the agreement is better

over the North Atlantic when the forcing is appropriate for the later decades (Figure 4.10c). On the other hand, the change in the model storm track is much better over the North Pacific for the earlier decades case (Figure 4.10b) than the later decades case (Figure 4.10c).

4.3.3 The relationship between the location of tropical forcing and the extratropical response

It has been shown that the observed trend in NH tropospheric circulation can be largely explained by a planetary wave response to the changes in the tropical diabatic processes, though feedback from eddy fluxes associated with the storm track to the mean flow also plays an important role. Seeing the importance of the tropical forcing, it is natural to ask from which part of the tropics the trend-like wave train originates. The particular configuration of the planetary wave in Figures 4.7c and 4.9a suggests that the wave stems from the tropical Indo-Pacific region. To verify this, an experiment is conducted using the linearized model by specifying the SVD1 related forcing only within the Indo-Pacific region ($40°S-40°N$, $60°E-60°W$). The results are presented in Figure 4.11b. Comparing with the linear response to the forcing specified over the whole tropical band (Figure 4.7a), re-displayed as Figure 4.11a, we can see that the wave train signal is predominantly reproduced by the Indo-Pacific forcing only. The difference between Figures 4.11a and b can be largely attributed to the forcing over the western basin of the Indian Ocean and surrounding continents. Another experiment with the SVD1 forcing only specified over the tropical Atlantic region gives no eminent contribution to the wave train seen in Figure 4.11 (result not shown).

To further pinpoint from which part of the Indo-Pacific region the forcing is responsible for the wave signal over the North Atlantic or North Pacific sectors, two additional linear experiments are performed with the forcing specified over the western Indo-Pacific (60°E-180°W) and the eastern Pacific (180°W-60°W), respectively. The results are illustrated in Figure 4.12. Panel (a) clearly shows that the PNA-like

wave train over the Pacific sector is driven from the western Indo-Pacific. Whereas the Eastern Pacific forcing is responsible for the changes over the North Atlantic and a portion of high pressure anomalies over western North America. Since the tropical diabatic forcing is dominated by the latent and sensible heat release that is, in turn, related to the evolution of tropical SST, these linear model results suggest it is more likely the SST changes over the central and eastern tropical Pacific rather than those over the Indian ocean, as claimed by Hoerling and Hurrell [2002], that drive the tropospheric circulation trend over the North Atlantic. Indeed, the relationship between the location of forcing region and the maximum extratropical response is quite in keeping with that shown by Simmons et al. [1983], who used a barotropic version of the Hoskins and Simmons [1975] model. These authors investigated the sensitivity of the extratropical linear low-frequency wave response to tropical forcing. It was found that large perturbations over the North Pacific are most easily excited by forcing located over Southeast Asia and the tropical west Pacific Ocean, whereas, large perturbations over the Atlantic are predominantly excited by forcing from the eastern tropical Pacific. It should be noted that models are probably very sensitive in their extratropical teleconnection response to the details of the diabatic forcing seen by the model in the Indo-Pacific region (Branstator [1985]). Since most models compute their diabatic forcing interactively using the model physics package (unlike our model, the forcing for which is computed from observations), it is possible that the locations of the diabatic forcing generated by the specified tropical SST could be sensitive to the details of the model physics, and might not always pick out the correct geographical relationship between the location of the SST forcing and the prominent extratropical response excited by it.

Most recently, Deser et al. [2003] comprehensively analyzed the available instrumental records of tropical climate variables including rainfall, cloudness, and SST. The results suggest a coherent pattern of variability over the Indian Ocean and the central and eastern tropical Pacific on interdecadal time scales. Based on her work and the model results here, it is arguable that the whole tropical Indo-Pacific oceans

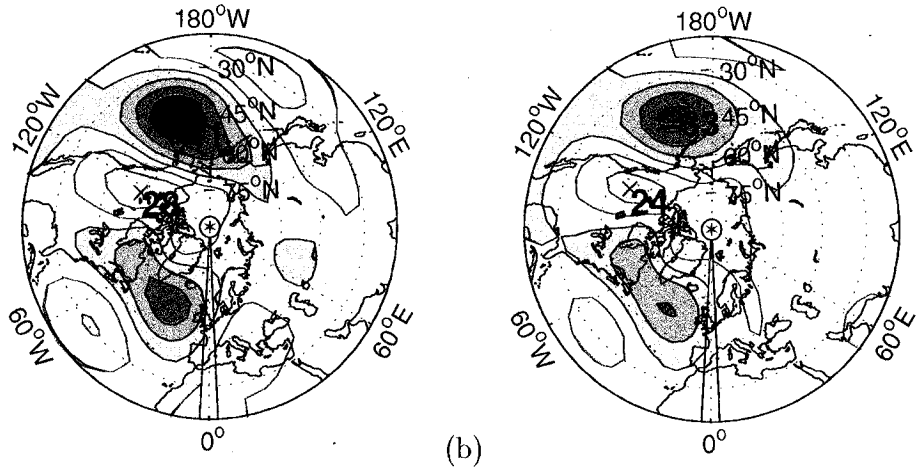

Figure 4.11: (a) Linear response of 500 hPa height to SVD1 tropical forcing, the same plot as Figure 4.7c, re-displayed for comparison; (b) linear response in 500 hPa height to SVD1 forcing restricted to the tropical Indo-Pacific. C.I.=10m/1 std of index.

should be involved in driving the interdecadal trend in the extratropical atmospheric circulation.

4.4 Conclusion and Discussion

This chapter examines the climate trend in the troposphere during the past 50 years. This period includes the last 20 years of the 20th century during which the NAO (Hurrell [1996]) and the AO (Thompson et al. [2000b]) exhibited a strong upward trend and which has attracted considerable attention because of the major impact of this trend on northern hemisphere climate, especially the Atlantic-European sector (e.g., Kushnir [1999]; Greatbatch [2000]; Hurrell et al. [2003]). For this reason, a comparison is made between the trend and AO in terms of their spatial patterns and driving mechanisms.

Here, attention is concentrated on the forcing of the NH climate change during the last 50 years. First, a SVD analysis is performed on the NH 500 hPa height and the model forcing diagnosed for the Hall model over the tropical Indo-Pacific region.

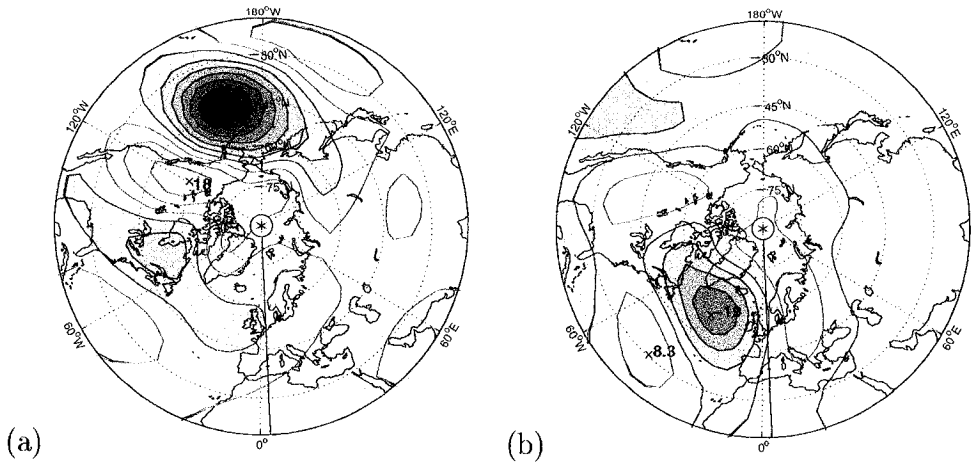

Figure 4.12: (a) Response in 500 hPa height to SVD1 forcing specified over the western Indo-Pacific (60°E-180°W) only in the linearized model; (b) same as (a) but to SVD1 forcing over the eastern Pacific (180°W-60°W) only. C.I.=5m/1 std of index.

The leading SVD mode relates a trend-like circulation pattern to tropical forcing that experienced an upward transition during the 1970's in its time evolution. The leading SVD mode of tropical model forcing was then applied to drive a dynamical model. The model is a dry, primitive equation model of the atmosphere (the Hall model) that can be run in both linear and nonlinear configurations. The model results show that the tropical-only forcing can reasonably capture the pattern of the observed trend over the whole NH with the attendant extra-tropical forcing playing a relatively minor role. The mechanism by which the extratropical circulation feels the tropical diabatic forcing is a planetary wave train that communicates the signal of the changes in the tropics to the extra-tropics. It has also been shown that the trend-like planetary wave train emanates from the tropical Indo-Pacific region, with the forcing over the western (eastern) Indo-Pacific more effective in exciting the perturbations over the North Pacific and North America (North Atlantic) region. After the passage of the wave train, the extra-tropical storm tracks feed back to and modulate the original wave signal. By unscrambling the effect of the model forcing using the linearized model and comparing it with the result from the full nonlinear model, we notice that

the model generated eddy forcing in the two storm track regions operates differently in contributing to the synchronous deepening trend of the Aleutian and Icelandic lows. Further examination of the storm track in the nonlinear SVD1 experiment reveals a fairly robust storm track response to our SVD1 forcing over the North Atlantic sector, whereas, the North Pacific storm track responds very nonlinearly to opposite signs of the same SVD1 forcing pattern. From the more faithful performance of the model over the North Atlantic sector, it is argued that the observed trend over the Euro-Atlantic sector during the last 50 years can be at least partly assigned to a resonant feedback between the low-frequency flow and the storm track, as a tele-response to the change in heating over the tropical Indo-Pacific region.

A change in the extratropical tropospheric circulation in response to tropical diabatic forcing can lead to a change in the sensible and latent heat release from the ocean to the atmosphere and in the associated diabatic heat release in the storm track (Hoskins and Valdes [1990]). It follows that the forcing associated with our SVD1 mode over the tropics and extratropics may not be independent of each other, as pointed out when we compared the linear model response to the SVD1-associated forcing specified over the tropics (Figure 4.7c) and extratropics (Figure 4.7e). In view of this, we speculate that the extratropical diabatic forcing associated with SVD1 (which is going along with the time series b(t)) might itself be the consequence of the tropical SVD1 forcing it is concomitant with. To substantiate this speculation on the relationship between the tropical and extratropical forcing, we have to resort to AGCMs that are able to interactively resolve the related diabatic processes.

The change in eddy activity associated with the SVD1 global diabatic forcing for the later decades case (see Figure 4.10c) not only resembles the anomalous storm track activity corresponding to the positive phase of the NAO, but is also similar to the pattern of increasing North Atlantic storm track activity in the ECHAM4/OPYC3 coupled model under increasing greenhouse gas (GHG) radiative forcing according to the IPCC IS92a scenario (Ulbrich and Christoph [1999], see their Fig. 2). Ulbrich and Christoph also noted that the signal of storm track activity corresponds to changes

in the upper tropospheric baroclinicity. Indeed, this is also the case in our model as driven by our SVD1 global forcing. We have calculated the anomalous Eady growth rate for the 300 to 500 hPa layer for this case. Despite the crude vertical resolution of the Hall model, the consistency between the storm activity (Figure 4.10c) and the growth rate (not shown) is remarkably good over both North Pacific and Atlantic sectors. In view of that, it may not be unreasonable to speculate that the changes in the North Atlantic storm activity driven by the SVD1 diabatic forcing could be a symptom traceable to GHG forcing (although the possibility has not been ruled out that the mechanisms responsible for the changes in the NAST activity shown in this study could be different from that driven by doubled CO_2 in Ulbrich and Christoph's scenario run). Given the fact that the tropical diabatic heating is dominated by the latent heat release associated with convective precipitation, it is likely that the diabatic heating pattern revealed by the first SVD is related to the precipitation changes associated with the tropical SST anomalies shown in Figure 4.2d (which is derived by regressing the time series of the first SVD for the tropical diabatic forcing onto the 51 winter mean SST from 1949 to 1999). Figure 4.2d is characterized by the warming trend over the tropical Pacific and Indian oceans, a pattern akin to the SST fingerprint driven by increased GHG in the coupled model of Knutson and Manabe [1998]. It is therefore possible that the SVD1 tropical diabatic heating and the associated tropical SST anomalies (and hence also the response to this heating, including the North Atlantic storm activity change) could be grouped under the banner of the GHG anthropogenic effect. Nevertheless, it is still an unresolved issue as to whether the warming trend in the tropical SST really is the fingerprint of the GHG forcing even though some model studies have suggested as much (e.g. Knutson and Manabe [1998]; Meehl and Washington [1996]). The interdecadal change in SST (as shown in Figure 4.2d) resembles the SST pattern associated with El Niño and the Pacific Decadal Oscillation (PDO, e.g., Mantua et al. [1997]) and this complicates the problem of detection and attribution of the anthropogenic fingerprint.

It is interesting to speculate whether the "COWL-like" pattern we have identified as describing the trend can itself be related to anthropogenic forcing. Palmer [1999] has pointed out, on the basis of studies of nonlinear chaotic systems with preferred states or "regimes", that the spatial patterns of the response to anthropogenic forcing may in fact project principally onto the preferred circulation regimes of the atmosphere. Corti et al. [1999] have argued that the change in the tropospheric circulation during the last 50 years can be interpreted in terms of an increase in the frequency of occurrence of a "COWL-like" pattern. A compelling question follows as to whether the "COWL-like" pattern is a preferred circulation regime? Indeed, the "COWL-like" regime emerges naturally from nonlinear regime extraction techniques, such as clustering analysis (e.g., Palmer [1999]; Corti et al. [1999]) or nonlinear principle component analysis (Monahan et al. [2001]). Furthermore, "COWL" can also be replicated by a low-order model as an equilibrium state in a hyperspace spanned by the leading EOF's of the reference GCM (D'Andrea [2002]). This serves as additional evidence for the natural existence of "COWL" from the perspective of dynamical systems. Physically, the existence of "COWL" is in debt to the contrast in thermal inertia between land and ocean, but not dependent on dynamical air-sea interaction or external radiation forcing (Wallace et al. [1995]; Broccoli et al. [1998]). Nevertheless, it has been reported that the tropical Pacific SST warming can generate substantial impact on the Probability Distribution Function (PDF) of the "COWL" regime (Palmer [1999]), leading to significant decadal average hemispheric-mean surface temperature differences (Kumar and Hoerling [1998]). The findings in the present study can be reconciled with this dynamical systems point of view by interpreting the trend since the late 1970's as a statistical consequence of the more frequent incidence of the "COWL-like" regime that itself is induced by the prevalently positive SVD1 tropical forcing we have identified.

Compared to COWL, the recent upward trend of the AO and NAO indices has attracted much more attention as an indicator of climate change under anthropogenic

forcing, although, hitherto, no consensus has been reached concerning the AO response to the increase of the concentration of atmospheric greenhouse gases and aerosols (Graf et al. [1998]; Ramaswamy et al. [2001]; Rind et al. [1998]; Schnadt et al. [2002]; Gillett et al. [2003]). Our study shows the merits of a "COWL-like" mode rather than the AO for describing the multidecadal trend in the tropospheric circulation, and that the "COWL-like" trend and at least some, if not all, of the linear trend in the AO are tropically driven from the Indo-Pacific region. The mechanism unraveled here whereby a tropical forcing source induces the extratropical circulation trend by driving a planetary wave train, which, in turn, induces a feedback between extratropical storm activity and the wave anomalies, provides a distinct pathway by which a long-term change in tropical diabatic processes can influence the extratropical circulation. Notwithstanding, the precise origin of the trend has yet to be finally pinpointed. If the trend is driven by changes in tropical SST, what mechanisms are important for determining the change in SST?(for an example involving dynamical wave processes within the tropical ocean, see Giese et al. [2002]) Further, are the changes in the tropics symptomatic of anthropogenic forcing? Answering these questions poses a challenge for future research.

Chapter 5

Non-stationary Impact of ENSO on Euro-Atlantic Climate

This chapter investigates the non-stationary impact of ENSO on the extratropical climate, in particular over the Euro-North Atlantic sector. An example of how the ENSO teleconnection varies with time can be manifested in terms of the running cross-correlation between the wintertime Tahiti-Darwin SO index (hereafter, SOI[1],Trenberth and Caron [2000]) and the COWL index (Section 1.2.2). As shown in Figure 5.1, an abrupt change occurred around the 1970's. After that time, the two indices became significantly anti-correlated at the 5% level, suggesting a favorable tropospheric circulation condition for the heat release from the oceans to the continents over the extratropics in recent El Niño events. Here, we choose two adjacent 20-year time windows 1958-77 and 1978-97 to represent the de-correlated and correlated periods between the ENSO and COWL, which are also the time periods used by Hilmer and Jung [2000] for analyzing the spatial pattern of the NAO. Following the convention, these two periods will still be referred to as P1 and P2, respectively. In addition to a regression analysis, sets of model experiments have been also conducted to gain some confidence in the result from regression analysis. This effort should lead to some insight into the possible mechanisms for the non-stationarity in the ENSO

[1]Or see http://www.cgd.ucar.edu/cas/ENSO/enso.html

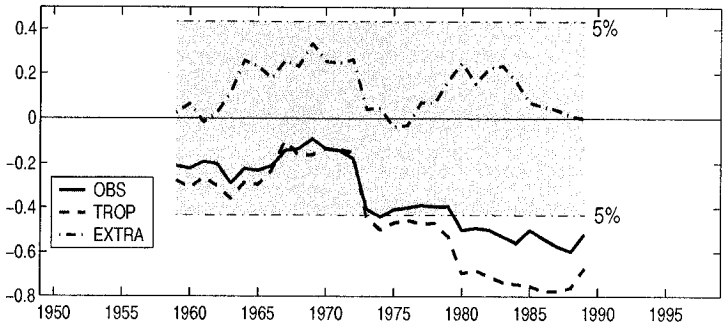

Figure 5.1: Running cross-correlation using a 21 year window between the observed SOI and the COWL index computed from the NCAR/NCEP data (solid line), and the ensemble mean tropically (dashed) and extratropically (dot-dash) forced model runs. The unshaded region marks the 5% significance level.

teleconnection in terms of the relative roles played by tropical and extratropical model forcing.

5.1 Regression Analysis

We begin by applying a regression analysis to winter (DJF) mean SLP and 1000 hPa air temperature taken from the NCAR/NCEP reanalysis (Kistler et al. [2001]) for 1948/49 to 1998/99. The regression pattern of SLP against SOI for all 51 winters 1949-99 is almost identical to that reported by Trenberth and Caron [2000] (their Fig. 4d) and is not shown here. Applying the regression to P1 and P2 time windows separately yields the patterns shown in Figure 5.2a and b, where the contour (color shading) indicates the regression coefficients of SLP (1000 hPa temperature). The features in common between the two panels, being also shared by the regression pattern for the whole 51 winters, are a high pressure anomaly over the northeastern Pacific and a low pressure anomaly to the southwest of it. The North Pacific SLP dipole gives rise to a tripolar pattern of temperature anomalies across the whole North Pacific, a feature being well accountable by the advection of the climatological mean temperature gradient by the anomalous geostrophic wind associated with the SLP

pattern. Nevertheless, the North Pacific SLP dipole differs substantially between the two regression periods. During period P2, the positive pole has been much expanded and strengthened while the negative pole weakened and displaced compared to P1. What is more striking is the difference over the North Atlantic and Europe sectors. During P1, the SLP regression pattern is characteristic of a meridional dipole with negative values to the north and positive values to the south, reminiscent of the positive phase of the NAO, and in keeping with the canonical response to ENSO (e.g., Fraedrich and Müller [1992]). Furthermore, the detailed impact on the European temperature by this anomalous circulation pattern, including cooler than normal conditions over the Iberian Peninsula, warmer than normal over the area between Scandinavia and British Isles, is largely consistent with Pozo-Vázquez et al. [2001]'s La Niña composites (see their Fig. 3d and e). After 1970's, the SLP signal flips its sign, consistent with the emergent link between ENSO and COWL shown in Figure 5.1. The associated wind between Iceland and North Sea reversed from westerly to easterly, resulting in opposite temperature anomalies over the Greenland Sea and Scandinavia. A similar reversal of wind and temperature also took place over Siberia and North Africa. A Student-t test indicates that only in a very limited area is the reversal of relationship to ENSO significant (not shown). For example, the 1000 hPa temperature to the southwest of the Red Sea is significantly anticorrelated (correlated) with SOI during P1 (P2). This result is in keeping with the changing relationship between the Red Sea coral record and Niño3 SST index from the pre-1970's to the post-1970's described by Rimbu et al. [2003].

5.2 Model Experiments and Results

To gain more confidence in the non-stationary behavior of ENSO, we put the question in a framework of an AGCM to see if this behavior can be captured by a numerical model governed by physical laws. Model experiments will also lead to some insight into the forcing mechanism for the changing teleconnection response to the ENSO

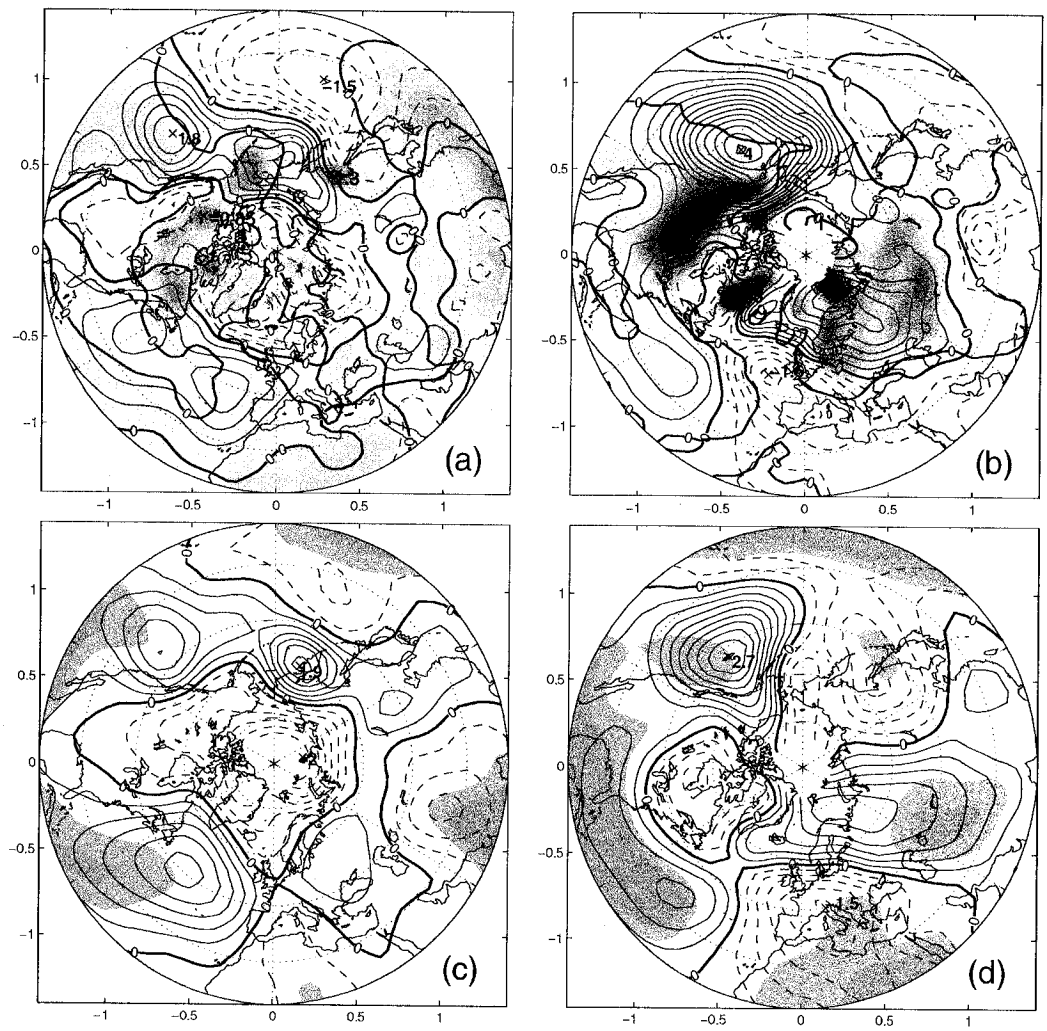

Figure 5.2: (a) and (b) are linear regression of NCAR/NCEP SLP (contours) and 1000 hPa temperature (color shading) against the observed SOI during P1 and P2 respectively. The zero isolines of the SLP (1000 hPa temperature) pattern are highlighted by thick black (green) lines. The contours in (c) and (d) are the same as those in (a) and (b) except for the model ensemble mean SLP driven by global forcing. Rigions significant from zero at the 5% confidence level, as determined by the Student's t-test, are denoted by gray shading. The contour interval is 0.3hPa/0.3^{o}C.

forcing.

Three sets of ensemble experiments have already been conducted in Section 4.2 with the forcing being applied in different model domains. In the first set of experiments, the whole globe is driven by the forcings varying from winter to winter; in the second, only in the tropical band equatorward of 36°N/S does the forcing vary according to different years, otherwise, the forcing is specified as the climatological average forcing for the 51 winters; in the third, the derived time-varying forcing is only applied in the extratropics. The reasons for choosing 36°N/S as the separation latitudes of tropics and extratropics has been discussed by Greatbatch et al.[2003] (see also the Appendix A).

In addition, a supplementary experiment is carried out making use of the regressed forcing against the SOI, a similar strategy having been implemented in Sections 3.3 and 4.3. We also run the linearized version of the Hall model, which is linearized about the climatology of the 51 winters, with the same ENSO regressed forcings specified globally and tropically.

The bottom panels of figure 5.2 show the ENSO teleconnection patterns during P1 and P2 in the globally forced case. The patterns are derived from regressing the model ensemble mean SLP for each winter against the observed SOI during P1 (Figure 5.2c) and P2 (Figure 5.2d). Comparing to the upper panels, the model can realistically capture the observed changes in the ENSO-related teleconnection over both Pacific and Atlantic sectors, lending us some confidence that there are deterministic reasons for the shift of ENSO teleconnection. Furthermore, we regressed the model forcing against the observed SOI within P1 and P2 separately and used the regressed forcing to drive the nonlinear model doing the ensemble of experiments. The ensemble mean SLP response to the regressed forcing for each period agrees qualitatively with the corresponding regression pattern shown in Figure 5.2 on all the major aspects, suggesting that the changing features of ENSO teleconnection can be largely attributed to the changing diabatic forcing associated with ENSO. The same conclusion can be reached from the result of linearized model experiments, wherein the

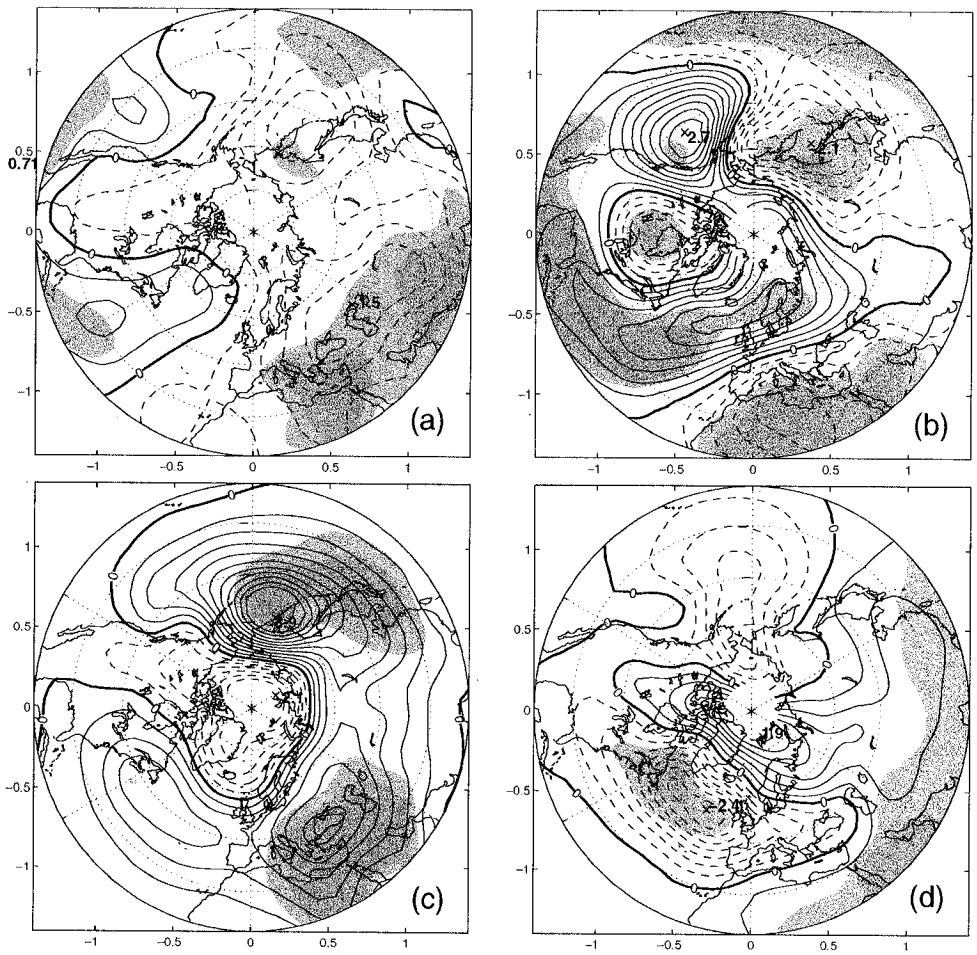

Figure 5.3: Linear regression against the observed SOI of the ensemble mean SLP from the model for tropical (a,b) and extratropical forcing (c,d) in P1 (a,c) and P2 (b,d). The grey shading indicates the 5% significance level (using Student's t-test). The contour interval is 0.3 hPa.

linearized model is driven by the same ENSO regressed forcing, while being devoid of the effects of transient eddy flux. The agreement between the nonlinear and linearized model experiments underlines the dominance of the diabatic forcing over the eddy forcing in exciting the extratropical teleconnection response to ENSO variability.

The source of ENSO variability comes from the dynamical and thermodynamical coupling between the tropical ocean and atmosphere. So, to trace the source of the shift in the extratropical teleconnection of ENSO, one has to turn attention to the diabatic forcing from the tropics. The same regression analysis is applied to the ensemble mean SLP from an ensemble of model runs, wherein the forcing varies from winter to winter only in the tropics. The results of regression against the observed SOI during P1 and P2 are plotted in Figure 5.3a and 5.3b respectively. Both show a PNA-like wave train (negative phase) emanating from the subtropical western Pacific. However, the amplitude of the signal is 2 or 3 times greater in P2 than in P1. A similar result is derived from a linearized model experiment driven by the ENSO regressed tropical forcing during P1 and P2, suggesting that this difference in amplitude is a feature of linear dynamics. Seeing this, one might expect the cause for the strengthened wave response to be enhanced diabatic forcing associated with the ENSO during P2. However, close inspection on the ENSO regressed forcing does not reveal any great difference in amplitude between those two periods. An example is given in Figure 5.4 of the forcing for the temperature equation regressed against SOI during P1 and P2 separately. No significant difference in amplitude can be seen between them. It has been reported that planetary waves can gain energy from the sources internal to the mean background flow (Branstator [1985]; Simmons et al. [1983]). It follows that the dramatically different response between P1 and P2 to rather similar tropical forcing may be due to the different mean states between these two periods. However, experiments using the model linearized about the different mean states for P1 and P2 do not show much dependence of the extratropical wave trains on the mean flow. Other mechanisms have to be invoked to understand this phenomenon. It has been demonstrated by Branstator [1985] that the mid-latitude response to a given tropical

forcing is highly dependent on the geographical position of the forcing. Furthermore, Branstator showed that the solution is sensitive to small details in the spatial pattern of the forcing. Thus, the increased wave response over the North Pacific and North America during P2 is most likely attributable to the slight changes of the spatial pattern of the forcing, with the forcing being more efficient at exciting the mid-latitude teleconnection in P2 than in P1. Also evident is the greater poleward penetration of the signal towards northern Europe in P2. Consequently, the signal emerging from the tropics bears a strong resemblance to the COWL pattern during P2. In fact, Figure 5.1 shows that the cross-correlation between the SOI and the COWL index for the tropically-forced ensemble mean model response increased dramatically between P1 and P2, with up to 60% of the variance in the tropically-emergent ENSO signal being accounted for by COWL during P2. Furthermore, there is no significant correlation in either P1 or P2 between the SOI and the COWL index for the extratropically forced model runs. It follows that the significant correlation between the SOI and COWL during P2 noted in the NCAR/NCEP data can attributed to the change in the signal emerging from the tropics between P1 and P2.

The teleconnection patterns of ENSO driven by the extratropical model forcing are shown in Figure 5.3c,d. These plots are derived by regression of ensemble mean SLP against the observed SOI when the model forcing varies from winter to winter only in the extratropics. Again we see a dramatic difference between P1 and P2. Interestingly, in this case, the extratropically-driven SLP pattern congruent with ENSO during both periods resembles the Arctic Oscillation, but with the sign reversed in P2 compared to P1. In P1, the ENSO-AO relationship suggested by Figure 5.3c is consistent with the canonical ENSO-Europe relationship, whereas, during P2 the extratropically-forced signal acts oppositely. Note that the teleconnection patterns shown in Figure 5.2c,d are given, to a good approximation, by simply adding the regression patterns shown in Figure 5.3a,b to those in Figure 5.3c,d, indicating the importance of linear dynamics. An important issue is whether the extratropical model forcing that is responsible for

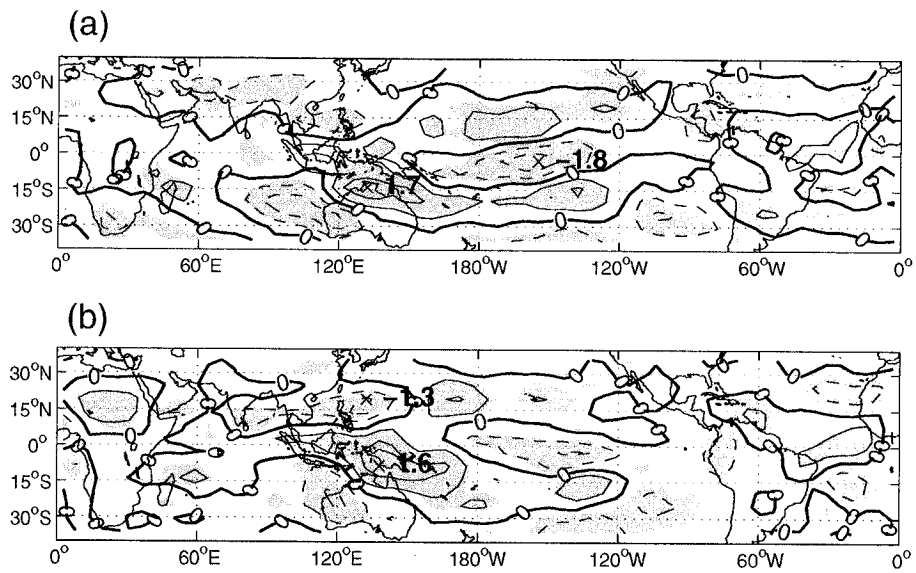

Figure 5.4: Regression of the vertically averaged forcing for the temperature equation against the observed SOI during P1 (panel a) and P2 (panel b). The 5% significant level is denoted by gray shading. The contour interval is 0.6°C per day.

the patterns shown in Figure 5.3c,d is itself a mid-latitude response to the tropically-forced signal shown in Figure 5.3a,b (e.g., due to latent heat release in the mid-latitude storm track), or is the difference between Figures 5.3c,d simply the result of chance? While this question cannot be answered definitely at this stage of research, we note that there are regions where the patterns shown in Figures 5.3c,d are statistically significant, suggestive of a genuine link with ENSO, but one that is hard to extract because of the dominance of other modes of variability in mid-latitudes.

5.3 Summary and Discussion

The link between ENSO and the Euro-Atlantic sector is not robust on interdecadal time scales (van Loon and Madden [1981]). An example is given in Figure 5.1 where

we show the running cross-correlation between the SOI and COWL index. The emergence of a significant anticorrelation between the SOI and COWL after the 1970's is not consistent with the canonical response to ENSO over the Euro-Atlantic sector documented by Fraedrich and Müller [1992]. By using a simple dynamical model, we have shown that the ENSO-related signal emerging from the tropics was between 2 and 3 times stronger in amplitude during P2 (1978-97) than during P1 (1958-77), as well as showing a greater poleward penetration during the later period that explains the emergent link with COWL. Model experiments also show that the extratropically forced model response congruent with ENSO resembles the AO pattern in both periods, but with the sign reversed, reinforcing the canonical ENSO response during P1 but countering it during P2. We suggest that the change in the extratropically-forced model response may partly be a consequence of the change in the ENSO signal emergent from the tropics, while recognizing that it may also have arisen by chance alone.

Chapter 6

Conclusions

During the last 50 years or so, the Northern Hemisphere winter climate underwent some changes at both interdecadal and interannual time scales. The interdecadal variability in the tropospheric circulation is characterized by a synchronous deepening trend in both the Aleutian and Icelandic lows, a pattern resembling the Cold Ocean Warm Land pattern and projecting positively on both the NAO and PNA modes. In the context of the interdecadal climate regime change, the spatial pattern of the interannual variability of the NAO shifted eastward during recent decades (1980's and 90's) compared to the earlier decades. The impacts of interannual ENSO variability on the extratropical teleconnection have also experienced some dramatic changes between the two periods. In combination with data analysis, atmospheric modelling has been used as a main tool to investigate the forcing mechanisms for these changes in terms of the relative roles played by tropical and extratropical forcings and the eddy flux associated with the Northern Hemisphere storm track. The main conclusions are following.

The eastward shift of the NAO pattern has been shown to be related to Rogers' leading mode of the North Atlantic storm activity, which, during recent two decades, explains 70% of the variance of the NAO. Since the late 1970's, when the shifted NAO pattern began to emerge, the NAO has been tied up strongly with Rogers' storm activity mode, ice flux anomalies through Fram Strait and Siberian winter temperature,

suggesting an emergent, spatially coherent climate regime over the Eurasia-North Atlantic sector.

Further, model experiments unraveled an eddy-driven mode showing a zonally oriented dipole in SLP with a low over Scandinavia and a high over southern Greenland. This pattern is dubbed "the NAO shift pattern" in this thesis and its time index shows a quadratic relationship with the NAO index. Thus, the NAO spatial pattern tends to be distorted in such a way that the northern center of action shifts eastward (westward) for the positive (negative) NAO phase. In this way, the eastward shift in the NAO pattern between P1 and P2 can be interpreted as a consequence of the high NAO index during P2 (average DJF index of 0.48) versus the low NAO index during P1 (average DJF index of -0.74), or in other words, the upward trend in the NAO index.

The upward trend in the winter NAO during the last half century is part of a hemispheric trend associated with a deepening of both the Icelandic and Aleutian lows. This trend has been shown to be largely attributed to a tropical source of forcing. The mechanisms by which the tropical forcing drives the trend in the extratropical, tropospheric circulation consist of a planetary wave train emanating from the tropical Indo-Pacific region and the feedback from the mid-latitude storm tracks to the original wave signal. Model results show robust storm track response over Euro-North Atlantic regions to the tropical forcing and help forge an argument that the upward trend of the NAO can be explained by a resonant feedback between the low-frequency flow and the storm track, as a tele-response to the change in heating over the tropical Indo-Pacific region.

Non-stationary behavior in the ENSO teleconnection has also been investigated in the context of the 1970's climate regime change. Running cross-correlation analysis reveals an emergence of a significant anticorrelation between the SOI and COWL after the 1970's, a teleconnection inconsistent with the canonical response to ENSO over the Euro-Atlantic sector documented by previous studies. By unscrambling the

tropical forcing from the extratropical forcing, we have shown that the tropically-forced ENSO teleconnection was between 2 and 3 times stronger in amplitude during P2 than during P1, as well as showing a greater poleward penetration during the later period that explains the emergent link with COWL. The most likely reason for the strengthened wave response during P2 might be due to the great sensitivity of the mid-latitude teleconnection to the geographical position of the forcing in the tropics. Slight changes in the forcing over the sensitive region, as occurred between P2 and P1, can lead to dramatic difference in the extratropical response.

Bibliography

K. Aagaard and E. C. Carmack. The role of sea-ice and other freshwater in the Arctic circulation. *J. Geophys. Res.*, 94:14485–14498, 1989.

M. H. P. Ambaum, B. J. Hoskins, and D. B. Stephenson. Arctic Oscillation or North Atlantic Oscillation? *J. Climate*, 14:3495–3507, 2001.

S.-I. An and B. Wang. Interdecadal changes of the structure of the ENSO modes and its impact on the ENSO frequency. *J. Climate*, 13:2044–2055, 2000.

J. K. Andell. Tropospheric temperature variations adjusted for El Niño, 1958-1998. *J. Geophys. Res.*, 105(D9):11841–11849, 2000.

T. P. Barnett. Variations in near-global sea level pressure. *J. Atmos. Sci.*, 42:478–501, 1985.

T. P. Barnett, D. W. Pierce, and R. Schnur. Detection of anthroponenic climate change in the world's oceans. *Science*, 292:270–274, 2001.

W. Bourke. A multi-level spectral model. I. Formulation and hemispheric integrations. *Mon. Wea. Rev.*, 102:687–701, 1974.

G. Branstator. Analysis of general circulation model sea-surface temperature anomaly simulations using a linear model. Part I: Forced solutions. *J. Atmos. Sci.*, 42:2225–2241, 1985.

C. S. Bretherton and D. S. Battisti. An interpretation of the results from atmospheric general circulation models forced by the time history of the observed sea surface temperature distribution. *Geophys. Res. Lett.*, 27:767–770, 2000.

C. S. Bretherton, C. Smith, and J. M. Wallace. An intercomparison of methods for finding coupled patterns in climate data. *J. Climate*, 5:541–560, 1992.

A. J. Broccoli, N.-C. Lau, and M. J. Nath. The Cold Ocean-Warm Land pattern: model simulation and relevance to climate change detection. *J. Climate*, 11:2743–2763, 1998.

R. E. Carnell, C.A. Senior, and J. F. B. Mitchell. An assessment of measure of storminess: simulated changes in northern hemisphere winter due to increasing CO_2. *Climate Dynamics*, 12:467–476, 1996.

B. A. Cash, P. J. Kushner, and G. K. Vallis. The structure and composition of the Annular Modes in an aquaplanet general circulation model. *J. Atmos. Sci.*, 59: 3399–3414, 2002.

C. Cassou, L Terray, J. W. Hurrell, and C. Deser. North Atlantic winter climate regimes: Spatial asymmetry, stationarity with time and oceanic forcing. *J. Climate*, (submitted), 2003.

E. K. M. Chang and Y.-F. Fu. Interdecadal variability in Northern Hemisphere winter storm track intensity. *J. Climate*, 15:642–658, 2002.

J. Chen, B. E. Carlson, and A. D. Del Genio. Evidence for strengthening of the tropical general circulation in the 1990s. *Science*, 295:838–841, 2002.

S. Corti, F. Molteni, and T. N. Palmer. Signature of recent climate change in frequencies of natural atmospheric circulation regimes. *Nature*, 398:799–802, 1999.

T. J. Crowley. Causes of climate change over the past 1000 years. *Science*, 289: 270–277, 2000.

A. Czaja, A. W. Robertson, and T. Huck. The role of Atlantic ocean-atmosphere coupling in affecting the North Atlantic Oscillation variability. *AGU Geophysical monograph 134: The North Atlantic Oscillation*, 10.1029/134GM07, 2003.

F. D'Andrea. Extratropical low-frequency variability as a low-dimensional problem. II: Stationary and stability of large-scale equilibria. *Q. J. Roy. Meteorol. Soc.*, 128: 1059–1073, 2002.

C. Deser, A. S. Phillips, and J. W. Hurrell. Pacific interdecadal climate variability: Linkage between the tropics and North Pacific during boreal winter since 1900. *J. Climate*, (submitted), 2003.

H. F. Diaz and N. E. Graham. Recent changes in tropical freezing heights and the role of sea surface temperature. *Nature*, 383:152–155, 1996.

R. R. Dickson, J. Meinke, S.-A. Malmberg, and A. J. Lee. The Great Salinity Anomaly in the Northern North Atlantic, 1968-1982. *Prog. Oceanogr.*, 20:103–151, 1988.

M. N. Evans, A. Kalpan, M. A. Cane, and R. Villalba. *Present and past inter-hemispheric climate linkage in the Americas and their societal effects.* Cambridge Univ. Press, Cambridge, 2001.

S. B. Feldstein. The recent trend and variance increase of the Annular Mode. *J. Climate*, 15:88–94, 2002.

K. Fraedrich. European Grosswetter during the warm and cold extremes of the El Niño/Southern Oscillation. *Inter. J. Climatol.*, 10:21–31, 1990.

K. Fraedrich. An ENSO impact on Europe? *Tellus*, 46A:541–552, 1994.

K. Fraedrich and K. Müller. Climate anomalies in Europe associated with ENSO extremes. *Int, J. Climatol.*, 12:25–31, 1992.

J. C. Fyfe, Boer G. J., and G. M. Flato. The Arctic and Antarctic Oscillations and their projected changes under global warming. *Geophys. Res. Lett.*, 26:1601–1604, 1999.

D. J. Gaffen. Temporal inhomogeneities in radiosonde temperature records. *J. Geophys. Res.*, 99(D2):3667–3676, 1994.

D. J. Gaffen, B. D. Santer, J. S. Boyle, J. R. Christy, N. E. Graham, and R. J. Ross. Multidecadal changes in the vertical temperature structure of the tropical troposphere. *Science*, 287:1242–1245, 2000.

R. D. Garreaud and D. S. Battisti. Interannual (ENSO) and interdecadal (ENSO-like) variability in the Southern Hemisphere tropospheric circulation. *J. Climate*, 12:2113–2123, 1999.

B. S. Giese, S. C. Urizar, and N. S. Fučkar. Southern Hemisphere origin of the 1976 climate shift. *Geophys. Res. Lett.*, 29:10.1029/2001GL013268, 2002.

N. P. Gillett, H. F. Graf, and T. J. Osborn. Climate change and the North Atlantic Oscillation. *AGU Geophysical monograph 134: The North Atlantic Oscillation*, 10.1029/134GM09, 2003.

N. P. Gillett, G. C. Hegerl, M. R. Allen, and P. A. Stott. Implications of changes in the Northern Hemisphere circulation for the detection of anthropogenic climate change. *Geophys. Res. Lett.*, 27:993–996, 2000.

H. F. Graf, I. Kirchner, and J. Perlwitz. Changing lower stratospheric circulation: The role of ozone and greenhouse gases. *J. Geophys. Res.*, 103:11251–11261, 1998.

N. E. Graham. Decadal-scale climate variability in the tropical and North Pacific during the 1970s and 1980s: observations and model results. *Clim. Dyn.*, 10:135–162, 1994.

R. J. Greatbatch. The North Atlantic Oscillation. *Stochastic Environmental Research and Risk Assessment*, 14:213–242, 2000.

R. J. Greatbatch, H. Lin, J. Lu, K. A. Peterson, and J. Derome. Tropical/Extratropical forcing of the AO/NAO: A corrigendum. *Geophys. Res. Lett.*, 30(14):10.1029/2003GL017406, 2003.

D. Gu and S. G. H. Philander. Interdecadal climate fluctuations that depend on exchanges between the tropics and extratropics. *Science*, 275:805–807, 1997.

S. Häkkinen. An Arctic source for the Great Salinity Anomaly: A simulation of the Arctic ice-ocean system for 1955-1975. *J. Goephys. Res.*, 98:16397–16410, 1993.

N. M. J. Hall. A simple GCM based on dry dynamics and constant forcing. *J. Atmos. Sci*, 57:1557–1572, 2000.

N. M. J. Hall, B. J. Hoskins, P. J. Valdes, and C. A. Senior. Storm track in a high-resolution GCM with doubled carbon dioxide. *Q. J. R. Meterorol. Soc.*, 120: 1209–1230, 1994.

N. M. J. Hall and P. D. Sardeshmukh. Is the time-mean Northern Hemisphere flow baroclinically unstable? *J. Atmos. Sci.*, 55:41–56, 1998.

D. L. Hartmann, J. M. Wallace, V. Limpasuvan, D. W. J. Thompson, and J. R. Holton. Can ozone depletion and global warming interact to produce rapid climate change? *Proc. Nat. Acad. Sci.*, 97:1412–1417, 2000.

M. Hilmer and T. Jung. Evidence for a recent change in the link between the North Atlantic Oscillation and Arctic sea ice export. *Geophys. Res. Lett.*, 27:989–992, 2000.

M. P. Hoerling and J. W. Hurrell. North Atlantic climate change as a response to Indian Ocean warming. *Eos Trans. AGU*, 83(19):Spring Meeting, Suppl., Abstract GC41A–07, 2002.

M. P. Hoerling, J. W. Hurrell, and T. Xu. Tropical origins for recent North Atlantic climate change. *Science*, 292:90–92, 2001a.

M. P. Hoerling, A. Kumar, and T. Xu. Robustness of the nonlinear climate response to ENSO's extreme phases. *J. Climate*, 14:1277–1293, 2001b.

M. Honda and H. Nakamura. Interannual seasaw between the Aleutian and Icelandic lows. Part II: Its significance in the interannual variability over the wintertime Northern Hemisphere. *J. Climate*, 14:4512–4529, 2001b.

M. Honda, H. Nakamura, J. Ukita, I. Kousaka, and K. Takeuchi. Interannual seasaw between the Aleutian and Icelandic lows. Part I: Seasonal dependence and life cycle. *J. Climate*, 14:1029–1042, 2001a.

B. J. Hoskins and A. J. Simmons. A multi-layer spectral model and the semi-implicit method. *Quart. J. R. Met. Soc.*, 101:637–655, 1975.

B. J. Hoskins and P. J. Valdes. On the existence of storm tracks. *J. Atmos. Sci.*, 47: 1854–1864, 1990.

J. T. Houghton, L. G. Meira Filho, B. A. Callender, N. Harris, A. Kattenberg, and K. Maskell. *Climate Change 1995: the science of climate change.* Cambridge Univ. Press, Cambridge, 1995.

J. W. Hurrell. Transient Eddy Forcing of the rotational flow during northern winter. *J. Atmos. Sci.*, 52:2286–2301, 1995a.

J. W. Hurrell. Decadal trends in the North Atlantic Oscillation: Regional temperatures and precipitation. *Science*, 269:676–679, 1995b.

J. W. Hurrell. Influence of variations in extratropical wintertime teleconnection on Northern Hemisphere temperature. *Geophys. Res. Lett.*, 23:665–668, 1996.

J. W. Hurrell, Y. Kushnir, G. Ottersen, and M. Visbeck. An overview of the North Atlantic Oscillation. *AGU Geophysical monograph 134: The North Atlantic Oscillation*, 10.1029/134GM01, 2003.

I. N. James and P. M. James. Ultra-low-frequency variability in a simple atmospheric circulation model. *Nature*, 342:53–55, 1989.

F.-F. Jin and B. J. Hoskins. The direct response to tropical heating in a baroclinic atmosphere. *J. Atmos. Sci.*, 52:307–319, 1995.

P. D. Jones. The early twentieth century Arctic High–fact or fiction? *Clim. Dyn.*, 1: 63–75, 1987.

T. Jung and M. Hilmer. On the link between the North Atlantic Oscillation and Arctic sea ice export through Fram Strait. *J. Climate*, 14:3932–3943, 2001.

E. Kalnay, M. Kanamitsu, R. Kistler, and et al. The NCEP/NCAR 40 years reanalysis project. *Bull. Amer. Met. Soc.*, 77:437–471, 1996.

M Kimoto and M. Ghil. Multiple flow regimes in the northern hemisphere winter. Part I: methodology and hemispheric regimes. *J. Atmos. Sci.*, 50:2625–2643, 1993.

R. Kistler, W. Collins, S. Saha, G. White, J. Woollen, E. kalnay, M. Chelliah, W. Ebisuzaki, M. Kanamitsu, V. Kousky, H. van den Dool, R. Jenne, and M. Fiorino. The NCEP-NCAR 50-year reanalysis: monthly means CD-ROM and documentation. *Bull. Amer. Met. Soc.*, 82:247–268, 2001.

T. R. Knutson and S. Manabe. Model assessment of decadal variability and trends in the tropical Pacific ocean. *J. Climate*, 11:2273–2296, 1998.

A. Kumar and M. P. Hoerling. On the specification of regional SSTs in AGCM simulations. *J. geophys. Res.*, 103:8901–8907, 1998.

Y. Kushnir. Europe's winter prospects. *Nature*, 398:289–291, 1999.

Y. Kushnir, W. A. Robinson, I. Bladé, N. M. J. Hall, S. Peng, and R. Sutton. Atmospheric GCM response to extratropical SST Anomalies: Synthesis and evaluation. *J. Climate*, 15:2233–2256, 2002.

R. Kwok. Recent changes in Arctic Ocean sea ice motion associated with the North Atlantic Oscillation. *Geophys. Res. Lett.*, 27:775–778, 2000.

R. Kwok and D. A. Rothrock. Variability of Fram Strait ice flux and North Atlantic Oscillation. *J. Geophys. Res.*, 104(C3):5177–5189, 1999.

M. Latif, K. Arpe, and E. Roeckner. Oceanic control of decadal North Atlantic sea level pressure variability in winter. *Geophys. Res. Lett.*, 27:727–730, 2000.

M Latif and T. P. Barnett. Causes of decadal climate variability over the North Pacific and North America. *Science*, 266:634–637, 1994.

M Latif and T. P. Barnett. Decadal climate variability over the North Pacific and North America: Dynamics and Predictability. *J. Climate*, 9:2407–2423, 1996.

N.-C Lau. Variability of the observed midlatitude storm tracks in relation to low-frequency changes in the circulation pattern. *J. Atmos. Sci.*, 45:2718–2743, 1988.

N.-C. Lau and E. O. Holopainen. Transient eddy forcing of the time-mean flow as identified by geopotential tendencies. *J. Atmos. Sci.*, 41:313–328, 1984.

N.-C. Lau and M. J. Nath. Variability of the baroclinic and barotropic transient eddy forcing associated with monthly changes in the midlatitude storm track. *J. Atmos. Sci.*, 48:2589–2613, 1991.

S. Levitus, J. I. Antonov, T. P. Boyer, and C. Stephens. Warming of the world ocean. *Science*, 287:2225–2229, 2000.

S. Levitus, J. I. Antonov, J. Wang, T. L. Delworth, K. W. Dixon, and A. J. Broccoli. Anthropogenic warming of earth's climate system. *Science*, 292:267–270, 2001.

V. Limpasuvan and D. L. Hartmann. Eddies and the annular modes of climate variability. *Geophys. Res. Lett.*, 26:3133–3136, 1999.

V. Limpasuvan and D. L. Hartmann. Wave-maintained annular modes of climate variability. *J. Climate*, 13:4414–4429, 2000.

H. Lin, J. Derome, R. J. Greatbatch, K. A. Peterson, and J. Lu. Tropical links for the Arctic Oscillation. *Geophys. Res. Lett.*, 29(9):10.1029/2001GL015822, 2002.

R. S. Lindzen and C. Giannitsis. Reconciling observations of global temperature change. *Geophys. Res. Lett.*, 29(12):10.1029/2001GL014074, 2002.

B. K. Linsley, G. M. Wellington, and D. P. Schrag. Decadal sea surface temperature variability in the subtropical South Pacific from 1726 to 1997 A.D. *Science*, 290: 1145–1148, 2000.

J. Lu and R. J. Greatbatch. The changing relationship between the NAO and northern hemisphere climate variability. *Geophys. Res. Lett.*, 29(7):10.1029/2001GL014052, 2002.

N. J. Mantua, S. R. Hare, Y. Zhang, J. M. Wallace, and R. C. Francis. A Pacific interdecadal climate oscillation with impacts on salmon production. *Bull. Amer. Met. Soc.*, 78:1069–1079, 1997.

A. Mariotti, N. Zeng, and K. M. Lau. Euro-Mediterranean rainfall and ENSO - a seasonally varying relationship. *Geophys. Res. Lett,*, 29:10.1029/2001GL014248, 2002.

J. Marshall and F. Molteni. Toward a dynamical understanding of planetary-scale flow regimes. *J. Atmos. Sci.*, 50:1792–1818, 1993.

M. J. McPhaden and D. Zhang. Slowdown of the meridional overturning circulation in the upper Pacific Ocean. *Nature*, 415:603–608, 2002.

G. A. Meehl and W. M. Washington. El Niño-like climate change in a model with increased atmospheric CO_2 concentrations. *Nature*, 382:56–60, 1996.

V. M. Mehta, M. J. Suarez, J. Manganello, and T. L. Delworth. Ocean influence on the North Atlantic Oscillation and associated northern hemisphere climate variations: 1959-1993. *Geophys. Res. Lett.*, 27:121–124, 2000.

U. Merkel and M. Latif. A high resolution AGCM study of the El Nino impact on the North Atlantic/European sector. *Geophys. Res. Lett.*, 29:10.1020/2001GL013726, 2002.

A. H. Monahan, L. Pandolfo, and J. C. Fyfe. The preferred structure of variability of the Northern Hemisphere atmospheric circulation. *Geophys. Res. Lett.*, 28:1019–1022, 2001.

T. Nitta and S. Yamada. Recent warming of tropical sea surface temperature and its relationship to the Northern Hemisphere circulation. *J. Meteorol. Soc. of Japan*, 67:375–383, 1989.

T. N. Palmer. A nonlinear dynamical perspective on climate change. *Weather*, 48: 313–348, 1993.

T. N. Palmer. A nonlinear dynamical perspective on climate prediction. *J. Climate*, 12:575–591, 1999.

K. A. Peterson, R. J. Greatbatch, J. Lu, H. Lin, and J. Derome. Hindcasting the NAO using diabatic forcing of a simple AGCM. *Geophys. Res. Lett*, 29(9): 10.1029/2001GL014502, 2002.

D. Pozo-Vázquez, M. J. Esteban-Parra, F. S. Rodrigo, and Y. Castro-Díez. The association between ENSO and winter atmospheric circulation and temperature in the North Atlantic region. *J. Climate*, 14:3408–3420, 2001.

C. Price, L. Stone, A. Huppert, B. Rajagopalan, and P. Alpert. A possible link between El Nino and precipitation in Israel. *Geophys. Res. Lett.*, 25:3963–3966, 1998.

V. Ramaswamy, M.-L. Chanin, J. Angell, J. Barnett, D. Gaffen, M. Gelman, P. Keckhut, Y. Koshelkov, K. Labitzke, J.-J. R. Lin, A. O'Neill, J. Nash, W. Randel, R. Rood, K. Shine, M. Shiotani, and R. Swinbank. Stratospheric temperature

trends: Observations and model simulations. *Reviews of Geophysics*, 39:71–122, 2001.

W. J. Randel, F. Wu, and D. J. Gaffen. Interannual variability of the tropical tropopause derived from radiosonde data and NCEP reanalyses. *J. Geophys. Res.*, 105(D12):15509–15523, 2000.

E. M. Rasmusson and T. H. Carpenter. Variations in the tropical sea surface temperature and surface wind fields associated with the Southern Oscillation/El Niño. *Mon. Wea. Rev.*, 110:354–384, 1982.

B. K. Reichert, R. Schnur, and L. Bengtsson. Global warming tied to anthropogenic forcing. *Geophy. Res. Lett.*, 29(11):10.1029/2001GL013954, 2002.

N. Rimbu, G. Lohmann, T. Felis, and J. Pätzold. Shift in ENSO teleconnections recorded by a northern Red Sea coral. *J. Climate*, 16:1414–1422, 2003.

D. Rind, D. Shindell, P. Lonergan, and N. K. Balachandran. Climate change and middle atmosphere. Part III: The doubled CO_2 climate revisited. *J. Climate*, 11: 876–894, 1998.

X. Rodo, E. Baert, and F. A. Comin. Variations in seasonal rainfall in Southern Europe during the present century: relationships with the North Atlantic Oscillation and the El Niño-Southern Oscillation. *Clim. Dyn.*, 13:275–284, 1997.

M. J. Rodwell, D. P. Rowell, and C. K. Folland. Oceanic forcing of the wintertime North Atlantic Oscillation and European climate. *Nature*, 398:320–323, 1999.

J. C. Rogers. The Association between the North Atlantic Oscillation and the Southern Oscillation in the Northern Hemisphere. *Mon. Wea. Rev.*, 112:1999–2015, 1984.

J. C. Rogers. Atlantic storm track variability and its association to the North Atlantic Oscillation and climate variability of Northern Europe. *J. Climate*, 10:1635–1647, 1997.

J. C. Rogers and E. Mosley-Thompson. Atlantic Arctic cyclones and the mild Siberian winters of the 1980s. *Geophys. Res. Lett.*, 22:799–802, 1995.

B. D. Santer, T. M. L. Wigley, D. J. Gaffen, and et al. Interpreting differential temperature trends at the surface and in the lower troposphere. *Science*, 287: 1227–1232, 2000.

C. Schnadt, M. Dameris, M. Ponater, R. Hein, V. Grewe, and B. Steil. Interaction of atmospheric chemistry and climate and its impact on stratospheric ozone. *Clim. Dyn.*, 18:501–517, 2002.

D. T. Shindell, R. L. Miller, G. A. Schnidt, and L. Pandolfo. Simulation of recent northern climate trends by greenhouse gas forcing. *Nature*, 399:452–455, 1999.

A. J. Simmons, J. M. Wallace, and G. W. Branstator. Barotropic wave propagation and instability, and atmospheric teleconnection patterns. *J. Atmos. Sci.*, 40:1363–1392, 1983.

C. Stephens, S. Levitus, J. Antonov, and T. P. Boyer. On the Pacific Ocean regime shift. *Geophys. Res. Lett.*, 28(19):3721–3724, 2001.

P. A. Stott, S. F. B. Tett, G. S. Jones, M. R. Allen, J. F. B. Mitchell, and G. J. Jenkins. External control of 20th century temperature by natural and anthropogenic forcings. *Science*, 290:2133–2137, 2000.

S. F. B. Tett, J. F. B. Mitchell, D. E. Parker, and M. R. Allen. Human influence on the atmospheric vertical temperature structure: Detection and observations. *Science*, 274:1170–1173, 1996.

D. W. J. Thompson, S. Lee, and M. P. Baldwin. Atmospheric processes governing the Northern Hemisphere Annular Mode/North Atlantic Oscillation. *AGU Geophysical monograph 134: The North Atlantic Oscillation*, 10.1029/134GM03, 2003.

D. W. J. Thompson and J. M. Wallace. Annular modes in the extratropical circulation. Part I: Month-to-month variability. *J. Climate*, 13:1000–1016, 2000a.

D. W. J. Thompson, J. M. Wallace, and G. C. Hegerl. Annular modes in the extratropical circulation. Part II: Trends. *J. Climate*, 13:1018–1036, 2000b.

M. Ting and N.-C. Lau. A diagnostic and modeling study of the monthly mean wintertime anomalies appearing in an 100 year GCM experiment. *J. Atmos. Sci.*, 50:2845–2867, 1993.

K. E. Trenberth, G. W. Branstator, D. Karoly, A. Kumar, N.-C. Lau, and C. Ropelewski. Progress during TOGA in understanding and modeling global teleconnections associated with tropical sea surface temperatures. *J. Geophys. Res.*, 103 (C7):14291–14324, 1998.

K. E. Trenberth and J. M. Caron. The Southern Oscillation revisited: sea level pressures, surface temperatures, and precipitation. *J. Climate*, 13:4358–4365, 2000.

K. E. Trenberth, J. M. Caron, D. P. Stephaniak, and S. Worley. Evolution of El Niño-Southern Oscillation and global atmospheric surface temperatures. *J. Geophys. Res.*, 107:10.1029/2000/D000298, 2002.

K. E. Trenberth and T. J. Hoar. The 1990-1995 El Niño-Southern Oscillation Event: Longest on record. *Geophys. Res. Lett.*, 23:57–60, 1996.

K. E. Trenberth and J. W. Hurrell. Decadal atmospher-ocean interactions in the Pacific. *Clim. Dyn.*, 9:303–319, 1994.

U. Ulbrich and M. Christoph. A shift of the NAO and increasing storm track activity over Europe due to anthropogenic gas forcing. *Climate Dynamics*, 15:551–559, 1999.

H. van Loon and R. A. Madden. The Southern Oscillation. Part I: Global association with pressure and temperature in northern winter. *Mon. Wea. Rev.*, 109:1150–1162, 1981.

J. M. Wallace and D. S. Gutzler. Teleconnection in the geopotential height field during the Northern Hemisphere winter. *Mon. Wea. Rev.*, 109:784–812, 1981.

J. M. Wallace, E. M. Rasmusson, T. P. Mitchell, V. E. Kousky, E. S. Sarachick, and H. von Storch. On the structure and evolution of ENSO-related climate variability in the tropical Pacific: Lessons from TOGA. *J. Geophys. Res.*, 103:14241–14260, 1998.

J. M. Wallace, C. Smith, and C. S. Bretherton. Singular value decomposition of wintertime sea surface temperature and 500-mb height anomalies. *J. Climate*, 5: 561–576, 1992.

J. M. Wallace, Y. Zhang, and L. Bajuk. Interpretation of interdecadal trends in Northern Hemisphere surface air temperature. *J. Clim.*, 9:249–259, 1996.

J. M. Wallace, Y. Zhang, and J. A. Renwick. Dynamical contribution to hemispheric temperature trends. *Science*, 270:780–783, 1995.

B. Wang. Interdecadal changes in El Niño onset in the last four decades. *J. Climate*, 8:267–285, 1995.

B. A. Wielicki, T. Wong, R. P. Allan, and et al. Evidence for large decadal variability in the tropical mean radiative energy budget. *Science*, 295:841–844, 2002.

C. Wunsch. The interpretation of short climate records, with comments on the North Atlantic and Southern Oscillations. *Bull. Amer. Met. Soc.*, 80(245–255), 1999.

Y. Xue. Interdecadal changes of 30-yr SST normals during 1871-2000. *J. Climate*, 16:1601–1612, 2003.

Y. Zhang, J. M. Wallace, and D. Battisti. ENSO-like interdecadal variability: 1900-1993. *J. Climate*, 10:1004–1020, 1997.

Appendix A

Tropical/Extratropical Forcing Separation

In Chapter 4, where we discussed the driving mechanism for the AO/NAO and the multidecadal climate change in terms of the relative contribution of the proxy diabatic forcing from the tropics and extratropics, experiments were carried out with the time-dependent or the regressed forcing confined to a subregion of the model domain, with the climatological forcing specified in the remaining part of the domain. In this thesis, the forcing split for the tropical/extratropical experiments is carried out at $36°N$ and $36°S$, different from the latitudes chosen to make the split (i.e., $30°N$ and $30°S$) in Peterson et al. [2002] and Lin et al. [2002]. The reason behind choosing a different split is a problem we found in the way of doing the tropical/extratropical split used by Peterson et al. and Lin et al.. This appendix addresses how to properly specify the forcing in a confined region without introducing potentially serious spurious effects along the boundary of the region.

As introduced in Chapter 2, the model used in this thesis study is the Hall model, a simple, dry dynamical model of the atmosphere with linear damping and driven by forcing computed from the NCAR/NCEP reanalysis data. The method of computing the forcing has been described in detail in Chapter 2. The forcing mimics processes not explicitly included in the model code, and is dubbed "diabatic" forcing for the

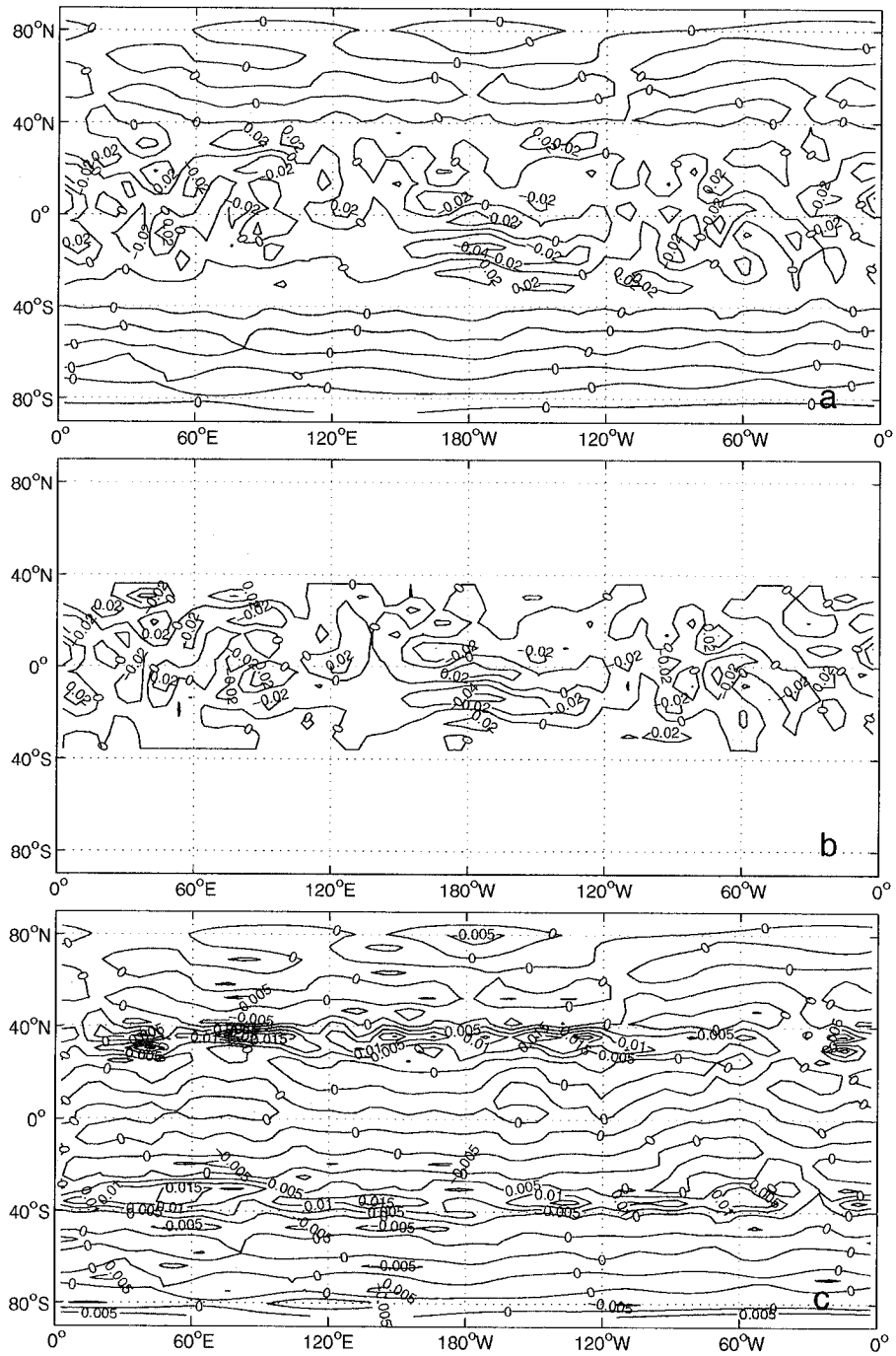

Figure A.1: (a) The resultant anomalous forcing for the divergence equation by zeroing out the AO-regressed forcing poleward of 36°N/S for momentum equations using the old approach; (b) Same as (b) but using the new approach, i.e., the zeroing out is carried out directly on the forcing for the divergence equation; (c) is the difference of (a) minus (b). The values are nondimensional. C.I. is 0.02 in (a) and (b), 0.005 in (c).

atmosphere (see Chapter 2 for detail explanation). However, it is important to appreciate that the computed forcing does not sit entirely on the temperature equation. In fact, all the prognostic equations of the model are forced including the equations for vorticity, divergence and surface pressure. Of particular concern is the forcing applied to the vorticity and divergence equations, since special care is required in the treatment of these equations when splitting the anomalous forcing between the tropics and the extratropics. In Peterson et al.[2002] and Lin et al.[2002], the split was carried out as follows: first, the global forcing (in spectral space) for the vorticity and divergence equations was first transformed to the equivalent forcing for the momentum equations; then, to split the forcing between the tropics and extratropics, the anomalous forcing (that is, difference from the mean for all 51 winters) for the momentum equations was zeroed out poleward (equatorward) of $30°N$ and $30°S$ on the Gaussian grid in the tropical (extratropical) forcing case; last, the resultant tropical (extratropical) forcing was transformed back to a forcing for the vorticity and divergence equations in spectral space. Since the last step involves taking derivatives of the momentum forcing with respect to the horizontal coordinates, the effect of this procedure is to introduce spurious "spikes" to the forcing for the vorticity and divergence equations along the latitudes of the split. To avoid this artificial effect, the splitting should be operated on the anomalous divergence and vorticity forcing directly, without recourse to the corresponding momentum equations. Figure A.1 gives an example comparing the results of zeroing out the AO regressed forcing poleward of $36°N$ and $36°S$ using different methods. The contours plotted are the vertical average of the forcing for the divergence equation on all the 5 model levels. Obviously, comparing to the new result (Figure A.1b), splitting the forcing in the momentum equations (Figure A.1a) gives rise to some unwanted noise outside of the tropical band. The error, plotted as the difference obtained by subtracting (b) from (a), is characterized by two strips of "spikes" along $36°N$ and $36°S$.

Another caution should be used when removing the anomalous forcing for the vorticity and divergence equations from a certain domain. It is required that the global

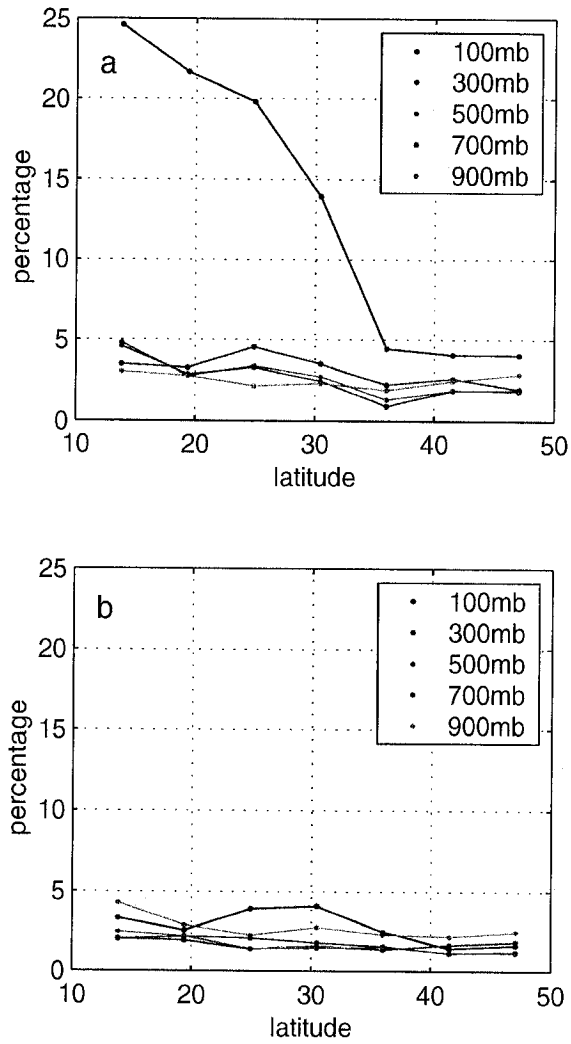

Figure A.2: The average of the anomalous forcing for (a) the divergence and (b) the vorticity equations on each model levels and within a latitude band centered on the equator, plotted as a function of the outer bounding latitude, averaged over all 51 winters, and expressed as a percentage of the area-weighted standard deviation of the forcing over the global domain.

integral of the forcing for the vorticity and divergence equations be zero on each vertical level as indicated by the fact that the forcing is derived from the equivalent forcing for the momentum equations by taking the curl and divergence of those equations (Bourke [1974]). Therefore, when splitting the forcing into tropical and extratropical parts, it is important to choose the lines of latitude demarking the tropics from the extratropics in such a way that the area integrals of the anomalous forcing for vorticity and divergence within each region are both close to zero. To illustrate this, Figure A.2 shows the result of averaging the forcing for the divergence and vorticity equations over the area contained within a latitude band centered on the equator. In the figure, this spatial (area-weighted) and time (over all 51 winters) average on each of the 5 model levels is plotted against the outer bounding latitude as a percentage of the area-weighted standard deviation of the forcing over the globe. It is clear that the most significant departure from zero occurs on the top model level (nominally 100 hPa) for the anomalous forcing of the divergence equation (Figure A.2a), and that the value of the integral is significantly reduced if the tropical/extratropical forcing split is carried out at $36°N$ and $36°S$ rather than at $30°N$ and $30°S$. For this reason, in this thesis, all the tropical/extratropical forcing decomposition is conducted along $36°N$ and $36°S$. The anomalous forcing of the vorticity equation is of much less concern seeing that none of the tropical integral exceeds 5% of the area-weighted standard deviation of the forcing over the globe.

We have investigated the influence of splitting the forcing in the two different ways on the model performance on the AO/NAO for the tropical/extratropical forcing case (Greatbatch et al. [2003]). Repeating the experiments in Peterson et al.[2002] with the forcing split correctly, the results for the NAO found by Peterson et al. still qualitatively hold, namely that a significant part of the interannual variability of the NAO is accounted for by the extratropical forcing, while the recent upward trend in the NAO is related to the tropical forcing. For the case of the AO, a very different conclusion is obtained. In the previous results (Lin et al. [2002]), the extratropical forcing case showed no significant correlation between the model AO index and the

observed AO index, while the tropical forcing accounts for almost as much variance as the global forcing case. The relatively different driving source for the AO and NAO in the previous model results gave rise to a simple way to distinguish the hemispheric AO from the more regionally focused NAO. However, with the tropical/extratropical split corrected, we now found that, like the NAO, the interannual variability of the AO is also predominantly driven from the extratropics, and only half of the trend in the AO is tropically related. Thus, on the basis of the new results, no clear distinction is found between the NAO and AO in terms of the relative importance of the tropical and/or extratropical forcing in accounting for the variance in their respective indices.